Engineering Design and Analysis of Sustainable Mine Fills

Lead Guest Editor: Erol Yilmaz
Guest Editors: Gaili Xue, Haiqiang Jiang, and Shuai Cao
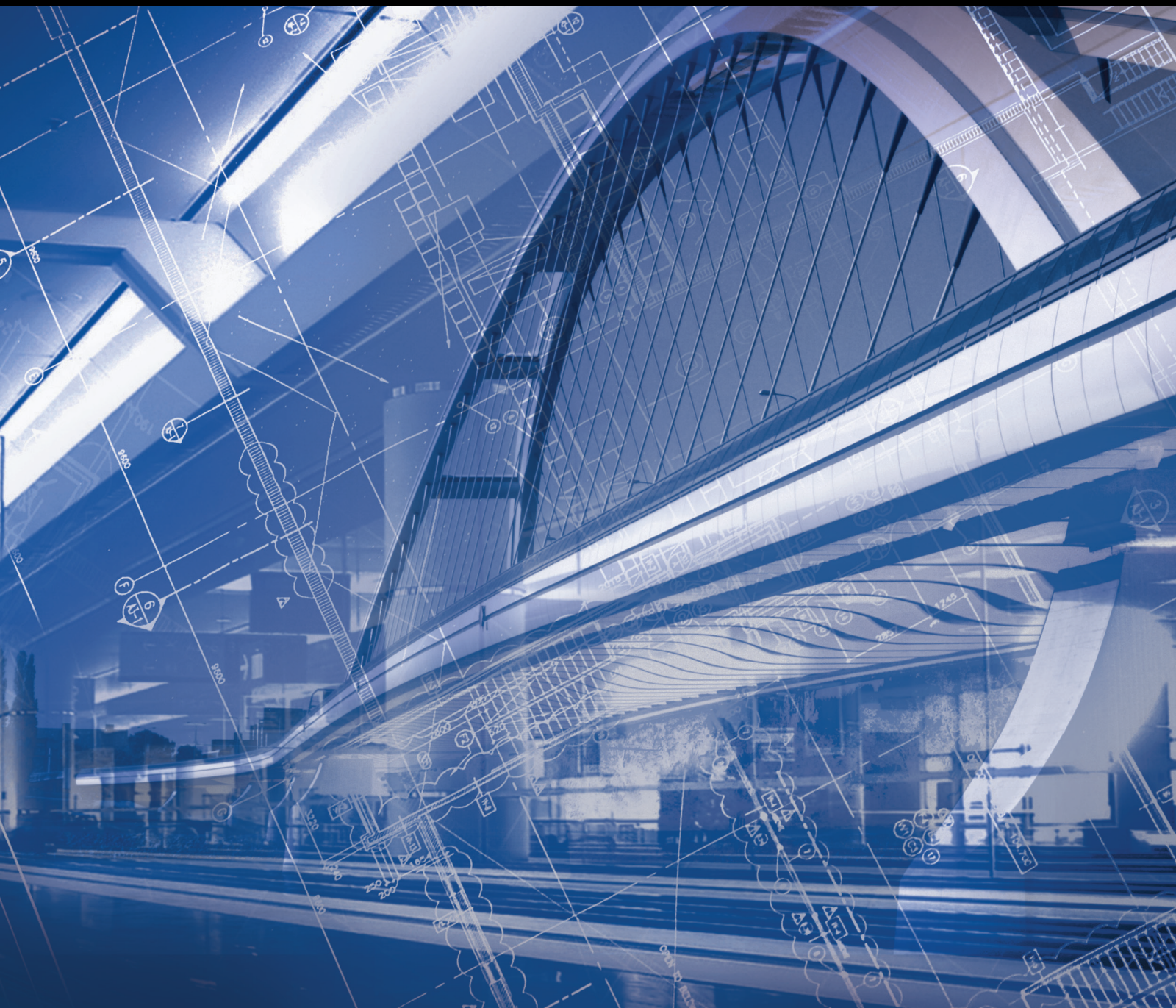
Engineering Design and Analysis of Sustainable Mine Fills

Engineering Design and Analysis of Sustainable Mine Fills

Lead Guest Editor: Erol Yilmaz
Guest Editors: Gaili Xue, Haiqiang Jiang, and Shuai Cao

Chayut Ngamkhanong (iD), Thailand
Trung Ngo, Australia
Tengfei Nian, China
Mehdi Nikoo (iD), Canada
Youjun Ning (iD), China
Olugbenga Timo Oladinrin (iD), United Kingdom
Oladimeji Benedict Olalusi, South Africa
Timothy O. Olawumi (iD), Hong Kong
Alejandro Orfila (iD), Spain
Maurizio Orlando (iD), Italy
Siti Aminah Osman, Malaysia
Walid Oueslati (iD), Tunisia
SUVASH PAUL (iD), Bangladesh
John-Paris Pantouvakis (iD), Greece
Fabrizio Paolacci (iD), Italy
Giuseppina Pappalardo (iD), Italy
Fulvio Parisi (iD), Italy
Dimitrios G. Pavlou (iD), Norway
Daniele Pellegrini (iD), Italy
Gatheeshgar Perampalam (iD), United Kingdom
Daniele Perrone (iD), Italy
Giuseppe Piccardo (iD), Italy
Vagelis Plevris (iD), Qatar
Andrea Pranno (iD), Italy
Adolfo Preciado (iD), Mexico
Chongchong Qi (iD), China
Yu Qian, USA
Ying Qin (iD), China
Giuseppe Quaranta (iD), Italy
Krishanu ROY (iD), New Zealand
Vlastimir Radonjanin, Serbia
Carlo Rainieri (iD), Italy
Rahul V. Ralegaonkar, India
Raizal Saifulnaz Muhammad Rashid, Malaysia
Alessandro Rasulo (iD), Italy
Chonghong Ren (iD), China
Qing-Xin Ren, China
Dimitris Rizos (iD), USA
Geoffrey W. Rodgers (iD), New Zealand
Pier Paolo Rossi, Italy
Nicola Ruggieri (iD), Italy
JUNLONG SHANG, Singapore

Nikhil Saboo, India
Anna Saetta, Italy
Juan Sagaseta (iD), United Kingdom
Timo Saksala, Finland
Mostafa Salari, Canada
Ginevra Salerno (iD), Italy
Evangelos J. Sapountzakis (iD), Greece
Vassilis Sarhosis (iD), United Kingdom
Navaratnarajah Sathiparan (iD), Sri Lanka
Fabrizio Scozzese (iD), Italy
Halil Sezen (iD), USA
Payam Shafigh (iD), Malaysia
M. Shahria Alam, Canada
Yi Shan, China
Hussein Sharaf, Iraq
Mostafa Sharifzadeh, Australia
Sanjay Kumar Shukla, Australia
Amir Si Larbi (iD), France
Okan Sirin (iD), Qatar
Piotr Smarzewski (iD), Poland
Francesca Sollecito (iD), Italy
Rui Song (iD), China
Tian-Yi Song, Australia
Flavio Stochino (iD), Italy
Mayank Sukhija (iD), USA
Piti Sukontasukkul (iD), Thailand
Jianping Sun, Singapore
Xiao Sun (iD), China
T. Tafsirojjaman (iD), Australia
Fujiao Tang (iD), China
Patrick W.C. Tang (iD), Australia
Zhi Cheng Tang (iD), China
Weerachart Tangchirapat (iD), Thailand
Xiaxin Tao, China
Piergiorgio Tataranni (iD), Italy
Elisabete Teixeira (iD), Portugal
Jorge Iván Tobón (iD), Colombia
Jing-Zhong Tong, China
Francesco Trentadue (iD), Italy
Antonello Troncone, Italy
Majbah Uddin (iD), USA
Tariq Umar (iD), United Kingdom
Muahmmad Usman, United Kingdom
Muhammad Usman (iD), Pakistan
Mucteba Uysal (iD), Turkey

Ilaria Venanzi (iD), Italy
Castorina S. Vieira (iD), Portugal
Valeria Vignali (iD), Italy
Claudia Vitone (iD), Italy
Liwei WEN (iD), China
Chunfeng Wan (iD), China
Hua-Ping Wan, China
Roman Wan-Wendner (iD), Austria
Chaohui Wang (iD), China
Hao Wang (iD), USA
Shiming Wang (iD), China
Wayne Yu Wang (iD), United Kingdom
Wen-Da Wang, China
Xing Wang (iD), China
Xiuling Wang (iD), China
Zhenjun Wang (iD), China
Xin-Jiang Wei (iD), China
Tao Wen (iD), China
Weiping Wen (iD), China
Lei Weng (iD), China
Chao Wu (iD), United Kingdom
Jiangyu Wu, China
Wangjie Wu (iD), China
Wenbing Wu (iD), China
Zhixing Xiao, China
Gang Xu, China
Jian Xu (iD), China
Panpan (iD), China
Rongchao Xu (iD), China
HE YONGLIANG, China
Michael Yam, Hong Kong
Hailu Yang (iD), China
Xu-Xu Yang (iD), China
Hui Yao (iD), China
Xinyu Ye (iD), China
Zhoujing Ye , China
Gürol Yildirim (iD), Turkey
Dawei Yin (iD), China
Doo-Yeol Yoo (iD), Republic of Korea
Zhanping You (iD), USA
Afshar A. Yousefi (iD), Iran
Xinbao Yu (iD), USA
Dongdong Yuan (iD), China
Geun Y. Yun (iD), Republic of Korea

Hyun-Do Yun (iD), Republic of Korea
Cemal YİĞİT (iD), Turkey
Paolo Zampieri, Italy
Giulio Zani (iD), Italy
Mariano Angelo Zanini (iD), Italy
Zhixiong Zeng (iD), Hong Kong
Mustafa Zeybek, Turkey
Henglong Zhang (iD), China
Jiupeng Zhang, China
Tingting Zhang (iD), China
Zengping Zhang, China
Zetian Zhang (iD), China
Zhigang Zhang (iD), China
Zhipeng Zhao (iD), Japan
Jun Zhao (iD), China
Annan Zhou (iD), Australia
Jia-wen Zhou (iD), China
Hai-Tao Zhu (iD), China
Peng Zhu (iD), China
QuanJie Zhu (iD), China
Wenjun Zhu (iD), China
Marco Zucca, Italy
Haoran Zuo, Australia
Junqing Zuo (iD), China
Robert Černý (iD), Czech Republic
Süleyman İpek (iD), Turkey

Contents

Research Article

Study on the Relation between Tailing Particle Size and Tailing Slurry Underflow Concentration

Yi Zou [ID],[1] **Qi Liu** [ID],[2,3] **and Weijun Liu** [ID][2]

[1]*Zijin Mining Group Co. Ltd., Xiamen 364200, China*
[2]*Changsha Mining Research Institute Co., Ltd., Changsha 410012, China*
[3]*DAYE NONFERROUS METALS GROUP HOLDINGS Co., Ltd., Huangshi 435111, China*

Correspondence should be addressed to Qi Liu; 345926583@qq.com

In order to study the effect of the physical properties of tailings on the concentration of tailing slurry underflow, the median particle size, control particle size, and density of the tailings of 9 typical mines were measured. Besides, static settlement test and dynamic thickening test of the tailing slurry of these 9 mines were separately conducted. The test results show that the underflow concentration of the tailing slurry is unrelated to the tailing density but is related to the tailing particle size. The finer the tailing particle size, the lower the underflow concentration. Through the nondimensional regression analysis, 3 relation equations were obtained: number 1 relation equation between the median particle size of tailings and the underflow concentration in the static settlement test, number 2 relation equation between the control particle size of tailings and the change in concentration in the static settlement test, number 3 relation equation between the underflow concentration in the static settlement test and the underflow concentration in the dynamic thickening test under different overflow water solid content conditions. Comparing the calculation results with the test results, it is found that the relative error between the predicted value and the test value does not exceed 6.1%, which has proved that the relation equations derived are convenient and feasible. The underflow concentration of the deep cone thickener can be predicted by merely measuring the particle size of the tailings, which means that the relation equations are highly recommended for wider use and application.

1. Introduction

With the progress and development of filling technology, more and more mines (especially metal mines) adopt or switch to the filling mining method [1–3]. The key technology of the filling mining method is the preparation of filling slurry (mainly composed of filling aggregate, cementitious material, and water) [4–6]. Due to a wide range of sources and low cost, tailings are often used as the main filling aggregate [7, 8]. Tailings are derived from the tailing slurry discharged after the mineral processing, and its concentration is normally only 10%~25%, which means it cannot be directly used to prepare high-concentration filling slurry. However, as for full tailing filling, especially cemented filling, it is required that the concentration of filling slurry should reach normally 65% to

75% and even higher for paste filling [9, 10]. Therefore, the tailing slurry must be concentrated and dehydrated before being used as a filling aggregate. The high-rate thickening of the tailing slurry is the key part of the full tailing filling technology [11, 12]. The underflow concentration is a key technical parameter for the thickening performance of tailings [13, 14]. It is found that the final underflow concentration greatly varies in the flocculation settlement tests of tailings from different mines.

At present, there are a lot of research studies on the sedimentation law and dense performance (underflow concentration, settlement speed, etc.) of the tailing slurry in both static settlement test and dynamic thickening test. In terms of static settlement test, Zhu [15] studied the relation between tailing particle size and underflow concentration and found that the higher the content of

fine particles in the tailings, the lower the underflow concentration; Grangeia et al. and [16] Arjmand [17] et al. have found that rapid tailing sedimentation can be achieved by selecting appropriate flocculant with proper dosage and the optimal tailing slurry concentration. Chen [18] used the Altman method to study the relation between settling time and the sedimentation height of the tailing slurry under different particle size conditions; Dong [19] sampled tailings from an iron mine, then studied the relation between the unit consumption of flocculant and the settling speed of this mine's tailing slurry under different tailing slurry concentrations, and then studied the relation between the unit consumption of flocculant and the ultimate underflow concentration under different tailing slurry concentrations; Wang et al. [20] found that the tailing slurry can be magnetized to improve the sedimentation performance; Liyi et al. [21] found that sound waves can improve the sedimentation performance of tailings. In terms of dynamic thickening, Gao et al. [22] found that the underflow concentration will increase with the increase in the mud layer height in the thickener, but when the mud layer height increases to a certain height, the underflow concentration will no longer increase; Gao et al. [23] found that the underflow concentration is inversely proportional to solid flux, that is, the greater the tailing slurry processing capacity per unit area of the thickener, the lower the corresponding underflow concentration; Li et al. [24] found that the continuous disturbance of the tailing slurry by the thickener rake arm can significantly increase the settlement speed and the underflow concentration. That is, when using the same tailing slurry, the settlement speed of the dynamic thickening test is 20% faster than that of the static settlement test, and the underflow concentration is 8%~15% higher; Gongcheng [25] studied the influence of the size change in the tailing flocculation on the denseness performance of the tailing slurry with different speed of the thickener rake arm.

The focus of the above studies is to use a certain agent and/or technical methods to improve the settlement performance parameters of tailing slurry but did not go to an in-depth study of what causes the differences in thickening performance between different tailings. So far, there is no report on the quantitative relation between the underflow concentration of tailing slurry and the particle size of tailings. Therefore, the settlement test of the tailing slurry of 9 metal mines was carried out to study the relation among the composition of the tailing particle size, the optimal diluted concentration, and underflow concentration in both static settlement test and dynamic thickening test. Taking into account the length of the study, only the static settlement test and dynamic thickening test processes and results of Mine 2 are listed in this study. For the rest of the mines, only the test results are listed and the test process is not written. Considering that the sedimentation law and complicated denseness of the tailing slurry, especially the combined test of static and dynamic settlement, which has many influence factors, it is necessary to study the quantitative relationship equation between the underflow concentration of the slurry and the particle size of the tailings.

2. Process and Results of Static Settlement Test

2.1. Particle Size and Density of Tailings. A Malvern particle size analyzer was used to measure the tailing particle size (including control particle size and median particle size) of 9 mines, and a 25 mL pycnometer was used to measure the true density of the tailings of these 9 mines. The test results are shown in Table 1. It can be seen from Table 1 that the particle sizes of tailings from Mine 1 (bauxite mine in Guangxi province), Mine 2 (gold mine in Hunan province), and Mine 3 (iron mine in Shandong province) are relatively fine, the particle sizes of tailings from Mine 4 (iron mine in Hubei province), Mine 5 (polymetallic mine in Tibet), and Mine 6 (gold mine in Xinjiang province) are moderate, and the particle sizes of tailings from Mine 7 (copper mine in Yunnan province), Mine 8 (gold mine in Jiangxi province), and Mine 9 (lead and iron mines in Yunnan province) are relatively coarse.

2.2. Process of Static Settlement Test. Mine 2 is taken as an example. Under the same slurry concentration, three anionic flocculants are added, 83376, AG9020, and 665 V, at a ratio of 20 g/t, respectively. The 83376 flocculant is finally recommended to be used for Mine 2 tailings, after comparing the factors including sedimentation speed, clear liquid clarification degree, and underflow concentration.

2.2.1. Experiment on the Optimal Flocculant Addition Ratio. After determining the optimal flocculant, a control test was carried out in order to obtain the optimal tailing slurry concentration under different dosages of the flocculant. The tailing slurry was selected with different concentrations, and a control test was arranged: 83376 flocculant was separately added into four types of tailings (with tailings density of 20%, 16%, 13%, and 11%), in three times for each type. The first addition of flocculant was with the proportion of 15 g/t, 20 g/t the second, and 25 g/t the third, and the optimal test results under static settlement test were obtained. The static settlement test results of Mine 2 are shown in Figure 1.

It can be seen in Figure 1 that within a certain range (15 g/t~25 g/t), the speed of tailing settlement gradually increased as more flocculant was added into the tailing slurry, and it slowed down after the amount of flocculant reached 20 g/t. Therefore, the optimal addition ratio of 83376 type flocculant is 20 g/t.

2.2.2. Optimal Diluted Concentration. The optimal mass concentration of Mine 2 can be determined through the relation between solid flux and filling tailing slurry concentration. The relation curve is shown in Figure 2. It can be seen from Figure 2 that when the tailing slurry concentration is 14%, the solid flux is the largest, which means the optimal value of the tailing slurry mass concentration is about 14.0%.

The final tailing flocculant addition scheme of Mine 2 is as follows: flocculant model 83376, flocculant addition amount 20 g/t, and tailing slurry diluted concentration 14.0%.

TABLE 1: Summary of static flocculation settlement test results of various mines.

Sample no.	Density $\gamma/(g\cdot cm^{-3})$	Particle size (mm)		Optimal diluted concentration C_0 (%)	Underflow concentration C_1 (%)	Optimal flocculant type	Unit consumption of flocculant/$(g\cdot t^{-1})$	Remark
		Median particle size d_{50}	Control; particle size d_{60}					
Mine 1	2.010	0.0282	0.0391	17.5	53.1	AG9020	20.000	Bauxite
Mine 2	2.611	0.0335	0.0423	14.0	53.5	83376	20.000	Iron mine
Mine 3	2.322	0.0217	0.0302	10.1	42.7	83376	30.000	Gold mine
Mine 4	2.871	0.0492	0.0625	16.5	59.5	83376	10.000	Polymetallic mine
Mine 5	2.880	0.0443	0.0540	13.2	55.3	6013S	15.000	Iron mine
Mine 6	2.560	0.0548	0.0723	14.0	59.3	AG9020	10.000	Gold mine
Mine 7	2.689	0.1088	0.1407	16.7	68.0	76	10.000	Iron mine
Mine 8	2.451	0.1012	0.1288	14.0	64.7	AG6025	10.000	Lead iron mine
Mine 9	3.009	0.0847	0.1055	16.7	63.8	83376	7.500	Copper mine
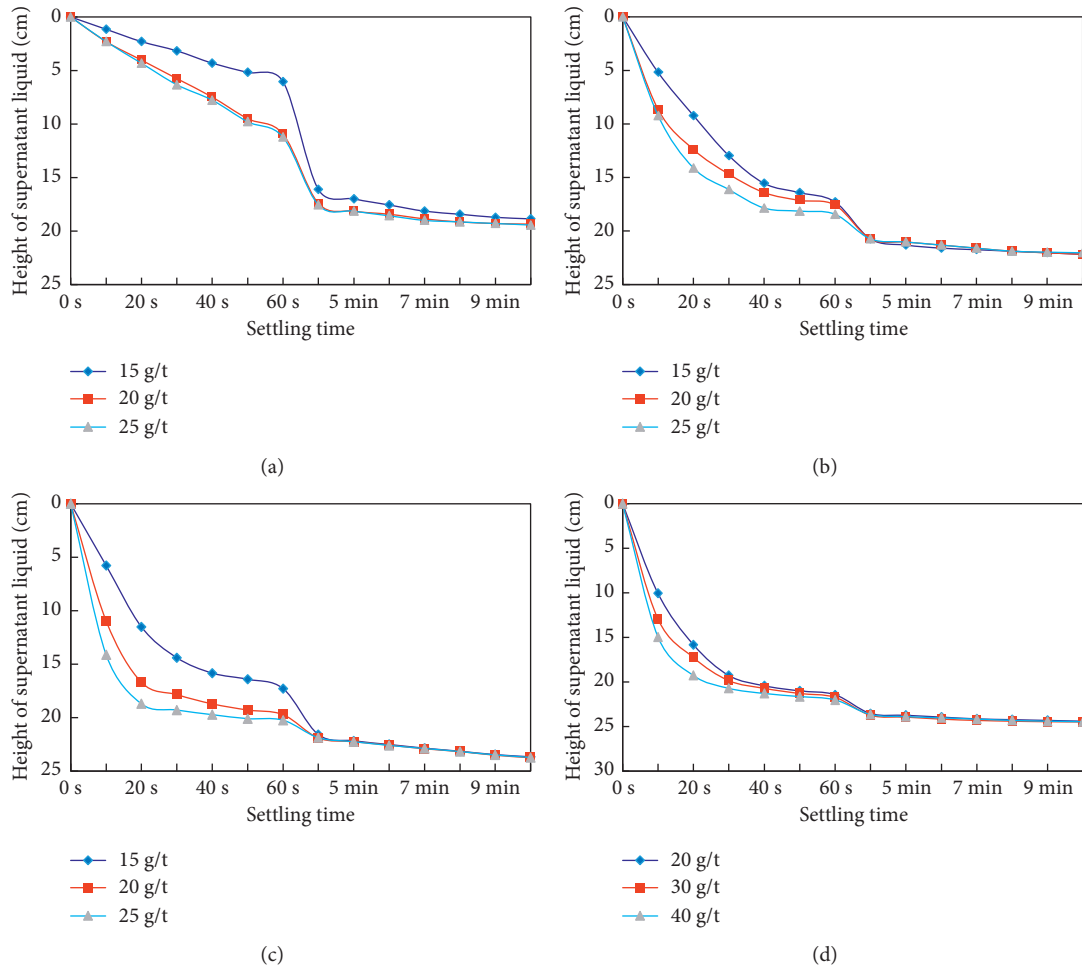
FIGURE 1: Settlement curves of different tailing slurry concentrations, (a) tailing slurry concentration at 20%, (b) tailing slurry concentration at 16%, (c) tailing slurry concentration at 13%, and (d) tailing slurry concentration at 11%.

2.3. Results of Static Settlement Test. The relation among the particle size and density of the tailings, the optimal flocculant type, the optimal flocculant addition, the optimal tailing slurry diluted concentration, and the tailing slurry throughput per unit area of 9 mines are shown in Table 1.
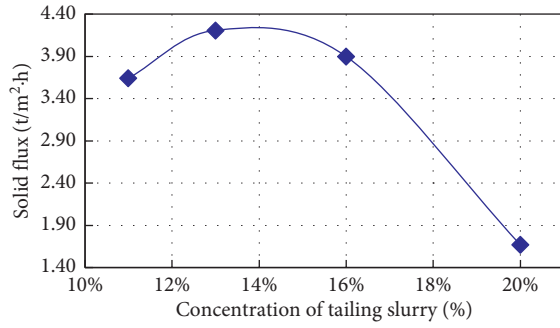
FIGURE 2: Settlement curves with different tailing slurry concentrations.

3. Relation between Tailing Particle Size and Underflow Concentration in Static Settlement Test

It can be seen in Table 1 that the coarser the tailing particle size is, the greater the underflow concentration becomes. In addition, there is a high degree of nonlinear correlation between both the median particle size of tailings and the control particle size of tailings with the underflow concentration. The function relation between both the median particle size and the control particle size of the tailings and the concentration of the tailing underflow is shown in equations (1) and (2). Considering the physical meaning of the fitting formula, when there are no tailings in the slurry, that is, when the particle size is close to 0, the underflow concentration C1 should also be 0. According to formula (1), when d50 is 0, the underflow concentration is −2.77. According to formula (2), when d60 is 0, the underflow concentration is −14.4%. It can be seen that the underflow concentration value calculated by the median particle size d50 is closer to the actual situation and more reliable.

$$C_1 = -20848d_{50}^{4} + 6387.5d_{50}^{3} - 701.6d_{50}^{2} + 34.009d_{50} - 0.0277. \tag{1}$$

$$C_1 = -8614.9d_{60}^{4} + 3445.7d_{60}^{3} - 495.94d_{60}^{2} + 31.373d_{60} - 0.144. \tag{2}$$

In the formula, C_0 is the initial slurry concentration, that is, the optimal slurry diluted concentration (%) in Table 1; C_1 is the underflow concentration. Figure 3

Through the settlement test, it is found that the greater the initial slurry concentration is, the higher the underflow concentration becomes. Therefore, it is necessary to consider the relation between the change in slurry concentration (the difference between the underflow concentration and the initial concentration) and the particle size of the tailings. The relation between the change in slurry concentration and the particle size of tailings is shown in Figure 4. It can be seen from the figure that there is not only a certain functional relation between the median particle size and the change in slurry concentration but also a certain functional relation between

the control particle size of the tailings and the change in slurry concentration, and both R-squared are close to 99%. From the perspective of the degree of fit, as long as the median particle size or control particle size of the tailings is known, the change in slurry concentration can be predicted. The functional relation is shown in equations (3) and (4).

$$C_1 - C_0 = -3993d_{50}^{4} + 1671.6d_{50}^{3} - 237.43d_{50}^{2} + 15.087d_{50} + 0.0917. \tag{3}$$

$$C_1 - C_0 = -4082.8d_{60}^{4} + 1708.2d_{60}^{3} - 259.52d_{60}^{2} + 17.909d_{60} - 0.0252. \tag{4}$$

Considering the physical meaning of the fitting formula, when there are no tailings in the slurry, that is, when the particle size is close to 0, the change in underflow concentration C_1–C_0 should also be 0. According to formula (3), when d_{50} is 0, the change in underflow concentration is 9.17%, and when d_{60} is 0, the change in underflow concentration is −2.52%, which shows that using the control particle size d_{60}, the calculated underflow concentration is more reliable.

4. Process and Results of Dynamic Thickening Test

4.1. Dynamic Thickening Test Equipment and Method. The dynamic thickening test uses 4 peristaltic pumps, which are used to pump dilution water, to pump flocculant, to pump tailing samples into the feeding system of the thickening test device, and to pump the underflow from the bottom of the test device. The dilution water is tap water; the flocculant is added through two different dosing points, and the addition amount is based on the data obtained from the static settlement test; the mass concentration of the tailing slurry is about 10% to 18%, and then, it is placed in a 100 L barrel with an electric mixer. All materials are fully mixed and finally pumped into the pipeline. The speed of the peristaltic pump is adjusted by calculation to make the flocculant and tailing sample reach the optimal addition ratio of the static settlement test and to simulate the results of the thickener under different conditions. When the height of the mud layer is 150 mm, then the measurement of the overflow water begins, and when the height of the mud layer is 240 mm, then the measurement of the underflow begins. The equipment required for the dynamic thickening test is shown in Figure 5.

4.2. Dynamic Thickening Test. According to the optimal flocculant type, flocculant unit consumption, and slurry diluted concentration obtained in the static settlement test, the effects of different feeding speeds (the rate of addition of tailing slurry) on overflow water clarity and underflow concentration in 9 mines were studied, respectively. The test results are shown in Table 2, while the underflow tailing samples are shown in Figure 6.

$$y = -20848x^4 + 6387.5x^3 - 701.6x^2 + 34.009x - 0.0277$$
$$R^2 = 0.9572$$

(a)

$$y = -8614.9x^4 + 3445.7x^3 - 495.94x^2 + 31.373x - 0.144$$
$$R^2 = 0.968$$

(b)
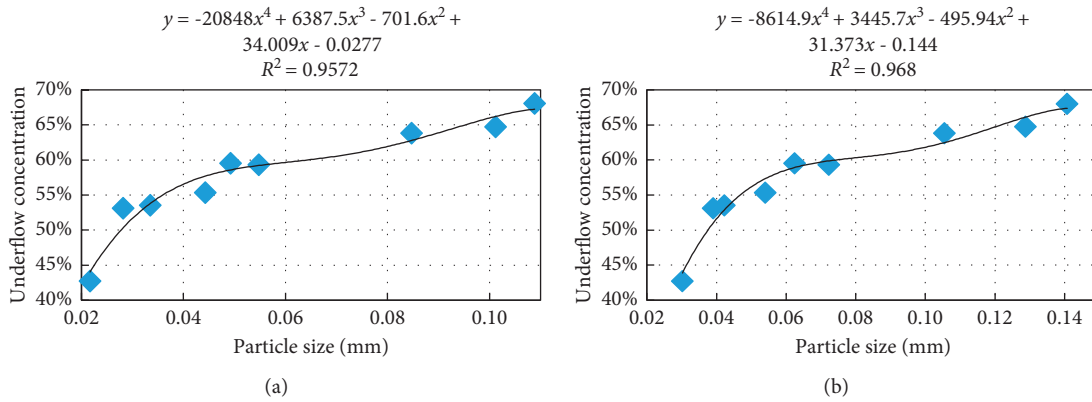
Figure 3: Nonlinear relation between particle size of tailings and underflow concentration. (a) Median particle size of tailings. (b) Control particle size of tailings.

$$y = -3993x^4 + 1671.6x^3 - 237.43x^2 + 15.087x + 0.0917$$
$$R^2 = 0.9912$$

(a)

$$y = -4082.8x^4 + 1708.2x^3 - 259.52x^2 + 17.909x - 0.0252$$
$$R^2 = 0.9859$$

(b)
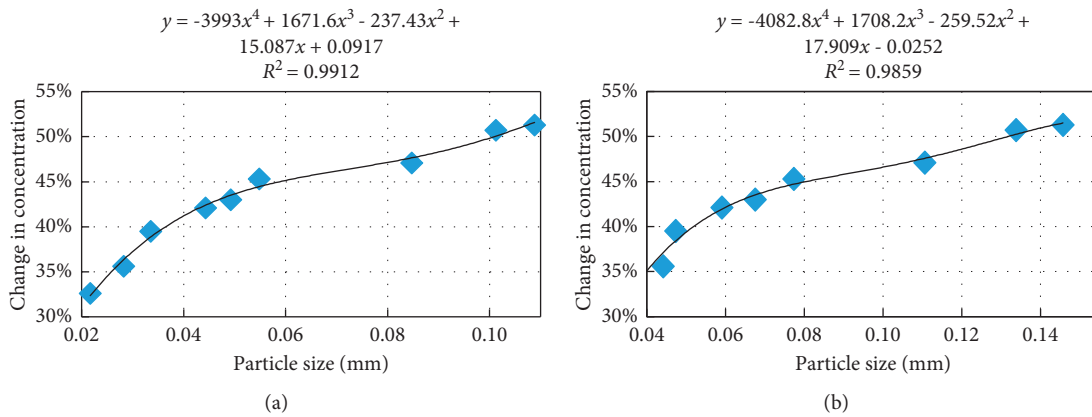
Figure 4: Nonlinear relation between particle size of tailings and change in concentration. (a) Median particle size of tailings. (b) Control particle size of tailings.

Figure 5: Dynamic thickening test equipment.

5. The Relation between Tailing Particle Size and Tailing Slurry Underflow Concentration

By analyzing the dynamic thickening test results, it is found that as the feeding speed decreases, the solid content of the overflow water gradually decreases, and the underflow concentration gradually increases. The main reason for this phenomenon is that the slower feeding speed prolonged the flocculation reaction time of tailing particles and the flocculation reaction is more thorough so that the solid content of the overflow water gradually decreases and the underflow concentration gradually increases. In the dynamic thickening test, the solid content of the overflow water at different feeding speeds is 50–400 ppm.

5.1. The Relation between Slurry Feeding Speed and Overflow Solid Content. The slurry feeding speed is an important index that affects the design of the tailing conveying system of the mineral processing plant and the thickening capacity of the deep cone thickener. The feeding speed is mainly determined through the thickening effect, especially the solid content of the overflow water. Using Mine 2 as an example, the relation between the feeding speed and the solid content of the overflow water in this mine is shown in Figure 7(a). In Figure 7(a), it is not only the fitting curve of the feeding speed and the solid content of the overflow water that are given but also the 3rd-degree polynomial function with its R-squared is given. The relation between the feeding speed and the solid content of the overflow water of these 9 mines is shown in Table 3.

Table 2: Results of dynamic thickening test.

Sample no.	Test no.	Slurry feeding speed v/(L/min)	Slurry concentration C_0 (%)	Slurry weight (kg) Before test	γ/(g·cm⁻³)	Tailing density	Tailings consumption (kg)	Time (min)	Underflow concentration	Overflow solid content f/ppm
Mine 1	1	0.12	17.5	60	56.19	2.01	0.666	30	67.95	48.35
	2	0.15	17.5	56.19	51.33	2.01	0.851	30	67.86	78.22
	3	0.17	17.5	51.33	45.67	2.01	0.992	30	67.8	96.21
	4	0.21	17.5	45.67	38.63	2.01	1.233	30	67.13	126.29
	5	0.25	17.5	38.63	30.53	2.01	1.416	30	66.86	156.21
	6	0.27	17.5	30.53	21.63	2.01	1.558	30	66.57	267.33
	7	0.30	17.5	21.63	11.86	2.01	1.709	30	66.38	352.69
Mine 2	1	0.32	14	144.7	134.05	2.611	1.491	30	67.86	58.22
	2	0.38	14	134.05	121.44	2.611	1.765	30	67.8	94.21
	3	0.46	14	121.44	106.31	2.611	2.119	30	67.13	126.29
	4	0.58	14	106.31	87.25	2.611	2.668	30	66.86	236.21
	5	0.73	14	87.25	63.42	2.611	3.336	30	64.38	372.69
Mine 3	1	0.82	10.1	130	103.86	2.322	2.64	30	52.25	321.73
	2	0.70	10.1	103.86	81.67	2.322	2.242	30	52.78	195.17
	3	0.55	10.1	81.67	64.2	2.322	1.765	30	53.27	115.23
	4	0.46	10.1	64.2	49.64	2.322	1.47	30	54.14	97.21
	5	0.33	10.1	49.64	39.08	2.322	1.067	30	54.53	90.45
Mine 4	1	0.42	16.5	100	85.82	2.871	2.34	30	72.95	73.58
	2	0.51	16.5	85.82	68.69	2.871	2.826	30	72.66	96.22
	3	0.61	16.5	68.69	48.35	2.871	3.357	30	72.23	196.21
	4	0.67	16.5	48.35	25.87	2.871	3.708	30	71.43	326.29
Mine 5	1	0.51	13.2	145	128.21	2.88	2.217	30	72.63	62.68
	2	0.60	13.2	128.21	108.64	2.88	2.583	30	71.94	101.3
	3	0.72	13.2	108.64	84.86	2.88	3.138	30	69.34	187.44
	4	0.76	13.2	84.86	59.96	2.88	3.287	30	67.75	215.87
	5	0.88	13.2	59.96	31.21	2.88	3.795	30	66.93	312.33
Mine 6	1	0.44	14	148	133.42	2.56	2.041	30	72.52	65.43
	2	0.56	14	133.42	115.2	2.56	2.551	30	72.24	123.47
	3	0.63	14	115.2	94.45	2.56	2.905	30	71.85	193.89
	4	0.68	14	94.45	72.3	2.56	3.101	30	71.33	247.22
	5	0.73	14	72.3	48.48	2.56	3.335	30	70.82	342.1
Mine 7	1	0.22	16.7	150	142.48	2.689	1.256	30	81.65	65.45
	2	0.28	16.7	142.48	133.14	2.689	1.56	30	81.14	78.22
	3	0.46	16.7	133.14	117.61	2.689	2.592	30	80.8	126.21
	4	0.59	16.7	117.61	97.97	2.689	3.281	30	79.4	156.29
	5	0.70	16.7	97.97	74.55	2.689	3.911	30	78.57	291.36
	6	0.81	16.7	74.55	47.5	2.689	4.517	30	77.46	461.53
Mine 8	1	0.44	14	158.1	143.86	2.451	1.994	30	78.12	72.13
	2	0.58	14	143.86	124.97	2.451	2.643	30	77.86	123.28
	3	0.67	14	124.97	102.98	2.451	3.079	30	77.35	190.47
	4	0.82	14	102.98	76.08	2.451	3.766	30	76.78	283.45
	5	0.97	14	76.08	44.26	2.451	4.455	30	76.36	367.81
Mine 9	1	0.78	16.7	130	103.6	3.009	4.409	30	73.37	324.17
	2	0.66	16.7	103.6	81.25	3.009	3.732	30	77.05	195.23
	3	0.56	16.7	81.25	62.46	3.009	3.138	30	78.62	107.21
	4	0.49	16.7	62.46	45.8	3.009	2.782	30	78.73	90.45
	5	0.45	16.7	45.8	30.58	3.009	2.542	30	78.78	87.62

5.2. The Relation between Slurry Feeding Speed and Underflow Concentration of Dynamic Thickening Test. The slurry feeding speed is closely related to the underflow concentration of the deep cone thickener. The relation between the feeding speed and the underflow concentration of Mine 2 is shown in Figure 7(b). In Figure 7(b), it is not only the fitting curve of the feeding speed and the underflow concentration that are given but also the 3rd-degree polynomial function with its R-squared is given. The relation between feeding speed and underflow concentration of these 9 mines is shown in Table 4.

FIGURE 6: Underflow of dynamic thickening test.

$y = -1615.8x^3 + 3382.2x^2 - 1403.9x + 213.91$
$R^2 = 0.9978$

$y = -102.93x^3 + 142.84x^2 - 68.754x + 78.783$
$R^2 = 0.9873$

(a)

(b)
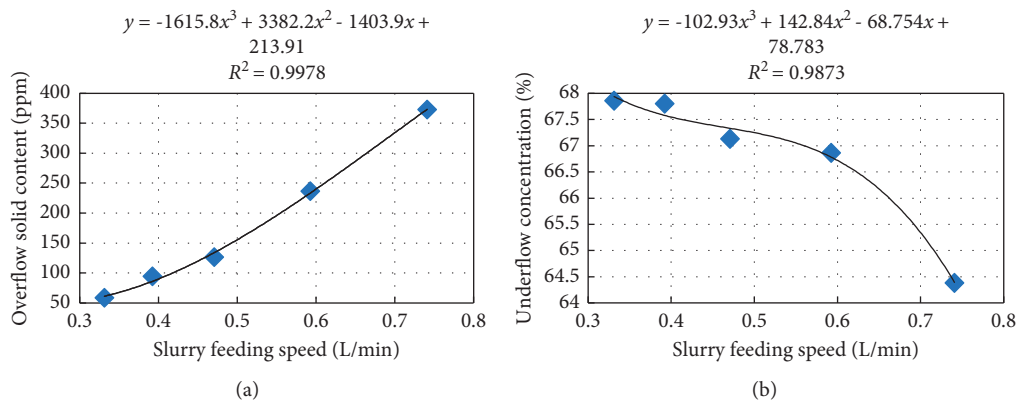
FIGURE 7: The relation between slurry feeding speed and (a) overflow solid content and (b) underflow concentration in mine 2.

TABLE 3: The correspondence table between overflow solid content and underflow concentration of dynamic thickening test.

Sample no.	Underflow concentration of static settlement test C_1 (%)	Overflow solid content 200 ppm		Overflow solid content 240 ppm		Overflow solid content 270 ppm		Overflow solid content 300 ppm	
		Feeding speed v/(L/min)	Underflow concentration C_2 (%)	Feeding speed v/(L/min)	Underflow concentration C_2 (%)	Feeding speed v/(L/min)	Underflow concentration C_2 (%)	Feeding speed v/(L/min)	Underflow concentration C_2 (%)
Mine 1	53.1	0.256	66.71	0.269	66.57	0.277	66.50	0.284	66.45
Mine 2	53.5	0.554	67.03	0.600	66.72	0.632	66.40	0.664	65.98
Mine 3	42.7	0.704	52.65	0.749	52.47	0.778	52.38	0.804	52.31
Mine 4	59.5	0.608	72.21	0.630	71.98	0.645	71.80	0.658	71.61
Mine 5	55.3	0.739	68.56	0.789	67.49	0.825	66.99	0.861	66.84
Mine 6	59.3	0.640	71.73	0.670	71.45	0.689	71.25	0.705	71.06
Mine 7	68	0.624	79.25	0.665	78.86	0.691	78.61	0.714	78.39
Mine 8	64.7	0.694	77.29	0.754	77.06	0.799	76.90	0.846	76.73
Mine 9	63.8	0.668	76.946	0.706	75.99	0.733	75.16	0.760	74.22

TABLE 4: The relation between slurry feeding speed and overflow solid content, and the relation between slurry feeding speed and underflow concentration.

Serial no.	Relation between slurry feeding speed v and overflow solid content f	Relation between slurry feeding speed v and underflow concentration C_2 of dynamic thickening test
Mine 1	$f = 95320v^3 - 48202\,v^2 + 8649.6v - 454.18$	$C_2 = 508.71v^3 - 333.4\,v^2 + 59.851\,v + 64.697$
Mine 2	$f = -1615.8v^3 + 3382.8\,v^2 - 1403.9\,v + 213.91$	$C_2 = -102.93v^3 + 142.84v^2 - 68.754\,v + 78.783$
Mine 3	$f = 1447.3v^3 - 1159.8\,v^2 + 280.3\,v + 72.424$	$C_2 = 16.366v^3 - 26.464v^2 + 8.5418\,v + 54.045$
Mine 4	$f = 8412.2v^3 - 8641.1v^2 + 2817.2\,v - 208.62$	$C_2 = -181.61v^3 + 272.61v^2 - 138.71\,v + 96.583$
Mine 5	$f = -1530.4v^3 + 3863.3v^2 - 2414.5\,v + 491.75$	$C_2 = 337.78v^3 - 703.06v^2 + 460.95\,v - 24.439$
Mine 6	$f = 8259.3v^3 - 11614v^2 + 5922.8\,v - 998.1$	$C_2 = -14.851v^3 + 3.464v^2 + 5.4232\,v + 70.726$
Mine 7	$f = 3376.5v^3 - 3694v^2 + 1516.2\,v - 127.88$	$C_2 = 8.9334v^3 - 22.005v^2 + 7.8756v + 80.731$
Mine 8	$f = -1478.3v^3 + 3283.9v^2 - 1763.8\,v + 336.7$	$C_2 = 3.5566v^3 - 6.7487v^2 + 0.3892v + 79.081$
Mine 9	$f = -4884.2v^3 + 11018v^2 - 7171\,v + 1529.9$	$C_2 = -49.505v^3 + 24.464v^2 + 11.36v + 73.191$

$$y = -0.0153x^2 + 2.7288x - 36.067$$
$$R^2 = 0.9961$$
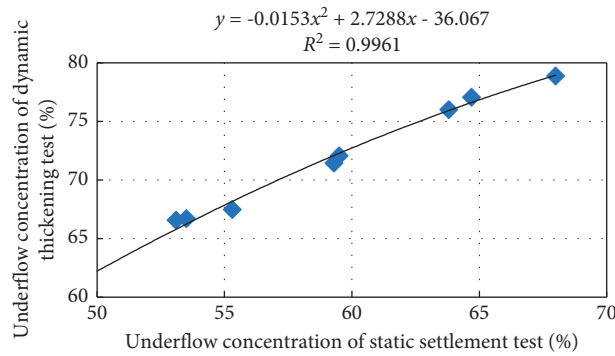
FIGURE 8: The relation between underflow concentration of static settlement test and underflow concentration of dynamic thickening test when overflow solid content is at 240 ppm.

TABLE 5: The relation between particle size and underflow concentration.

The relation between median particle size of tailings d50 and underflow concentration of static settlement test C_1		$C_1 = -20848 d_{50}^4 + 6387.5 d_{50}^3 - 701.6 d_{50}^2 + 34.009 d_{50} - 0.0277$
The relation between underflow concentration of static settlement test C_1 and underflow concentration of dynamic thickening test C_2	Overflow solid content At 200 ppm	$C_2 = -0.0162\ C_1^2 + 2.8395\ C_1 - 38.987$
	Overflow solid content At 240 ppm	$C_2 = -0.0153\ C_1^2 + 2.7288\ C_1 - 36.067$
	Overflow solid content At 270 ppm	$C_2 = -0.0162\ C_1^2 + 2.8395\ C_1 - 38.987$
	Overflow solid content At 300 ppm	$C_2 = -0.0145\ C_1^2 + C_1 - 32.778$

5.3. The Relation between Overflow Solid Content and Underflow Concentration of Dynamic Thickening Test.
When the solid content of the overflow is 200 ppm, 240 ppm, 270 ppm, and 300 ppm, the underflow concentrations of tailings in the 9 mines after treatment by the dynamic thickening device are shown in Table 4. It can be seen from Table 4 that the underflow concentration of the dynamic thickening test is 10%~15% higher than that of the static settlement test. It means that the underflow concentration of the tailing slurry treated through dynamic thickening test by deep cone thickener is higher than that treated through static settlement test by tailing silo. This shows that the deep cone thickener can more effectively increase the underflow concentration, enhance the strength of the underground filling body, and increase the reliability of high-concentration slurry transportation.

5.4. The Relation between Underflow Concentration of Static Settlement Test and Underflow Concentration of Dynamic Thickening Test.
When the solid content in the overflow water is 240 ppm, the relation between the underflow concentration of the static flocculation settlement test and the underflow concentration of the dynamic thickening test is shown in Figure 8. In Figure 8, it is not only the fitting curve of the underflow concentration C1 of the static settlement test and the underflow concentration C2 of the dynamic thickening test that are given but also the

2nd-degree polynomial function with its R-squared is given.

When the solid content of the overflow water is 200 ppm, 250 ppm, 270 ppm, and 300 ppm, the relation between the underflow concentration of static flocculation settlement test and the underflow concentration of dynamic thickening test, and the relation between the tailings particle size and the dynamic thickening test underflow concentration are shown in Table 5. It can be known from Table 4 that given certain particle size of the tailings and the underflow concentration of the static flocculation settlement test and the dynamic thickening test can be predicted.

6. Comparative Analysis of Calculation Results and Test Results

When the tailing density, median particle size, and control particle size are known, the underflow concentration of each mine from the static settlement test and the underflow concentration of each mine from the dynamic settlement test under different overflow solid content conditions can be calculated by the formula obtained in Table 5. When the solid content of the overflow is 240 ppm, the test results of the static and dynamic settlement tests of 9 mines are compared and analyzed with the calculation results. The details are given in Table 6. It can be found from Table 6 that the relative error percentage of the calculated value and the

TABLE 6: Comparison of calculation results and test results.

Sample no.	Ture density g/cm³	Median particle size d_{50}	Control particle size d_{60}	Underflow concentration of static settlement test			Underflow concentration of dynamic settlement test when the solid content of overflow is 240 ppm		
				Tested value (%)	Calculated value (%)	Relative error (%)	Tested value	Calculated value	Relative error (%)
Mine 1	2.010	0.0282	0.0391	53.1	50.35	5.18	66.57	62.54	6.06
Mine 2	2.611	0.0335	0.0423	53.5	53.81	0.58	66.72	66.47	0.37
Mine 3	2.322	0.0217	0.0302	42.7	44.06	3.18	52.47	54.46	3.79
Mine 4	2.871	0.0492	0.0625	59.5	58.58	1.55	71.98	71.28	0.97
Mine 5	2.880	0.0443	0.0540	55.3	57.70	4.35	67.49	70.45	4.39
Mine 6	2.560	0.0548	0.0723	59.3	59.22	0.13	71.45	71.88	0.60
Mine 7	2.689	0.1088	0.1407	68.0	67.26	1.10	78.86	78.25	0.77
Mine 8	2.451	0.1012	0.1288	64.7	66.22	2.34	77.06	77.54	0.62
Mine 9	3.009	0.0847	0.1055	63.8	62.79	1.59	75.99	74.95	1.37

tested value of the underflow in either static or dynamic settlement test does not exceed 6.1%, which shows that the curve equation obtained by regression analysis is reliable and can be used to guide actual production.

7. Conclusions

(1) Through the static settlement test, the optimal tailing slurry diluted concentration, underflow concentration, optimal flocculant type, and optimal amount of flocculant were determined for 9 typical mines. Different types of mines are with different optimal slurry diluted concentrations, generally about 10% to 18%; the underflow concentration of the static settlement test is generally about 50% to 65% (when the tailings are particularly fine in size, the underflow concentration is less than 43%. While the tailing particle size is particularly coarse, the underflow concentration can reach 68%). The underflow concentration of the dynamic thickening test is 10%~15% higher than that of the static flocculation settlement test. The coarser the particle size of tailings, the higher the underflow concentration. The optimal flocculant types and flocculant unit consumption vary when applied to different types of tailings. Type 83376 is the most widely used flocculant. The unit consumption of flocculant is generally about 7.5%~30%. In general, the finer the tailings, the larger the amount of flocculant.

(2) The study found that the underflow concentration and the change in tailing slurry concentration are closely related to the tailing particle size. Through the nondimensional theoretical regression analysis method, the mathematical equations between the factors are obtained: number 1 relation equation between the median particle size of tailings and underflow concentration of static flocculation settlement test, and number 2 relation equation between the controlled particle size of the tailings and the change amount on underflow concentration of the static settlement test.

(3) Through the dynamic thickening test, equations of these 9 mines are obtained: number 1 relation equation between the tailing slurry feeding speed and the solid content of the overflow, number 2 relation equation between the feeding speed and the underflow of the dynamic thickening test, number 3 relation equation between underflow concentration of static settlement test and underflow concentration of dynamic thickening test with different overflow solid content, and number 4 relation equation between the tailing particle size and the tailing slurry underflow concentration with different overflow solid content.

(4) Comparing the calculation results with the test results of these 9 mines, it is found that the relative error between the predicted value and the test value does not exceed 6.1%, which has proved that the relation equations derived are convenient and feasible. The underflow concentration of the deep cone thickener can be predicted by merely measuring the particle size of the tailings, which means that the relation equations are highly recommended for wider use and application.

Data Availability

The data used to support the findings of this study are available from the corresponding author upon request.

Conflicts of Interest

The authors declare that they have no conflicts of interest.

Acknowledgments

References

[1] Q. Chen, Q. Zhang, and C. Qi, "Recycling phosphogypsum and construction demolition waste for cemented paste backfill and its environmental impact," *Journal of Cleaner Production*, vol. 186, pp. 418–429, 2018.

[2] L. Yang, H. Wang, and A. Wu, "Status and development tendency of the full-tailings paste mixing technology," *Metal Mine*, vol. 7, pp. 34–41, 2016.

[3] X. M. Gong, Z. J Y, and L. W. Guo, "Theory and technology of backfilling in deep mines," in *Proceedings of the 2011 2nd International Conference on Mechanic Automation and Control Engineering*, Inner Mongolia, China, July 2011.

[4] Q. Chen, Y. Tao, Y. Feng, Q. Zhang, and Y. Liu, "Utilization of modified copper slag activated by Na2SO4 and CaO for unclassified lead/zinc mine tailings based cemented paste backfill," *Journal of Environmental Management*, vol. 290, p. 112608, 2021.

[5] Q. Zhang, Y. Li, Q. Chen, Y. K. Liu, Y. Feng, and D. L. Wang, "Effects of temperatures and pH values on rheological properties of cemented paste backfill," *Journal of Central South University*, vol. 28, no. 6, pp. 1707–1723, 2021.

[6] C. Qi, X. Tang, X. Dong, Q. Chen, A. Fourie, and E. Liu, "Towards Intelligent Mining for Backfill: a genetic programming-based method for strength forecasting of cemented paste backfill," *Minerals Engineering*, vol. 133, pp. 69–79, 2019.

[7] X. M. Wang, B. Zhao, and Q. L. Zhang, "Cemented backfilling technology with unclassified tailings based on vertical sand silo," *Journal of Central South University of Technology*, vol. 15, no. 6, pp. 801–807, 2008, (English Edition).

[8] X. Chen, X. Jin, H. Jiao, Y. Yang, and J. Liu, "Pore connectivity and dewatering mechanism of tailings bed in raking deep-cone thickener process," *Minerals*, vol. 10, no. 4, p. 375, 2020.

[9] Q. Chen, Y. Tao, Q. Zhang, and C. Qi, "The rheological, mechanical and heavy metal leaching properties of cemented paste backfill under the influence of anionic polyacrylamide," *Chemosphere*, vol. 286, p. 131630, 2022.

[10] M. Sheshpari, "A review of underground mine backfilling methods with emphasis on cemented paste backfill," *Electronic Journal of Geotechnical Engineering*, vol. 20, no. 13, pp. 5183–5208, 2015.

[11] Q. Chen, S. Sun, Y. Liu, C. C. Qi, H. B. Zhou, and Q. L. Zhang, "Immobilization and leaching characteristics of fluoride from phosphogypsum-based cemented paste backfill," *International Journal of Minerals, Metallurgy and Materials*, vol. 28, no. 9, pp. 1440–1452, 2021.

[12] S. Wang, X. Song, X. J. Wang, Q. S. Chen, J. C. Qin, and Y. X. Ke, "Influence of coarse tailings on flocculation settlement," *International Journal of Minerals Metallurgy and Materials*, vol. 27, no. 8, pp. 1065–1074, 2020.

[13] X. Du, G. Feng, T. Qi, Y. Guo, Y. Zhang, and Z. Wang, "Failure characteristics of large unconfined cemented gangue backfill structure in partial backfill mining," *Construction and Building Materials*, vol. 194, pp. 257–265, 2019.

[14] C. Piao, D. Wang, H. Kang, H. He, C. Zhao, and W. Liu, "Model test study on overburden settlement law in coal seam backfill mining based on fiber Bragg grating technology," *Arabian Journal of Geosciences*, vol. 12, no. 13, pp. 1–9, 2019.

[15] J. Zhu, F. Liu, and Y. Xiong, "Experimental study on settlement characteristics of tailings with different particle size grading," *Mining Research and Development*, vol. 40, no. 5, pp. 41–44, 2020.

[16] C. Grangeia, P. Ávila, and M. Matias, "Mine tailings integrated investigations: the case of Rio tailings (Panasqueira Mine, Central Portugal)," *Engineering Geology*, vol. 123, no. 4, pp. 359–372, 2011.

[17] Arjmand R, Massinaei M, and A. Behnamfard, "Improving flocculation and dewatering performance of iron tailings thickeners," *Journal of Water Process Engineering*, vol. 31, pp. 1–8, 2019.

[18] J. Chen, Y. Chen, M. A. L. long et al., "Experimental analysis on tailings sedimentation regularity based on Altman method," *Industrial Minerals & Processing*, vol. 48, no. 7, pp. 30–32 43, 2019.

[19] P. Dong, *Research on Cementitious Materials and Rheological Properties of the Whole Tailings in Angang Iron*, University of Science and Technology, Beijing, 2017.

[20] X.-min Wang, J.-wen Zhao, and De-ming Zhang, "Optimal prediction model of flocculating sedimentation velocity of unclassified tailings," *Chinese Journal of Nonferrous Metals*, vol. 03, pp. 793–798, 2015.

[21] Z. H. U. Li-yi, L. ü Wen-sheng, Y. Peng, and Z. Wang, "Influence of acoustic wave on thickening sedimentation of unclassified tailings," *Chinese Journal of Nonferrous Metals*, vol. 523, no. 1, pp. 2850–2859, 2020.

[22] Z. Gao, A. Wu, and H. Jiao, "Dynamic thickening sedimentation of unclassified tailings," *Nonferrous Metals*, vol. 69, no. 2, pp. 1–6, 2017.

[23] W. Gao, H. Wang, and C. Hui, "Study on main factors of underflow concentration in the dynamics thickening process of tailings," *Metal Mine*, vol. 485, no. 11, pp. 102–105, 2016.

[24] Z. Li, L. Guo, and X. Wei, "Research on flocculation and settlement mechanism of tailings slurry disturbed," *Gold Science and Technology*, vol. 27, no. 2, pp. 265–270, 2019.

[25] L. I. Gongcheng, *Study on Size Change of Unclassified Tailings Floes and its Thickening Performance*, University of Science and Technology, Beijing, 2018.

Research Article

A Large Goaf Group Treatment by means of Mine Backfill Technology

Hanwen Jia [1,2] **Baoxu Yan** [3] **and Erol Yilmaz** [4]

[1]*Deep Mining Laboratory, Shandong Gold Group Co., Ltd., Yantai 264000, China*
[2]*Center for Rock Instability and Seismicity Research, School of Resource and Civil Engineering, Northeastern University, Shenyang 110819, China*
[3]*Energy School, Xi'an University of Science and Technology, Xi'an 710054, China*
[4]*Department of Civil Engineering, Geotechnical Division, Recep Tayyip Erdogan University, Fener, Rize TR53100, Turkey*

Correspondence should be addressed to Baoxu Yan; yanbaoxu@xust.edu.cn

There are few studies on the management methods of large-scale goaf groups per the specific surrounding rock mass conditions of each goaf. This paper evaluates comprehensively the stability of the multistage large-scale goaf group in a Pb-Zn mine in Inner Mongolia, China, via the modified Mathews stability diagram technique. The volume of each goaf to be backfilled was quantitatively analyzed in the combination of theoretical analysis and three-dimensional laser scanning technology. The corresponding mechanical characteristics of the filling were determined by laboratory testing while formulating the treatment scheme of the large goaf group using the backfill method. The applicability of the treatment scheme using the backfill was verified by the combination of the numerical results of the distribution of the surrounding rock failure zone and the monitored data of the surface subsidence. The research results and treatment scheme using the backfill can provide a reference for similar conditions of mines worldwide.

1. Introduction

The open stoping and shallow-hole blasting techniques have been most often employed in the initial steps of Chinese metal mining, bringing about the advance of the widely distributed goafs [1, 2]. The existence of large goaf groups is a grave menace to the mines' safety. It is easy to cause a variety of mine disasters, such as roof caving [3], surface subsidence [4], rib failure [5], and water inrushing [6], resulting in irretrievable casualties and property losses [7]. The essence of the safety management of a large goaf group is to transfer the stress concentration, ease the stress concentration on the rock mass or make the stress state reach a new relative balance, and ensure the mines' pressure and their secure productions [8, 9].

There are several safety treatment methods for the mined-out area left by underground mining, and they are as follows: caving mined-out area, backfill mined-out area, and permanent pillar support mined-out area [10, 11]. However,

studies showed that the goaf treatment of caving surrounding the rock requires higher construction technology. A large number of rocks in the empty area are prone to a sudden fall and can cause airwave damage. Permanent pillars to support the goaf can only meet the needs of short-term stability. The roof of the goaf has the risk of instability failure under the conditions of engineering blasting disturbance and rheological properties of the rock [12]. Many researchers have made corresponding achievements in the treatment of goaf using the backfill method: Bao et al. [13] determined the grouting parameters and scheme based on the laboratory test and field measurement and completed the backfill treatment of underground goaf. Li et al. [14] used theoretical analysis to discuss the deformation mechanism of longwall goaf, studied the physical and chemical properties of backfill materials, and finally determined the grouting scheme to complete the treatment of longwall goaf. Zhang et al. [15] proposed the method of solid backfill for room and pillar mining method, which changed the stress transfer

mechanism caused by secondary mining, in view of the great influence of secondary mining on the coal pillar in the process of mining by traditional caving method and chain instability failure of the coal pillar. Li et al. [16] studied whether backfill into the goaf has an influence on the rock strata movement and deformation of the surrounding rock mass, indicating that the cemented backfill has a great influence on the rock strata movement and can significantly slow down the surface subsidence and deformation, however, it cannot prevent surface subsidence. Kostecki and Spearing [17] showed that with the decrease of shear and unconfined compressive and tensile strength of the backfill, the coal pillar strength's increase was more owing to the limits of the mines instead of the material's mechanical properties.

However, thanks to the diverse conditions at each mine, each abandoned goaf provides information on different locations/morphological properties and treatment methods [18]. The stability of the mined-out area is a complex problem. It is not only related to the occurrence state of the mining body, such as buried depth, dip angle, and thickness but also related to the geological and mining conditions, such as mining times and mining methods [19–21].

The goaf stability analysis methods mainly include numerical simulation [22], in situ monitoring [23], and theoretical analysis [24]. For example, Qiao et al. [25] established the energy criterion of the underground space engineering stability using the catastrophe theory and evaluated the rock stability of a coal mine based on this criterion. Jiang et al. [26] predicted the deformation and failure depth of the surrounding rock of the underground chamber using the method of bionic particle swarm optimization combined with numerical calculation. Habibi et al. [27] assessed the durable stability of the diverse shapes and dimensions of the salt cavern subjected to cyclic loading based on numerical calculation. Yang et al. [28] evaluated the stability of underground cavities by combining the in situ stress monitoring data using the numerical simulation method.

Because of the idealization of theoretical formula construction and the limit of the sum of the field monitoring tools, the aforementioned method is inadequate for the stability evaluation of the large-scale multistage goaf group. It is worth noting that the Mathews stability graph method is a semiquantitative and semiempirical stope stability evaluation method [29]. The method is relatively simple and convenient for in situ implementation [30]. It can be used for stability evaluation before large-scale goaf management and is largely employed in underground hard-rock mining [31, 32].

In the process of backfilling and treating large mined-out areas, it was generally adopted to treat all mined-out areas equally and adopt the same type of backfill, such as cemented backfill, ignoring the sequence of backfill. The differential conditions of the surrounding rock mass in each goaf were ignored. For example, local rock collapse occurred in some goaf, and the collapsed rock masses filled the bottom of the goaf. The filling effect of these collapsed rocks needs to be paid attention to in the process of goaf

treatment. It is because the collapsed rock is often quite different from the cemented backfill in terms of mechanical properties. In addition, some of the mined-out area is relatively narrow and flat in spatial dimension, the surrounding rock deformation of this type of goaf is bigger after completing the backfill process, which will make the cemented backfill cause serious damage. Hence, at this time, it is not economic to use cemented backfill to treat the goaf. However, using uncemented backfill is often more effective and economic. That is to say, a precise backfill technique should be adopted when the large group goaf is treated.

This study evaluates comprehensively by the engineering background of a multistage large-scale goaf group in a Chinese Pb-Zn mine using the modified Mathews stability diagram technique. The volume of each goaf to be backfilled was evaluated in combination with theoretical analysis and 3D laser scanning technology (CMS). The corresponding mechanical characteristics of the backfill were determined by a laboratory test. The treatment scheme of the large goaf group using the backfill method was also formulated. The applicability of the treatment scheme using the mine backfill technology was verified in combination with the numerical results of the distribution of the surrounding rock failure zone and the monitored data of surface subsidence.

2. Engineering Background

Figure 1 shows the areas on the east of the line form the "eastern district," and the areas on the west form the "western district" in the tested Pb-Zn mine [33]. A geological model dealing the stope from a 768 m level to the 928 m level in the 3DMine software was established by field measurement and the existing engineering geological log. In the mining area, there are four surface subsidence areas and a total of six subsidence pits. The subsidence area of the F1 fracture zone of the lines 3 to 5, 5526 m^2 of the lines 9 to 13, 16,237 m^2 of the lines 25 to 29, and 2100 m^2 of the F3 fracture zone of the lines 53 to 57 is located in the delineated mobile zone as shown in Figure 1. The main reasons for the collapse are the goaf above the 808m level in the western area, the oxidation of some ore bodies near the surface, broken surrounding rock on the hanging wall, the fact that the mining method is mostly the sublevel open stoping method of mid-hole caving, and a strong broken zone that is produced nearby.

3. Stability Analysis of the Goaf Group

3.1. Control Principle of Mathews Stability Diagram.
Potvin [34] illustrates the stability diagram technique based on the calculation of HR (hydraulic radius) in the perilous surface and the improved stability no N′. These two factors were plotted on the graph and categorized as stable zone, transition zone, and caving zone (Figure 2) to express the stability of the underground excavation area [34, 35]. The hydraulic radius HR in the stability graph can be obtained using equation (1).
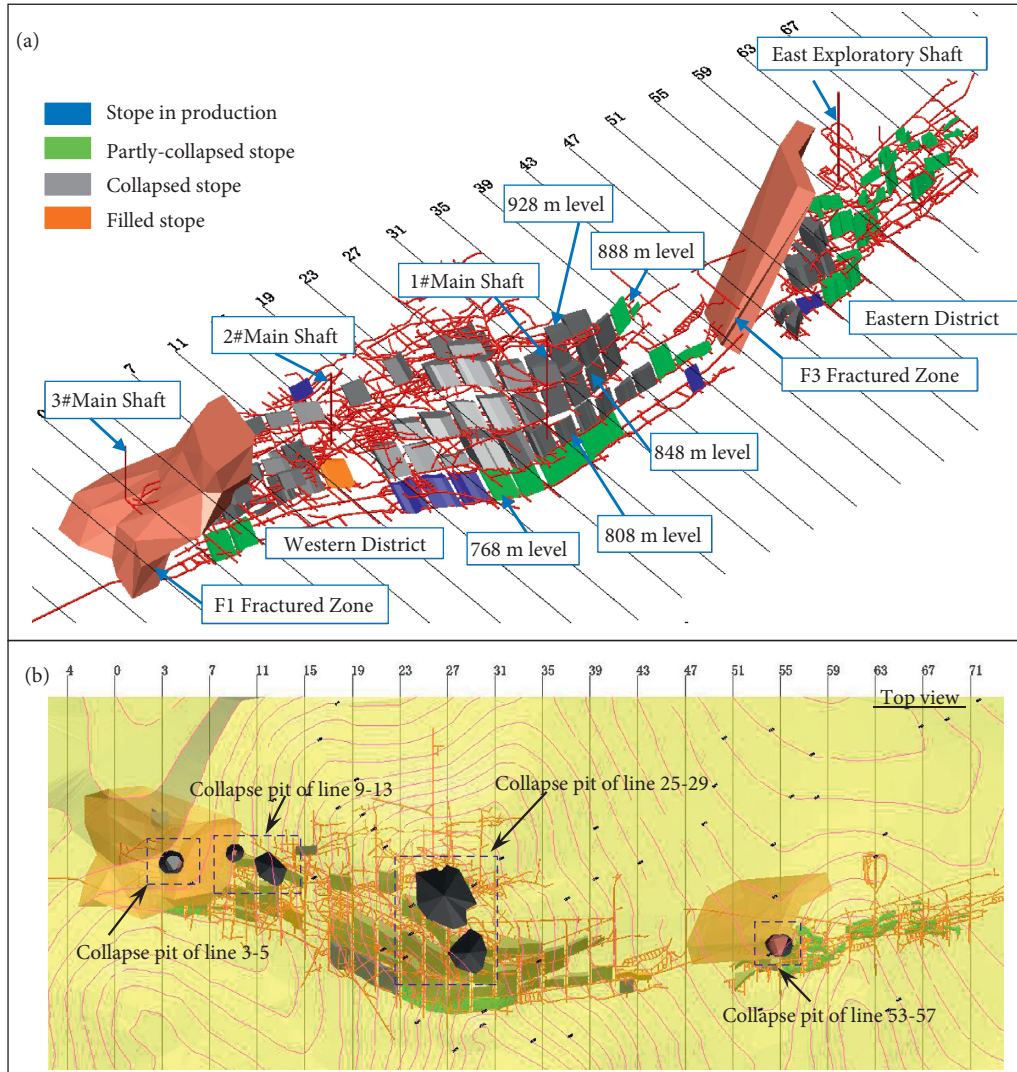
FIGURE 1: A layout of the tested Pb-Zn mine [33] (a) and the top view of the surface collapse pit (b).
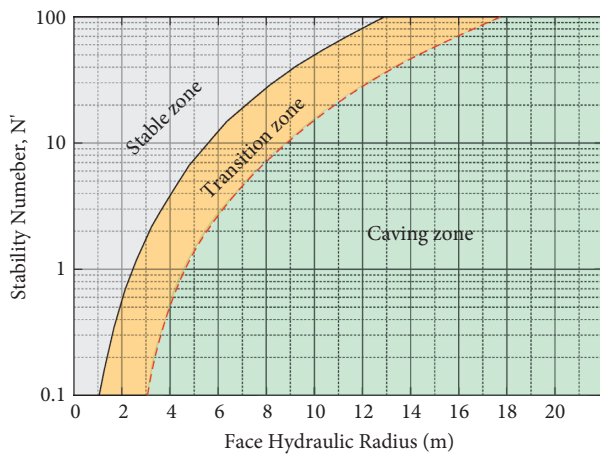
FIGURE 2: The Mathews stability graph [34].

$$HR = \frac{length \times width}{2 \times length + 2 \times width}. \tag{1}$$

The stability number N′ as shown in Figure 2 is calculated by equation (2).

$$N' = Q' \times A \times B \times C, \tag{2}$$

where Q' can be obtained by equation (3).

$$Q' = \frac{RQD}{J_n} \frac{J_r}{J_a}, \tag{3}$$

where RQD stands for rock quality index, J_n stands for joint number, J_r stands for joint roughness number, and J_a stands for joint change number.

Parameter B in equation (1) is the joint adjustment factor, and its value is measured by the difference between the dip angle of the mining face and the main joint set. Parameter C is the gravity adjustment factor. A is the rock stress factor. The compressive stress σ_{1max} is the extreme induced tangential stress acting on the center of critical face. Parameter A is linearly related to UCS/σ_{1max}, and its range is 0.1 to 1. It is calculated by equations (4) and (5). The detailed

procedure of these parameters can be found in the literature of Jia et al. [33].

$$R = \frac{\text{UCS}}{\sigma_{1\max}}, \tag{4}$$

$$A = \begin{cases} 0.1, & \text{If } R < 2, \\ \dfrac{0.9}{8}(R-2) + 0.1, & \text{If } 2 \leq R \leq 10, \\ 1, & \text{If } 10 < R. \end{cases} \tag{5}$$

For the rock materials, the tensile strength is much lower than the compressive strength, and hence, the instability caused by the tensile failure of rock mass must be estimated when calculating the modified stress coefficient, which is ignored by the current stability graph method [36]. Considering the influence of spatial multidimensional stress on the rock stress coefficient A, the authors modified the calculation method of the rock stress coefficient A by Hoek–Brown criterion, including tensile truncation [33]. The Mathews stability graph evaluation method suitable for thin orebody stope is obtained. This study will use this modified method to analyze the stability of the goaf group, providing a theoretical basis and reference for the subsequent goaf backfilling treatment planning.

3.2. Stability Calculation of Goaf Based on Mathews Stability Graph

3.2.1. Acquisition of Rock Parameters. In this paper, with the help of the ShapeMetrix3D digital measurement system, the rock mass discontinuities of 10 stopes in the eastern and western areas are investigated in a targeted way. As shown in Figure 3, the rock mass discontinuities are synthesized according to the obtained images based on similar pixel matching and line-of-sight judgment techniques. The mean value of the digital measurement results was taken to acquire the information of rock mass joints and the fissures and joints of each stope, and the results are listed in Table 1.

In this study, the rock mass geomechanical RMR value is converted into Barton's Q value using the basic rock mass quality index BQ value, the empirical conversion formula of the rock mass geomechanical RMR value [37], the Barton rock mass quality Q value given by Barton considering joint orientation, and the rock mass geomechanical RMR value [38]. Then, the Barton-modified Q'' value of the rock mass was solved. The joint density of Alhada rock mass $J_v = 7.23$ strip/m³ per 3GSM sweeps surface. Considering the surface conditions and joint density values, the geological strength index (GSI) of the rock mass is 60 per the rock mass structure. The main rock type of Alhada lead-zinc deposit is the argillaceous slate, and the material constant $m_i = 10$ can be obtained. As inferred from the above data, the rock mass strength variables of the orebody and the surrounding rock

can be obtained (Table 2), which provides a basis for numerical simulation and solving the rock stress coefficient A.

$$\text{RMR} = 15 \ln Q + 50,$$

$$\text{RMR} = \frac{(BQ - 80.79)}{6.09}. \tag{6}$$

3.2.2. The Determination of Stability Number N and Hydraulic Radius HR. The rock stress coefficient calculation method proposed by Jia et al. [33] requires a numerical simulation to obtain the highest and lowest principal stresses (σ_1 and σ_3, respectively) in the center of the stope's critical face. This study uses the FLAC³D and Rhino software to build numerical models. The model boundary dimensions are as follows: the length of 2400 m, the width of 600 m, and the average height of approximately 400 m. The top surface varies with the height of surface fluctuation: the highest height is 449 m, and the lowest height is 370 m. Figure 4 shows the numerical model. In the model's calculation, only the gravity stress field is considered, i.e., the equilibrium is solved only under the action of the self-weight of the rock. The boundary condition is that the top of the model is a free surface. The horizontal and vertical displacement limits are levied on the nearby boundary and the bottom, respectively.

The mechanical parameters of numerical calculation were selected according to Table 2. The Mohr–Coulomb constitutive model was adopted to excavate the mining rooms one by one in accordance with the actual mining sequence of the mine. The rock stress coefficients of each stope roof from the 808 m to 888 m stage were calculated per the contours of the mining-induced Max. principal stress and Min. principal stress shown in Figure 5.

For the value of B, the included angle between the exposed stope surface in the stereographic projection and the main joints in Table 1 are used for calculation, and parameter B is obtained according to the diagram of B in literature [34]. The value of C is mainly determined by $C = 8 - 6\cos\alpha$. Hydraulic radius HR is calculated according to geometric parameters of each stope. According to the roof stability number N and hydraulic radius HR of each goaf calculated above, the Mathews stability graph of each goaf's roof in the middle stage of 888 m, 848 m, and 808 m is finally obtained as shown in Figure 6. The stability evaluation results of each stope are shown in Tables 3, 4, 5. According to the field survey and calculation results, a three-dimensional model of the stope stability is drawn in Figure 7. At this point, the stope can be divided into a collapsed stope in the caving zone, a collapsed stope in the transition zone, a partly-collapsed stope in the stable zone, a partly-collapsed stope in the transition zone, a stope in production, and a filled stope. During the treatment of goaf, more attention will be paid to the first backfilling areas of the partly-collapsed stope in the stable zone and the partly-collapsed stope

(a)   (b)   (c)
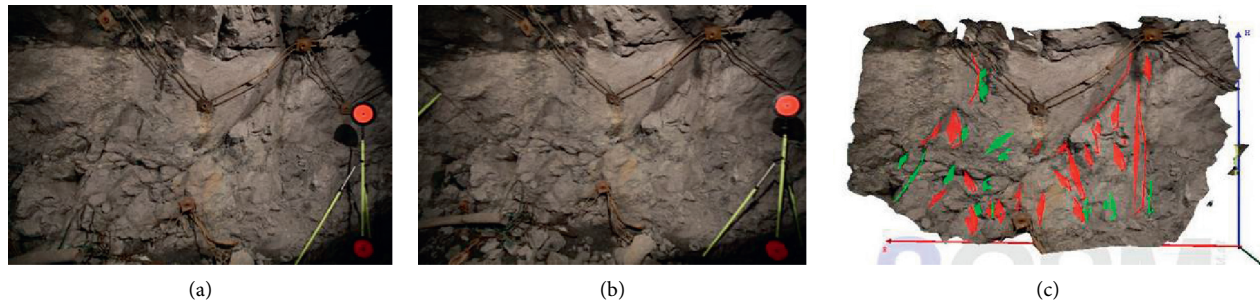
FIGURE 3: The scanning map of rock mass structural plane. (a) left view; (b) right view; (c) synthetic 3D map [33].

TABLE 1: The stope structural information.

Main joint tendency (°)	Main joint dip (°)
120	81
85	71
47	64
213	67
332	58
314	32
251	66
297	44
161	81
236	38

TABLE 2: Rock mass mechanical variables.

Variables	Slate	Ore
Uniaxial compressive strength (MPa)	9.38	7.65
Uniaxial tensile strength (MPa)	0.61	0.68
Apparent cohesion (MPa)	2.28	2.11
Angle of friction (°)	34.87	32.74
Young's modulus (GPa)	13.65	10.95
Specific gravity	2.58	3.67
Poisson's ratio	0.31	0.18

in the transition zone. The stability evaluation results provide a theoretical basis for the further formulation of a goaf backfilling planning.

3.3. Estimation of Goaf Volume Based on CMS Detection. The goaf is the structure left over after mining the orebody, and hence, it has the same structure and similar spatial morphology as the orebody. The mined-out areas left by the same vein keep a high degree of self-similarity in spatial morphology. Thus, the occurrence of other mined-out areas in the same vein can be qualitatively analyzed according to the detected mined-out area morphology, caving height, and stable state. In this paper, the cavity monitoring system (CMS) developed by Optech in Canada is used to conduct the spatial detection of the goaf of a typical stope.

Because of the open-pit operation in Alhada lead-zinc mine, most of the remaining mined-out areas have been damaged. Restricted by the site conditions, the stopes 7635 of the 35th line in the western area and 7661 of the 61st line in

the eastern area are selected as reference stopes to distinguish the occurrence state of the mined-out areas. The stope span of 7635 is 100 m with an inclination angle of 42°. The stope of 7661 has a 63 m span and 68° dip angle. The two stopes have the largest span and a slow dip angle on the west and east, respectively, and have the necessary conditions as a reference stope. Figure 8 indicates the caving conditions of the mined-out areas in stopes 7635 and 7661.

The stope span of 7635 is large, and the CMS laser scanner has a scanning blind area. Hence, the scanning results fail to cover all the stopes of 7635. It is observed from Figure 8(a) that the caving height is 14–17.5 m. Figure 8(b) shows that the caving height of stope 7661 is 8.2 m to 13.6 m. According to the field survey of the 888 m to 808 m stage in the west area, the stope is almost collapsed. Based on CMS laser detection, it can be seen that the final collapse form of 7635 stope in the western area is caused by the instability of the stope hang wall, and the stope roof is well-preserved. Therefore, it can be inferred that the 57th goaf collapsed from the stage of 888 m level to the stage of 808 m level in the western area is not caved in, and there may be triangular mined-out areas in the roof as shown in Figure 9.

The shape of the triangular mined-out area is determined by the static natural repose angle of rock, which is 40° in the lead-zinc mine. Therefore, it can be estimated that the residual mined-out area volume of 57 stopes collapsed in the west area accounts for about 5.8% of the stope volume. As the backfilling method is used for mining below the 808m level, the goaf in the 768m level in the western area is relatively well-preserved. It can be seen from the above section that the average height of the caved bulk in 7635 stope is approximately 15.7 m. From the ratio of the caved bulk height to the stope design height, it can be roughly concluded that the residual goaf volume in the west stope of 768 m level accounts for 50.9% of the stope volume.

According to the field survey on the 888 m level to 768 m level in the eastern district, except for the collapse of 7 stopes near the broken zone of lines 43 to 51, the mined-out areas of the other 28 stopes are relatively well-preserved. According to CMS laser detection results, the average caving height of the bulk in 7661 stope is approximately 10.9 m. From the ratio of the caving bulk height to the stope design height, it can be roughly concluded that the residual cavity volume in the eastern stope accounts for 65.9% of the stope volume. Similarly, there may still be triangular mined-out areas in the
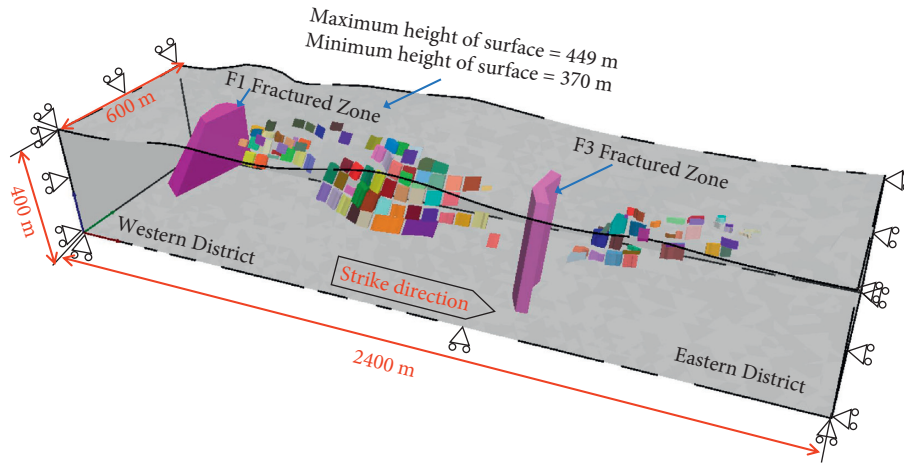
FIGURE 4: Numerical model.
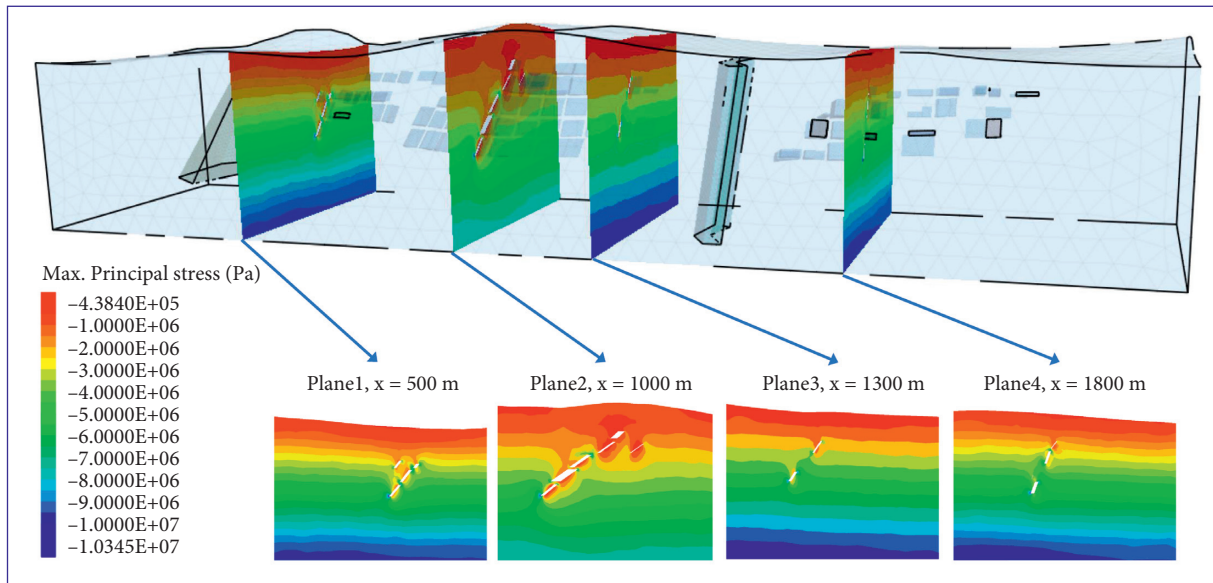
(a)
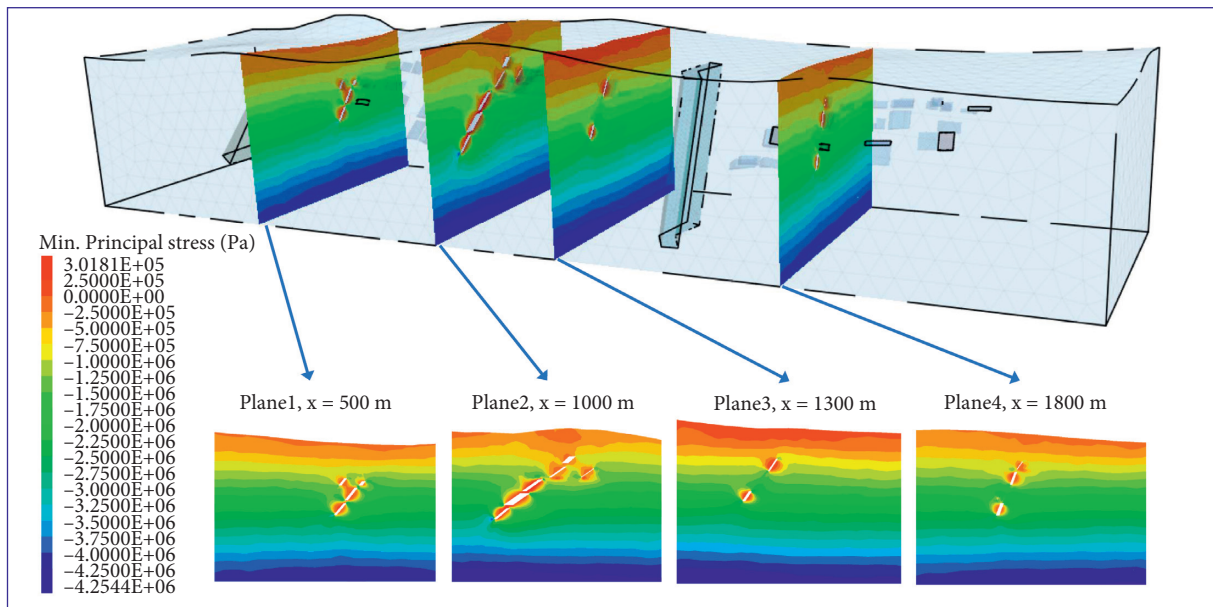
(b)

FIGURE 5: Contours of mining-induced (a) Max. principal stress and (b) Min. principal stress.
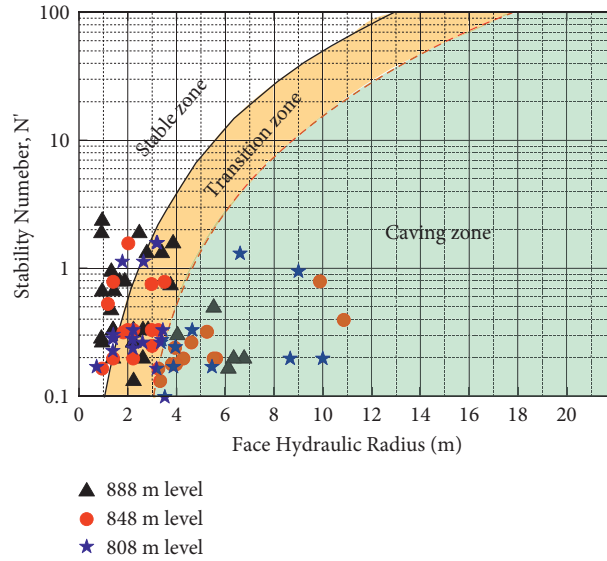
Figure 6: Mathews stability graph.

Table 3: Statistical results of goaf volume in 808 m level.

Stop number	Stope position	Stope span (m)	Stope height (m)	Stope thickness (m)	Exposed area of roof (m²)	Exposed perimeter of roof (m)	Goaf volume (m³)	Results of stability graph method
808–1#	1–3 line	20	15	10.5	210	61	260.8	Transition zone
808–2#	3–5 line	41	34	9.8	401.8	101.6	638.6	Transition zone
808–3#	5–7 line	42	34	9.5	399	103	646.2	Transition zone
808–4#	7–9 line	41	10	1.5	61.5	85	78.1	Stable zone
808–5#	9–11 line	41	34	8.5	348.5	99	569.5	Transition zone
808–6#	11–13 line	42	34	8	336	100	557.1	Transition zone
808–7#	13–15 line	42	34	7.5	315	99	557.6	Transition zone
808–8#	17–19 line	41	34	12	492	106	Backfilled	Caving zone
808–9#	19–21 line	40	30	5	200	90	327.5	Transition zone
808–10#	21–23 line	40	12	6	240	92	253.5	Transition zone
808–11#	23–25 line	40	34	40	1600	160	3813.3	Caving zone
808–12#	25–27 line	41	34	30	1230	142	2521.4	Caving zone
808–13#	27–29 line	40	30	15	600	110	709.8	Caving zone
808–14#	29–31 line	38	25	3	114	82	76.0	Transition zone
808–15#	31–33 line	39	27	3	117	84	215.8	Transition zone
808–16#	31–35 line	40	27	3	120	86	193.5	Transition zone
808–17#	35–37 line	40	22	3	120	86	319.7	Transition zone
808–18#	37–39 line	38	27	5	190	86	593.4	Transition zone
808–19#	39–41 line	35	34	5	175	80	365.9	Transition zone
808–20#	41–45 line	45	12	8	360	106	Backfilled	Transition zone
808–21#	53–55 line	45	30	30	1350	150	1827.3	Caving zone
808–22#	55–57 line	39	30	20	780	118	1066.0	Caving zone
808–23#	57–59 line	45.1	8	7.5	338.25	105.2	1523.0	Transition zone
808–24#	57–59 line	42	8	7.5	315	99	335.4	Transition zone
808–25#	61–63 line	46	8	3	138	98	1162.2	Transition zone
808–26#	61–63 line	46	8	3	138	98	1097.2	Transition zone
808–27#	65–67 line	45.5	34	6	273	103	3408.0	Transition zone
808–28#	67–69 line	32.4	34	4	129.6	72.8	2113.8	Stable zone
Total					25230.6			

TABLE 4: Statistical results of goaf volume in 848 m level.

Stop number	Stope position	Stope span (m)	Stope height (m)	Stope thickness (m)	Exposed area of roof (m^2)	Exposed perimeter of roof (m)	Goaf volume (m^3)	Results of stability graph method
848-1#	Of 3–5 line	35	15	15	525	100	549.7	Caving zone
848-2#	3–5 line	20	15	13	260	66	419.8	Caving zone
848-3#	Of 5–7 line	32	20	10	320	84	353.1	Caving zone
848-4#	5–7 line	30	12	12	360	84	351.9	Caving zone
848-5#	7–9 line	39	20	10	390	98	444.4	Caving zone
848-6#	9–11 line	42	20	7	294	98	287.2	Transition zone
848-7#	9–11 line	41	20	5	205	92	164.0	Transition zone
848-8#	9–11 line	20	20	5	100	50	108.3	Transition zone
848-9#	11–13 line	40	20	2	80	84	381.2	Stable zone
848-10#	11–13 line	40	20	8	320	96	95.1	Caving zone
848-11#	19–21 line	45	18	15	675	120	706.1	Caving zone
848-12#	21–23 line	42	22	15	630	114	1175.0	Caving zone
848-13#	23–25 line	40	30	5	200	90	405.3	Transition zone
848-14#	25–27 line	40	34	12	480	104	1103.6	Caving zone
848-15#	27–29 line	35	34	8	280	86	667.9	Transition zone
848-16#	29–31 line	35	34	8	280	86	616.5	Transition zone
848-17#	31–33 line	41	34	7	287	96	576.6	Transition zone
848-18#	31–35 line	41	34	4	164	90	393.4	Transition zone
848-19#	35–37 line	42	34	3	126	90	220.1	Transition zone
848-20#	53–55 line	30	4	58	1740	176	195.1	Caving zone
848-21#	55–57 line	42	30	45	1890	174	2408.9	Caving zone
848-22#	57–59 line	45.5	35	2.5	113.75	96	1255.2	Stable zone
848-23#	57–59 line	32	34	9	288	82	5993.7	Transition zone
848-24#	61–63 line	45.2	15	3	135.6	96.4	795.0	Stable zone
848-25#	63–65 line	40	34	4.5	180	89	4680.7	Stable zone
848-26#	67–69 line	40	20	7	280	94	5566.0	Transition zone
Total					29913.8			

7 collapsed stopes in the eastern area, and the volume of the residual mined-out areas accounts for 5.8% of the stope volume. According to this qualitative estimation, all goaf volumes from the 808 m to 888 m level can be obtained as shown in Tables 3 to 5. The results of cavity scanning based on CMS detection provide the data basis for the backfilling quantity required by the subsequent cavity management.

4. Goaf Treatment by Precise Backfill Technology

This study implemented the backfill process based on the principle of precision backfill in goaf. The goaf precision backfill technology is to study the precision backfill theory according to the surrounding rock mass conditions and mainly solve the five problems, namely "how much to fill, what to fill, when to fill, how to fill, and what effect." The specific technical ideas are as follows: firstly, the 3D laser scanning of the goaf is carried out according to CMS to realize the rapid reconstruction of the 3D contour of the goaf. Secondly, the joint and fissure structure characterization, the stability analysis of the goaf, and the numerical reconstruction of the three-dimensional shape are carried out. Again, the rock sample drilled from the site was tested, and the corresponding mechanical properties were obtained. The physical and chemical characteristics of the tailings were analyzed. The mechanical characteristics of the relationship between the hardened backfill and the nearby rock mass, the matching relationship between the creep deformation of the nearby rock mass, and the backfill were analyzed to realize the configuration of the backfill type and backfill scheme according to the deformation conditions of the nearby rock. Then, as said by the precise detection and numerical reconstruction of the goaf, the stability analysis results of the goaf, and the accurate matching relationship between the backfill and the nearby rock mass, the type and quantity of backfill needed for a specific goaf were calculated to realize the precise backfill of goaf. Finally, the applicability of the treatment scheme using backfill was verified in the combination of the results of the distribution of the nearby rock failure zone and the monitored data of surface subsidence.

4.1. Integrated Planning. As stated by field investigation, there are 101 mined-out areas, including 68 in the west and 33 in the east. Most of the goaf in the west area has a large volume, large exposed roof area, and poor stability. The existence of goaf has caused great hidden trouble to safety production. Combined with the production practice of Alhada lead-zinc mine and according to the distribution characteristics of goaf, the overall planning scheme of goaf

TABLE 5: Statistical results of goaf volume in 888 m level.

Stop number	Stope position	Stope span (m)	Stope height (m)	Stope thickness (m)	Exposed area of roof (m²)	Exposed perimeter of roof (m)	Goaf volume (m³)	Results of stability graph method
888–1#	9–11 line	41.5	18	6	249	95	247.1	Transition zone
888–2#	11–13 line	41.5	15	5	207.5	93	148.6	Transition zone
888–3#	17–19 line	41	25	3	123	88	192.2	Transition zone
888–4#	21–23 line	41	25	3	123	88	190.6	Caving zone
888–5#	23–25 line	42	25	20	840	124	1051.0	Caving zone
888–6#	25–27 line	41	30	5	205	92	232.1	Transition zone
888–7#	25–27 line	42	25	5	210	94	643.7	Transition zone
888–8#	27–27 line	42	30	15	630	114	1133.7	Caving zone
888–9#	27–29 line	41	25	3	123	88	77.1	Stable zone
888–10#	27–29 line	42	25	5	210	94	242.2	Transition zone
888–11#	29–31 line	42	20	10	420	104	655.6	Caving zone
888–12#	29–31 line	41	30	6	246	94	451.0	Transition zone
888–13#	31–33 line	43	8	18	774	122	319.3	Caving zone
888–14#	31–33 line	43	34	5	215	96	323.1	Transition zone
888–15#	33–35 line	44	34	17	748	122	1138.5	Caving zone
888–16#	35–37 line	44	34	6.5	286	101	572.9	Transition zone
888–17#	37–39 line	42	34	3	126	90	459.2	Stable zone
888–18#	39–41 line	41	10	2	82	86	37.8	Stable zone
888–19#	55–57 line	10	8	5	50	30	3177.9	Stable zone
888–20#	55–57 line	5	15	15	75	40	230.8	Stable zone
888–21#	57–59 line	10.3	12	4	41.2	28.6	1413.1	Stable zone
888–22#	59–61 line	30.2	8	10	302	80.4	2005.9	Transition zone
888–23#	61–63 line	27.2	15	7	190.4	68.4	2782.0	Transition zone
888–24#	63–65 line	38.9	14	2	77.8	81.8	2653.3	Stable zone
888–25#	63–65 line	45	14	8	360	106	863.9	Transition zone
888–26#	65–67 line	24	15	2	48	52	601.9	Stable zone
888–27#	65–67 line	22.8	15	3	68.4	51.6	534.3	Stable zone
888–28#	65–67 line	21.4	15	3	64.2	48.8	479.1	Stable zone
888–29#	67–69 line	21.9	14	2	43.8	47.8	621.4	Stable zone
888–30#	67–69 line	20.8	15	6.5	135.2	54.6	179.4	Stable zone
888–31#	69–71 line	33.8	6	10	338	87.6	824.2	Transition zone
888–32#	69–71 line	40	7.5	2	80	84	264.6	Stable zone
Total					24747.5			
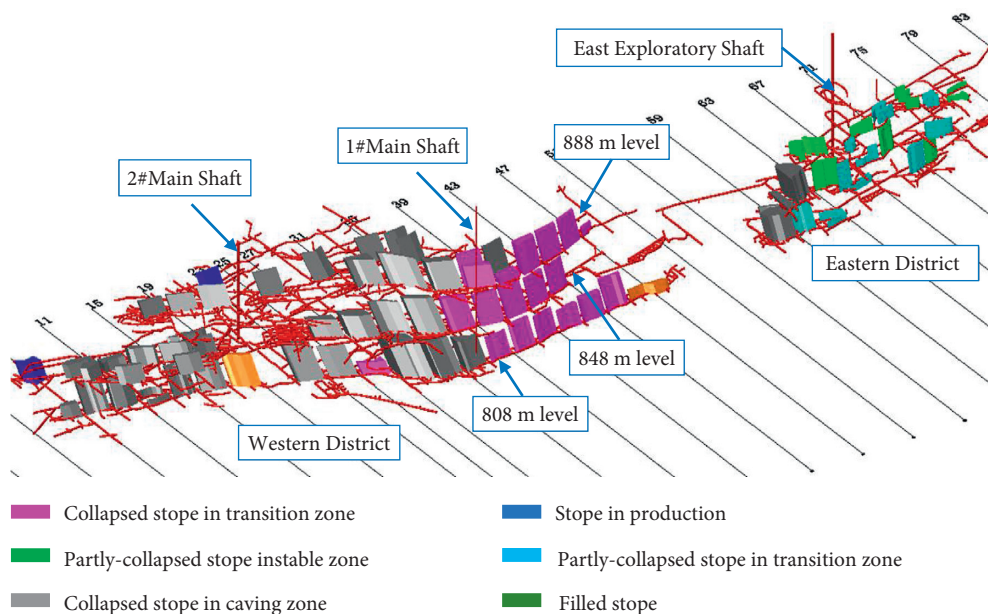
FIGURE 7: 3D graph of stope stability modified by the Mathews Stability Graph method.
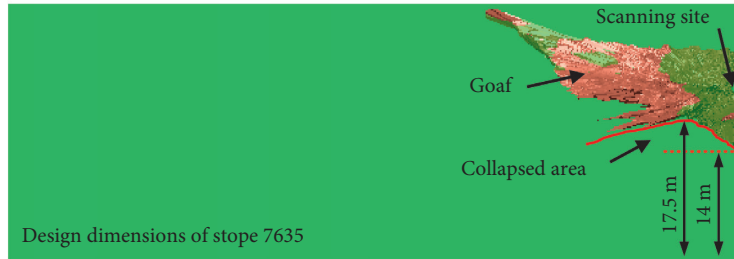
(a)
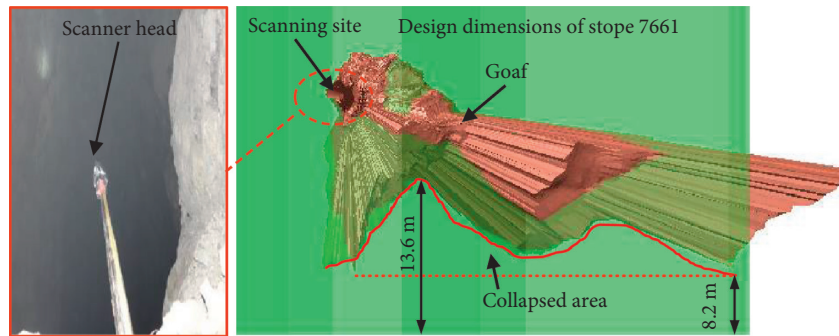
(b)

FIGURE 8: Scanning results of roof caving stopes 7635 (a) and 7661 (b).
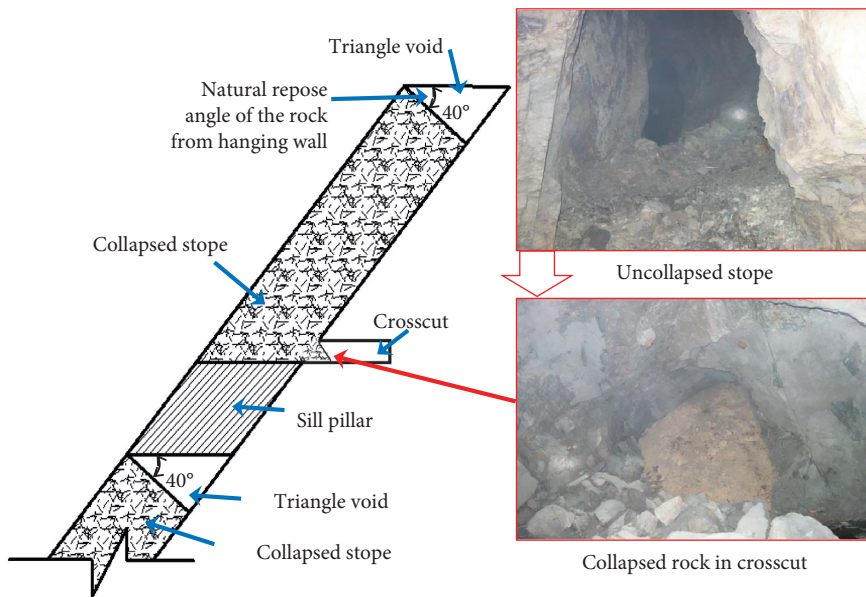
FIGURE 9: The shape of the collapsed stope in the west of 888m middle section to 808m middle section.

backfilling treatment is determined as follows: the overall sequence of backfilling treatment is from bottom to top, i.e., backfilling the 768 m level first, followed by backfilling the 808 m level, 848 m level, and 888m level. Meanwhile, because of the large thickness of 27 to 33 orebody, the mined-out area of 27 to 33 lines is firstly backfilled in the west area, and then, the residual mining is gradually backfilled in the two wings. There is a broken zone in lines 53 to 57. The goaf at the footwall of the broken zone is, firstly, backfilled in the

eastern area, and the residual mining is gradually backfilled from the broken zone eastward. Consistent with the field monitoring results of the deformation rate of a nearby rock mass in stopes 7661 and 7635, the deformation rate of the nearby rock mass belongs to the category of medium strain rate (0.3% to 1.5%/day). As said by the author's earlier research results, when the thickness of the orebody is less than or equal to 6 m, it is necessary to analyze whether the damage and failure of the cemented backfill will occur under

the condition of a medium strain rate. If the damage/failure is large, the uncemented backfill rather than the cemented backfill should be considered. As the thickness of the orebody is larger than 6 m, cemented backfill should be selected. At this time, the initial stiffness and the minimum shrinkage strain/drainage of the backfill should be taken into account. The statistical results of the backfill types of each goaf are shown in Table 6.

4.2. Performance Evaluation of Cemented Tailings Backfill. Because of low-temperature and high-cold conditions in the mining area, the lowest temperature reaches $-37.4°C$, which can cause wellbore icing and surface pipeline cracking. Therefore, the influence of the low-temperature environment conservation on the backfill strength should be considered. According to the climatic conditions and physical and chemical properties of the tailings in the Alhada lead-zinc mine, the graded tailings are selected as the filling aggregate, and pulping is made in a low-temperature environment. The useful metal grade in the tailings of Alhada lead-zinc mine is lower than the lowest optional grade. The content of SiO_2 and Al_2O_3 in the tailings is as high as 56.24% and 17.82%, respectively. The total content of SiO_2, Al_2O_3, and Fe_2O_3 is as high as 85%, showing high potential cementation. However, there is a certain amount of sulfur in the tailings, and the mechanical properties of the cemented backfill with the cementing materials need to be determined by test. Thus, the slurry was poured into the standard metal test mold of $7.07 \times 7.07 \times 7.07$ cm and put into the curing box for low-temperature environment curing (curing temperature 7°C, humidity 90%). After reaching the specified curing age, the mold was removed, and the uniaxial compressive strength was tested on a special loading machine. The strength of the backfill with the cement-sand ratio of 1 : 4 to 1 : 10 and the solid content of 65% to 75% of the graded tailings in the Alhada lead-zinc mine was studied (including the ages of 7, 14, 28, and 60 days). At the same time, the bleeding performance of the filling slurry of the classified tailings of Alhada lead-zinc mine with a cement-sand ratio of 1 : 4 to 1 : 10 and a solid content of 65% to 75% was determined. Figure 10 indicates the obtained results.

As the cement-tailings ratio decreased, the compressive strength of the cemented backfill decreased clearly. For example, when the solid content is 75%, the internal structure of 1 : 6 sample is relatively dense. Its compressive strength can reach approximately 1.64 MPa at 28 days, while the compressive strength of 1 : 10 sample at 28 days is only 0.48 MPa, and there are stratification and segregation phenomena. The strength of the sample increases with the increase of curing time. For example, the strength of each solid content for 28 days increases significantly compared to that for 7 days. The higher the solid content, the greater the increase range, indicating that the strength increases significantly and lasts for a long time when the cement content in the backfill is larger, which is beneficial to the subsequent backfill.

The strength of backfill is closely related to its solid content. The greater the slurry solid content, the larger the backfill strength [39]. The test results show that when the slurry solid content surges from 65% to 75%, the strength of the cemented backfill up to 28 days can increase by 2 to 3 times. However, because of the strong workability and viscosity of the cemented-tailings backfill, too high a solid content will make pipeline transportation difficult. The test results show that when the cement-sand ratio is less than 1 : 6, even if the solid content increases, the strength of the backfill cannot reach 1 MPa in 28 days. When the cement-sand ratio is 1 : 8 and 1 : 10, it cannot be used as the cementing layer, which will affect the operation of the mechanical and human activity on the backfill.

The nonuniformity coefficient of the tailings of Alhada lead-zinc mine is 16.5. The particle size distribution of the tailings varies greatly. Approximately 67% of the tailings particles were less than 75 μm. The tailings of Alhada lead-zinc mine belong to silt, which may lead to slime if it is backfilled into the stope. The nonuniformity coefficient of the graded tailings is 3.9, and the particle size distribution of the tailings is close to the ideal nonuniformity coefficient of 4 to 5. It belongs to uniform fine tailings, and the mud content is less than 1%. It is easy to be mixed during pulping, is convenient for pipeline transportation, and is dehydrated rapidly after backfilling in the stope, which is conducive to reducing cement segregation.

The permeability coefficient of Alhada lead-zinc tailings is 0.0702 cm/h at 5 °C and only 0.2376 cm/h even at 20 °C. It cannot meet the requirement of 10 cm/h. It is not conducive to the rapid dehydration and hardening of the backfill and is not suitable for filling aggregate. The permeability of the graded tailings is 3.1428 cm/h at 5 °C and 14.04 cm/h at 20 °C. Although the low-temperature environment has a certain influence on the permeability of the graded tailings, it maintains a good dehydration performance and fast initial setting after entering the stope.

4.3. Industrial Tests. The backfill slurry is transported by the pipeline. To make full use of mine tunnels, backfill pipes are arranged in two directions from the surface backfill station outlet to 2# main shaft and 57 line vents through the surface. The total length of the pipes from the backfill station to 2# main shaft is 680 m, and the vertical height is 57 m. The total length of the backfill station to 57 line vents is 937 m, and the vertical height is 67 m. See Figure 11(a) for the surface layout of the pipe. The backfill treatment of the mined-out area at 768 m level was, firstly, carried out in the Alhada lead-zinc mine. Preparation work was made for the backfill of the 25th to 35th line goaf in the 768m level. 15 backfill holes were constructed and 18 slab walls were erected. The backfill pipe extends downward from the cable that runs through the surface to the 808 m level, and the feeding port of the pipe is connected with the filling hole of ø 100 mm (Figure 11(b)). Considering the backfill cost, three types of cement/sand ratio of backfill materials are adopted: 1 : 6, 1 : 8, and pure tailings. The bottom layer of the goaf was, firstly, backfilled with a backfill slurry with a cement-sand ratio of 1 : 6 to a vertical height of 1 m. After that, the whole goaf was backfilled with a cement-sand ratio of 1 : 8. The solid content

TABLE 6: Statistical results of the types of backfill (collapsed rock and cemented/uncemented backfill) in each middle goaf.

Stope number	The ratio of the volume of the collapsed waste rock to the total volume of the goaf (%)	Types of backfill	Stope number	The ratio of the volume of the collapsed waste rock to the total volume of the goaf (%)	Types of backfill
768–1#	49	Cemented backfill	848–12#	94	Cemented backfill
768–2#	49	Cemented backfill	848–13#	94	Cemented backfill
768–3#	49	Cemented backfill	848–14#	94	Cemented backfill
768–4#	49	Cemented backfill	848–15#	94	Cemented backfill
768–5#	49	Uncemented backfill	848–16#	94	Cemented backfill
768–6#	49	Uncemented backfill	848–17#	94	Cemented backfill
768–7#	49	Cemented backfill	848–18#	94	Cemented backfill
768–8#	34	Cemented backfill	848–19#	94	Uncemented backfill
768–9#	34	Cemented backfill	848–20#	94	Cemented backfill
808–1#	94	Cemented backfill	848–21#	94	Cemented backfill
808–2#	94	Cemented backfill	848–22#	0	Uncemented backfill
808–3#	94	Cemented backfill	848–23#	0	Cemented backfill
808–4#	94	Uncemented backfill	848–24#	0	Uncemented backfill
808–5#	94	Cemented backfill	848–25#	0	Cemented backfill
808–6#	94	Cemented backfill	848–26#	0	Cemented backfill
808–7#	94	Cemented backfill	888–1#	94	Uncemented backfill
808–8#	94	Cemented backfill	888–2#	94	Cemented backfill
808–9#	94	Uncemented backfill	888–3#	94	Uncemented backfill
808–10#	94	Uncemented backfill	888–4#	94	Uncemented backfill
808–11#	94	Cemented backfill	888–5#	94	Cemented backfill
808–12#	94	Cemented backfill	888–6#	94	Uncemented backfill
808–13#	94	Cemented backfill	888–7#	94	Uncemented backfill
808–14#	94	Uncemented backfill	888–8#	94	Cemented backfill
808–15#	94	Uncemented backfill	888–9#	94	Uncemented backfill
808–16#	94	Uncemented backfill	888–10#	94	Uncemented backfill
808–17#	94	Uncemented backfill	888–11#	94	Cemented backfill
808–18#	0	Uncemented backfill	888–12#	94	Uncemented backfill
808–19#	0	Uncemented backfill	888–13#	94	Cemented backfill
808–20#	0	Cemented backfill	888–14#	94	Uncemented backfill

TABLE 6: Continued.

Stope number	The ratio of the volume of the collapsed waste rock to the total volume of the goaf (%)	Types of backfill	Stope number	The ratio of the volume of the collapsed waste rock to the total volume of the goaf (%)	Types of backfill
808–21#	94	Cemented backfill	888–15#	94	Cemented backfill
808–22#	94	Cemented backfill	888–16#	94	Cemented backfill
808–23#	0	Cemented backfill	888–17#	0	Uncemented backfill
808–24#	0	Cemented backfill	888–18#	0	Uncemented backfill
808–25#	0	Uncemented backfill	888–19#	0	Uncemented backfill
808–26#	0	Uncemented backfill	888–20#	0	Cemented backfill
808–27#	0	Uncemented backfill	888–21#	0	Uncemented backfill
808–28#	0	Uncemented backfill	888–22#	0	Cemented backfill
848–1#	94	Cemented backfill	888–23#	0	Cemented backfill
848–2#	94	Cemented backfill	888–24#	0	Uncemented backfill
848–3#	94	Cemented backfill	888–25#	0	Cemented backfill
848–4#	94	Cemented backfill	888–26#	0	Uncemented backfill
848–5#	94	Cemented backfill	888–27#	0	Uncemented backfill
848–6#	94	Cemented backfill	888–28#	0	Uncemented backfill
848–7#	94	Uncemented backfill	888–29#	0	Uncemented backfill
848–8#	94	Uncemented backfill	888–30#	0	Cemented backfill
848–9#	94	Uncemented backfill	888–31#	0	Cemented backfill
848–10#	94	Cemented backfill	888–32#	0	Uncemented backfill
848–11#	94	Cemented backfill	—	—	—

of the slurry is changed between 65% and 70%. During the backfill process, the drainage wall was closely observed as shown in Figure 11(c). The feeding point and mine backfill amount were adjusted according to the drainage speed, and the backfill method of "multipoint feeding, multiple times with more and less amount" was adopted.

Using the performed field mine backfill industrial testing, only 22,500 m³ of cavity backfill was completed in lines 25 to 35 of the 768 m level. The maximum backfill amount of a single goaf in a single day reaches 1240 m³ with an average backfill capacity of 60 m³ to 80 m³ per hour. The vertical height of packing is 35 m. No pipe blockage, wall collapse, or slurry leakage occurred during the mine backfill process.

According to the disclosure of 808 m construction goaf combined roadway, the mine backfill material has good flatness and high compactness. It can meet the requirements of goaf treatment and later sill pillar recovery.

5. Evaluation of the Effect of Goaf Treatment by Backfill

In this study, the numerical simulation method was employed to better analyze the damage and failure of the surrounding rock mass in goaf, and the surface subsidence monitoring method was used to analyze the surface
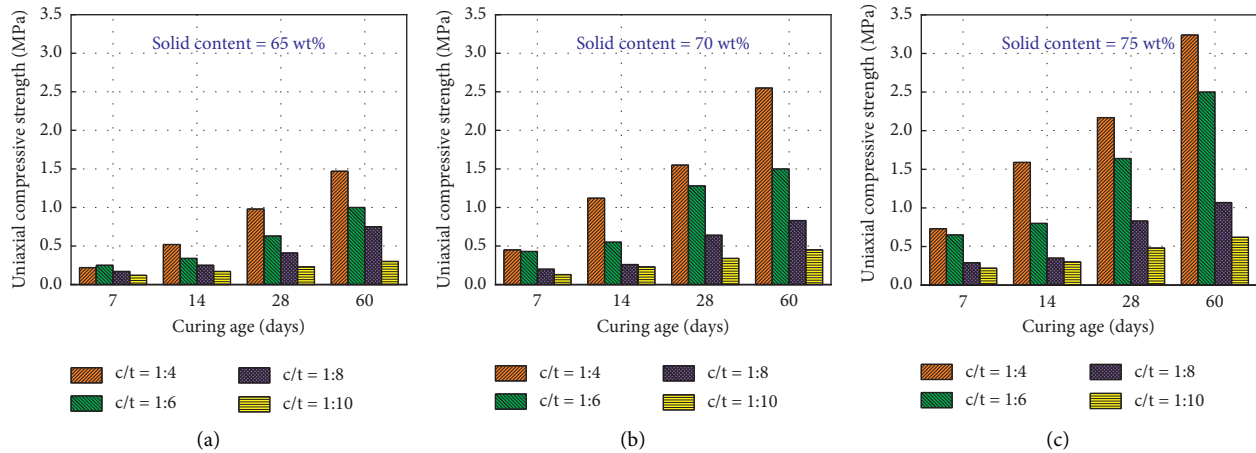
FIGURE 10: Evolution of the strength of cemented backfill under the effects of solid content and cement-tailings ratio.
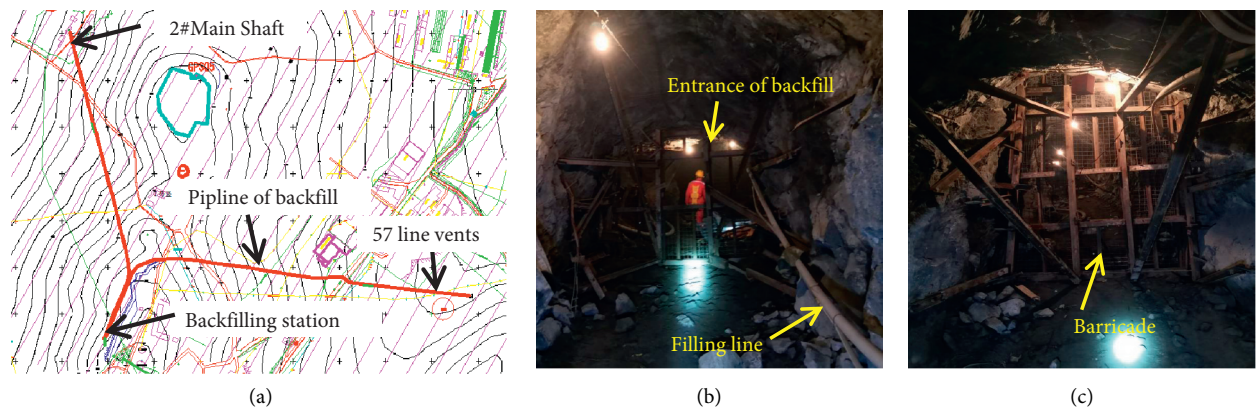
FIGURE 11: Industrial test. (a) The layout of backfilling pipeline at surface; (b) entrance of backfill at a goaf; (c) construction of barricades.

subsidence to evaluate the effectiveness of the filling treatment of a large goaf. For details, see sections 5.1 and 5.2.

5.1. Distribution of Surrounding Rock Failure Zone in Goaf.
The amount of backfill used in the mined-out area is given in Table 6. It can be seen that every stope is not regular equally in terms of the mine backfill process as demonstrated clearly in Figure 12. However, the volume of backfill in the stope is carried out strictly in accordance with the actual situation of the surrounding rock mass. For example, some stopes have triangular goaf, some use cemented backfill, some use uncemented backfill, and the influence of collapsed waste rock caused by the unstable surrounding rock is considered during the backfill process.

As observed from Figure 13, the surrounding rock of the goaf without the backfill treatment has many failure areas, and the rock pillars between the goaf have large failure areas. One can observe that the failure area of the nearby rock of the goaf is significantly reduced after using the backfill method per the deformation state of the nearby rock mass, and the backfill treatment of the goaf significantly improves the stability of the surrounding rock mass. It shows that the backfill technology adopted in this study has a sizeable

influence in governing the stability of the nearby rock mass in the goaf.

5.2. Monitoring Scheme and the Results of Surface Subsidence.
To certify the secure production and smooth progress of backfilling treatment, a settlement monitoring system is set up on the surface. The monitoring scheme uses SD-226 hydraulic static level that is composed of a liquid reservoir, imported high-precision core, specially customized circuit module, protective cover, and other components. Four core cables are used to connect each static level in parallel, and then, they are connected to the data gaining port. Two of the four core cables are used for the power supply of the sensor, and the other two are used for data transmission. The data collection port has a built-in wireless module that conveys the monitored data to the cloud data service center through the GPRS network. The monitoring center server accesses the cloud data service center using the HTTP transmission protocol, and the users can query, manage, and maintain projects.

The diameter of the collapse pit at No. 25 exploration line is approximately 125 m and that at No. 29 exploration line is approximately 70 m. Considering the scope of the surface
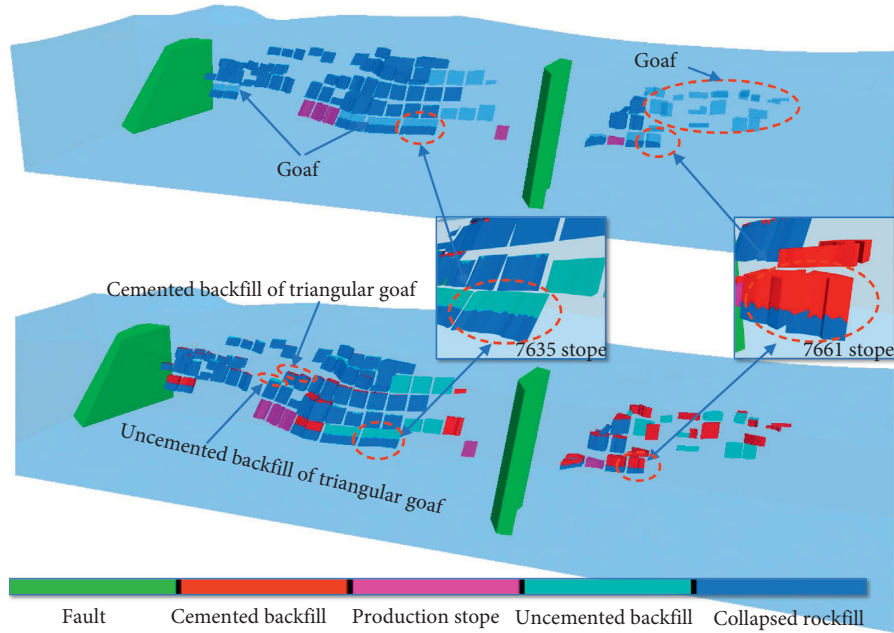
FIGURE 12: Results of precise backfill in large goaf group.

moving belt, the monitoring range of the area is determined from exploration line 23 to exploration line 31. Ten measuring points are arranged along the 300 m (S1 monitoring line) and 170 m (S2 monitoring line) of the orebody strike to monitor the settlement rule of the surface moving belt as shown in Figure 14. The surface liquid static level monitoring system was installed and officially put into operation after debugging.

Figure 15(a) shows the accumulated settlement value of each measuring point in S1. The accumulated settlement value of N2–N5 measuring point fluctuates at 0 cm, and no surface settlement occurs in this monitoring area. The accumulated settlement value of N10 measurement point fluctuates at 2 cm. The N7–N9 measuring point deformation value with time is increasing and then tends to attain a stable state, N7 measuring point accumulated settlement value is about 5.2 cm, N8 measuring point accumulated settlement value is about 7.9 cm, and N9 measuring point accumulated settlement value is about 5.7 cm.

Figure 15(b) shows the accumulated settlement value of each measuring point in S2. The accumulated settlement value of N2~N6 measuring point fluctuates at 0 cm, and no surface settlement occurs in this monitoring area. N10 began to settle on September 2, and the maximum accumulated settlement value was 8.5 cm. The deformation value of N7–N9 measuring points increases with time and begins to fluctuate periodically on August 10. Finally, the three measuring points tend to stabilize at the settlement value of 8 cm.

The instability of surrounding rock is serious, and the failure areas between mined-out areas are nearly connected

Plane1, x = 500 m   Plane2, x = 1000 m   Plane3, x = 1300 m   Plane4, x = 1800 m

Zone state

- None
- shear-n shear-p
- shear-n shear-p tension-p
- shear-p
- shear-p tension-p
- tension-n shear-p tension-p
- tension-n tension-p
- tension-p

(a)

The failure area between surrounding rock and mined-out area is significantly reduced

Plane1, x = 500 m   Plane2, x = 1000 m   Plane3, x = 1300 m   Plane4, x = 1800 m

Zone state

- None
- shear-n shear-p
- shear-n shear-p tension-p
- shear-p
- shear-p tension-p
- tension-n shear-p tension-p
- tension-n tension-p
- tension-p

(b)

FIGURE 13: The failure area of the surrounding rock of the large goaf group using the backfill method and otherwise. (a) Large goaf group that is not backfilled and (b) backfilled per the specific conditions of the surrounding rock mass.

Layout of surface subsidence monitoring points

Hydrostatic level system
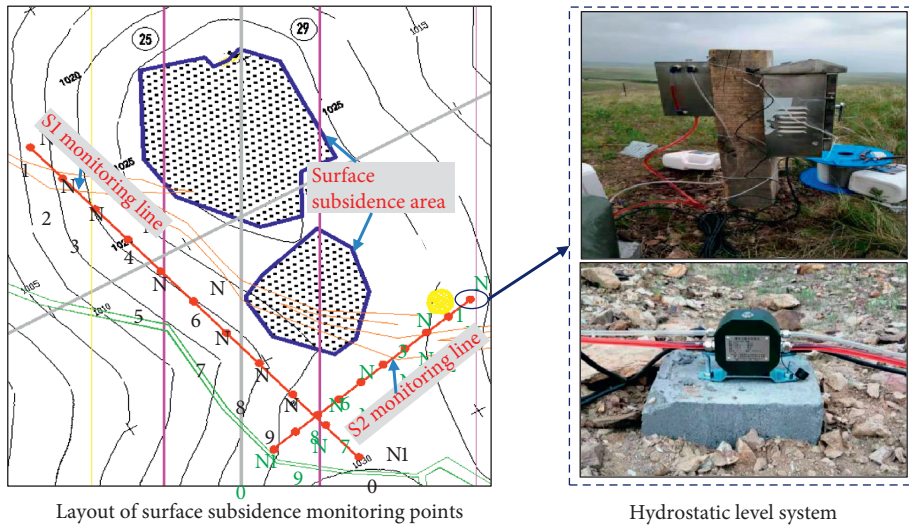
FIGURE 14: Layout of surface subsidence monitoring points and Hydrostatic Level System.

(a)

(b)
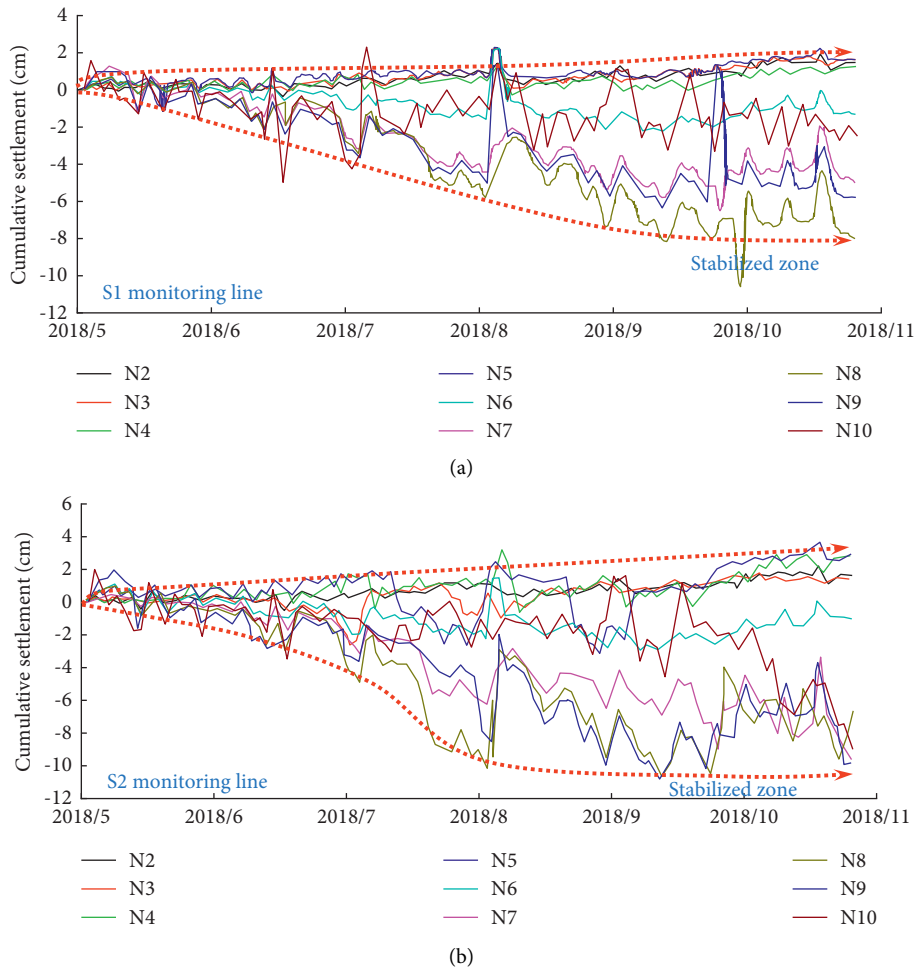
FIGURE 15: Cumulative settlement of each measuring point on (a) S1 and (b) S2 monitoring line.

6. Conclusions

In this study, three-dimensional modeling, laboratory test, industrial test, and field monitoring were used to study the treatment scheme of a large goaf group in the Alhada lead-zinc mine using precise backfill technology. The specific conclusions are as follows:

(i) The stability of the large goaf group can be comprehensively evaluated by employing the modified Mathews stability diagram system. The volume of each goaf to be backfilled can be quantitatively analyzed in combination with theoretical analysis and three-dimensional laser scanning technology.

(ii) The final collapse form of the western stope is caused by the instability of the upper wall of the goaf, and there is a triangular goaf under the effect of the western goaf and the eastern broken zone. The volume of the triangular goaf accounts for about 5.8% of the stope volume. The residual mined-out area volume in the western section of 768 m accounts for 50.9% of the stope volume. The volume of the residual mined-out area outside the influence area of the broken zone in the eastern area accounts for 65.9% of the total volume of the stope.

(iii) The precise backfill technology adopted in this study can deal with a large goaf group well and significantly reduce the damaged area of the surrounding rock mass in the goaf and the settlement of the surface. Also, it can reduce the cost of backfill treatment using cemented backfill and uncemented backfill together. The monitoring results showed that the surface maximum accumulated subsidence value is about 8.5 cm, and in the end, the surface vertical deformation tends to be stable after using the backfill technology.

Data Availability

All data, models, or codes that support the findings of this study are available from the corresponding author upon reasonable request.

Conflicts of Interest

The authors declare no conflicts of interest.

Acknowledgments

References

[1] Y. M. Wang, M. Q. Huang, A. X. Wu, G. H. Yao, and K. J. Hu, "Rock backfill and hazard control of abandoned stopes: a case study," *Applied Mechanics and Materials*, vol. 368-370, pp. 1726–1731, 2013.

[2] X. Zhao, A. Fourie, and C.-C. Qi, "Mechanics and safety issues in tailing-based backfill: a review," *International Journal of Minerals, Metallurgy and Materials*, vol. 27, no. 9, pp. 1165–1178, 2020.

[3] X. Liu, J. Ning, Y. Tan, Q. Xu, and D. Fan, "Coordinated supporting method of gob-side entry retaining in coal mines and a case study with hard roof," *Geomechanics and Engineering*, vol. 15, no. 6, pp. 1173–1182, 2018.

[4] U. G. Akkaya, K. Cinku, and E. Yilmaz, "Characterization of strength and quality of cemented mine backfill made up of lead-zinc processing tailings," *Frontiers in Materials*, vol. 8, Article ID 740116, 2021.

[5] S. Qin, S. Cao, E. Yilmaz, and J. Li, "Effects of types and geometric shapes of 3D printed polymeric lattice on ductility performance of cementitious backfill composites," *Construction and Building Materials*, vol. 307, Article ID 124973, 2021.

[6] W. Y. Lv and Z. H. Zhang, "Research on the belt loader waste rock gravity backfill mining technology," *Applied Mechanics and Materials*, vol. 253, pp. 1036–1039, 2013.

[7] G. L. Xue, E. Yilmaz, W. D. Song, and S. Cao, "Fiber length effect on strength properties of polypropylene fiber reinforced cemented tailings backfill specimens with different sizes," *Construction and Building Materials*, vol. 241, Article ID 118113, 2020.

[8] L. Cui and M. Fall, "Multiphysics modeling of arching effects in fill mass," *Computers and Geotechnics*, vol. 83, pp. 114–131, 2017.

[9] S. Yin, Y. Shao, A. Wu, H. Wang, X. Liu, and Y. Wang, "A systematic review of paste technology in metal mines for cleaner production in China," *Journal of Cleaner Production*, vol. 247, Article ID 119590, 2020.

[10] C. Zhang, S. Tu, and Y. Zhao, "Compaction characteristics of the caving zone in a longwall goaf: a review," *Environmental Earth Sciences*, vol. 78, no. 1, p. 27, 2019.

[11] F. Ren, Y. Zhou, R. He, J. Cao, and K. Zou, "Similarity model test on the spatiotemporal evolution law of deformation and failure of surrounding rock-induced caving in multi-mined-out areas," *Advances in Civil Engineering*, vol. 2021, Article ID 1224658, 15 pages, 2021.

[12] S. Cao, E. Yilmaz, G. L. Xue, and W. D. Song, "Assessment of acoustic emission and triaxial mechanical properties of rock-cemented tailings matrix composites," *Advances in Materials Science and Engineering*, vol. 2019, Article ID 6742392, 12 pages, 2019.

[13] W. Bao, Z. Ma, H. Wang, J. Ren, Y. Huang, and B. Liang, "Integrated treatment technology of storage-mining inclined goaf under expressway," *Advances in Civil Engineering*, vol. 2020, Article ID 8822964, 19 pages, 2020.

[14] X. Li, X. Guo, and G. Sun, "Grouting reinforcement mechanism and multimodel simulation analysis of longwall goaf," *Geofluids*, vol. 2021, Article ID 9943596, 13 pages, 2021.

[15] J.-X. Zhang, P. Huang, Q. Zhang, M. Li, and Z.-W. Chen, "Stability and control of room mining coal pillars-taking room mining coal pillars of solid backfill recovery as an example," *Journal of Central South University*, vol. 24, no. 5, pp. 1121–1132, 2017.

[16] X. Li, D. Wang, C. Li, and Z. Liu, "Numerical simulation of surface subsidence and backfill material movement induced by underground mining," *Advances in Civil Engineering*, vol. 2019, Article ID 2724370, 17 pages, 2019.

[17] T. Kostecki and A. J. S. Spearing, "Influence of backfill on coal pillar strength and floor bearing capacity in weak floor conditions in the Illinois Basin," *International Journal of Rock Mechanics and Mining Sciences*, vol. 76, pp. 55–67, 2015.

[18] E. Yilmaz, T. Belem, M. Benzaazoua, A. Kesimal, B. Ercikdi, and F. Cihangir, "Use of high-density paste backfill for safe disposal of copper/zinc mine tailings," *Mineral Resources Management*, vol. 27, no. 3, pp. 81–94, 2011.

[19] P. Yang, L. Li, M. Aubertin, M. Brochu-Baekelmans, and S. Ouellet, "Stability analyses of waste rock barricades designed to retain paste backfill," *International Journal of Geomechanics*, vol. 17, no. 3, Article ID 04016079, 2016.

[20] F. Feng, D. Y. Li, X. B. Li, Z. P. Guo, S. F. Wang, and Y. Chen, "Novel underhand cut-and-fill stoping method and mechanical analysis of overlying backfill," *International Journal of Geomechanics*, vol. 17, no. 7, Article ID 04017004, 2017.

[21] C. Qi and A. Fourie, "Numerical investigation of the stress distribution in backfilled stopes considering creep behaviour of rock mass," *Rock Mechanics and Rock Engineering*, vol. 52, no. 9, pp. 3353–3371, 2019.

[22] Y. Ohnishi, T. Sasaki, T. Koyama, I. Hagiwara, S. Miki, and T. Shimauchi, "Recent insights into analytical precision and modelling of DDA and NMM for practical problems," *Geomechanics and Geoengineering*, vol. 9, no. 2, pp. 97–112, 2014.

[23] Y. Zhu, Y. Li, Z. Hao, L. Luo, J. Luo, and L. Wang, "An analytical solution for the frost heaving force and displacement of a noncircular tunnel," *Computers and Geotechnics*, vol. 133, Article ID 104022, 2021.

[24] P. P. Nomikos, A. I. Sofianos, and C. E. Tsoutrelis, "Structural response of vertically multi-jointed roof rock beams," *International Journal of Rock Mechanics and Mining Sciences*, vol. 39, no. 1, pp. 79–94, 2002.

[25] C. Qiao, Y.-H. Guo, and C.-H. Li, "Study on rock burst prediction of deep buried tunnel based on cusp catastrophe theory," *Geotechnical & Geological Engineering*, vol. 39, no. 2, pp. 1101–1115, 2021.

[26] Q. Jiang, G. Su, X.-T. Feng, G. Chen, M.-Z. Zhang, and C. Liu, "Excavation optimization and stability analysis for large underground caverns under high geostress: a case study of the Chinese Laxiwa project," *Rock Mechanics and Rock Engineering*, vol. 52, no. 3, pp. 895–915, 2019.

[27] R. Habibi, H. Moomivand, M. Ahmadi, and A. Asgari, "Stability analysis of complex behavior of salt cavern subjected to cyclic loading by laboratory measurement and numerical modeling using LOCAS (case study: nasrabad gas storage salt cavern)," *Environmental Earth Sciences*, vol. 80, no. 8, pp. 1–21, 2021.

[28] W. Yang, Y. Jiang, X. Gu, Z. Wang, Y. Shang, and W. Zeng, "Deformation mechanism and mechanical behavior of tunnel within contact zone: a case study," *Bulletin of Engineering Geology and the Environment*, vol. 80, no. 7, pp. 5657–5673, 2021.

[29] H. S. Mitri, R. Hughes, and Y. Zhang, "New rock stress factor for the stability graph method," *International Journal of Rock Mechanics and Mining Sciences*, vol. 48, no. 1, pp. 141–145, 2011.

[30] L. Yang, W. Xu, E. Yilmaz, Q. Wang, and J. Qiu, "A combined experimental and numerical study on the triaxial and dynamic compression behavior of cemented tailings backfill," *Engineering Structures*, vol. 219, Article ID 110957, 2020.

[31] E. Yilmaz, T. Belem, M. Benzaazoua, and B. Bussiere, "Assessment of the modified CUAPS apparatus to estimate in situ properties of cemented paste backfill," *Geotechnical Testing Journal*, vol. 33, no. 5, pp. 351–362, 2010.

[32] J. A. Vallejos, A. Delonca, and E. Perez, "Three-dimensional effect of stresses in open stope mine design," *International Journal of Mining, Reclamation and Environment*, vol. 32, no. 5, pp. 355–374, 2018.

[33] H. Jia, K. Guan, W. Zhu, H. Liu, and X. Liu, "Modification of rock stress factor in the stability graph method: a case study at the Alhada Lead-Zinc Mine in Inner Mongolia, China," *Bulletin of Engineering Geology and the Environment*, vol. 79, no. 6, pp. 3257–3269, 2020.

[34] Y. Potvin, "Empirical Open Stope Design in Canada," Doctoral Thesis, The University of British Columbia, Vancouver, Canada, 1988.

[35] F. T. Suorineni, "A critical review of the stability graph method for open stope design," in *Proceedings of the MassMin 2012*, pp. 10–14, Canadian Institute of Mining, Metallurgy and Petroleum, Sudbury, Canada, June 2012.

[36] F. T. Suorineni, "The stability graph after three decades in use: experiences and the way forward," *International Journal of Mining, Reclamation and Environment*, vol. 24, no. 4, pp. 307–339, 2010.

[37] Q. Liu, J. Liu, Y. Pan, X. Kong, and K. Hong, "A case study of TBM performance prediction using a Chinese rock mass classification system - h," *Tunnelling and Underground Space Technology*, vol. 65, pp. 140–154, 2017.

[38] N. Barton, "Some new Q-value correlations to assist in site characterisation and tunnel design," *International Journal of Rock Mechanics and Mining Sciences*, vol. 39, no. 2, pp. 185–216, 2002.

[39] M. Benzaazoua, T. Belem, and E. Yilmaz, "Novel lab tool for paste backfill," *Canadian Mining Journal*, vol. 127, no. 3, pp. 31–33, 2006.

Research Article

Subsidence Control Design Method and Application to Backfill-Strip Mining Technology

Xiaojun Zhu [iD],[1,2,3] **Feng Zha** [iD],[1] **Guangli Guo** [iD],[4] **Pengfei Zhang** [iD],[1] **Hua Cheng** [iD],[1] **Hui Liu** [iD],[1] **and Xiaoyu Yang** [iD][5]

[1]*Anhui Province Engineering Laboratory for Mine Ecological Remediation, Anhui University, Hefei, China*
[2]*Engineering Research Center of Coal Industry for Space Collaborative Monitoring of Mine Environment and Disaster, Huainan, China*
[3]*Huaibei Bureau of Natural Resources and Planning, Huaibei, China*
[4]*School of Environment Science and Spatial Information, China University of Mining and Technology, Xuzhou, China*
[5]*Department of Engineering Management, Hefei College of Finance and Economics, Hefei, China*

Correspondence should be addressed to Xiaojun Zhu; zhuxiaojunahu@126.com and Pengfei Zhang; zhangpf004@126.com

Received 18 August 2021; Accepted 16 September 2021; Published 12 October 2021

Academic Editor: Haiqiang Jiang

Intensive and massive coal mining causes a series of geological hazards and environmental problems, especially surface subsidence. At present, two major types of subsidence control technology are applied: backfilling technology and partial mining technology. However, the cost of backfill mining is high and partial mining has a low recovery ratio. Therefore, the backfill-strip mining is used to solve the problems of high cost and shortage of filling materials in coal mines at present. A subsidence control design method of backfill-strip mining was proposed in this paper based on the subsidence control effects and economic benefits. First, the stability of the composite support pillar of the filling body and coal pillars in the backfill-strip mining is analyzed, and the values of the main subsidence influencing factors that include the filling material, the size of the backfilling working face, caving mining face, and residual coal pillar are preliminarily determined. Then, the surface movement and deformation are predicted based on the equivalent superposition probability integral method (PIM). The subsidence influencing factors are optimized and determined by comparing the requirements of the safety fortification index of the antideformation ability of surface buildings, resource recovery rate, and coal mining cost. Finally, the mining scheme design parameters of the backfill-strip mining technology are determined. This method is applied in the subsidence control design of backfill-strip mining in the Ezhuang coal mine. Research results show that backfill-strip mining can ensure the safety of surface buildings, increase the resource recovery rate, and reduce coal mining costs through the reasonable design of this method. This study can provide scientific guidance for subsidence disaster control, prevention, and engineering design in backfill-strip mining.

1. Introduction

When resources are mined, a large number of goafs are produced underground, and the stress balance inside the rock is disturbed. This leads to the overburden stratum bending and breaking, resulting in surface subsidence [1, 2]. Surface subsidence caused by underground coal mining is a global problem and leads to damage to infrastructure, buildings, roads, and drainage systems [3–6]. The problems of surface subsidence have been reported in the United

States, China, Australia, Poland, Czech Republic, and other countries. In recent decades, with increased mining, the associated surface subsidence problems in China have become progressively more serious. Surface subsidence is the most common cause of disasters in mining areas. According to statistics, the surface subsidence area due to coal mining in China has reached $6 \times 10^3 \, \text{km}^2$, and the area is increasing by $240 \, \text{km}^2$ every year [7–9].

Many mining techniques were applied to control surface subsidence to achieving the coordinated and sustainable

development of coal resources exploitation and environmental protection. The backfilling mining technology based on filling body support mainly includes gob, caving zone, and separated-bed filling [10–12]. However, this technology has the disadvantages of high filling costs and backfill material shortage [13–16]. The partial mining achieves the goal of controlling surface subsidence through the support of coal pillars and reducing the mining area. However, the partial mining wastes a large amount of coal resources because its coal resource recovery rate is too low [17–19].

Backfill-strip mining is a partial backfilling technology that combines the advantages of backfill mining and partial mining, which can effectively control surface subsidence and reduce costs. In this technology, longwall partial backfill mining is conducted first. After the backfill materials achieve a certain bearing capacity, the residual coal pillar is recycled. This mining process eventually forms a combined support pillar of the filling body and the coal pillar (CSP) to support the overlying strata and achieve the goal of subsidence control. Figure 1 shows the backfill-strip mining diagram. The increase in environmental constraints has made the advantages of backfill-strip mining increasingly prominent and facilitated its application in several coal mines in China, such as Daizhuang Coal Mine, Fucun Coal Mine, Xuchang Coal Mine, Xingdong Mining, and Handan Coal Mine.

Since backfill-strip mining method was proposed, it has undergone continuous development. Backfill-strip mining uses coal gangue and other solid wastes as the main backfill material to fill the underground mine; on the one hand, it can reduce waste discharge such as gangue; on the other hand, it can be applied in coal seam extraction under building due to the subsidence control effect and achieves coal recycling economy and green mining [20]. The backfill materials commonly used in coal mine mainly include gangue, fly ash, paste, and high-water material [21]. Compared with the full backfilling of the goaf, when decreasing the backfill range of backfill-strip mining, the backfill cost is greatly reduced, and the reduction of the backfill workload also reduces the impact on the normal mining of the working face and improves the efficiency of the mining work [22, 23].

In recent years, some subsidence control design methods were proposed according to the corresponding mining subsidence control techniques. The regulation [24] promulgated by China Coal research institute describes the subsidence control design method of strip mining, and the stability of coal pillar, the influence of surface subsidence, and recovery rate are considered in this method. Wang [25] proposed the subsidence control design method of backfill mining, and the filling quality, the influence of surface subsidence, and economic benefits are considered in this method. Backfill-strip mining combines the advantages of backfill mining and partial mining, but the control mechanisms of the strata subsidence between backfill mining, strip mining, and backfill-strip mining are not the same. The subsidence effect of backfill-strip mining is influenced by many factors, among which the stability of the CSP is the key to the success of backfill-strip mining. The CSP in the backfill-strip mining is affected by the filling material and the

size of the backfilling working face, caving mining face, and residual coal pillar [21, 26]. However, CSP is different from coal pillar or fulling body because of different material properties and structure. Therefore, the subsidence control design method of backfill-strip mining cannot completely copy those of strip mining and backfill mining. A new subsidence control design method of backfill-strip mining was proposed in this paper based on the subsidence control effects and economic benefits.

The rest of the paper is organized as follows. The subsidence control design method of backfill-strip mining is introduced in detail to determine the size of the backfilling working face, caving mining face, and residual coal pillar in Section 2. An engineering case of the subsidence control design of backfill-strip mining is shown in Section 3. The subsidence control effect and economic benefit of backfill mining, strip mining, and caving mining methods are contrastively analyzed in Section 4. Section 5 presents the conclusions.

2. Subsidence Control Design Method of Backfill-Strip Mining

2.1. Subsidence Control Design Principles of Backfill-Strip Mining. The subsidence control design of backfill-strip mining is determined by three aspects to meet the requirements of subsidence control and cost reduction: the stability of composite support, the surface movement and deformation value, and the economic benefit. Therefore, the following principles should be followed in the design process:

(1) The primary principle in the subsidence control design of backfill-strip mining is to ensure that the surface subsidence is controlled within the safety fortification index of the surface building. This is the most important principle of subsidence control in backfill-strip mining.

(2) The second principle is to ensure the stability of the CSP. The CSP is the main support of the overlying strata. The stability of the CSP is the core of backfill-strip mining, and it is also the premise of using the equivalent superposition PIM to predict the surface subsidence. Therefore, the subsidence control design of backfill-strip mining must ensure the stability of CSP.

(3) On the premise of ensuring the above two principles, the width of the residual coal pillars and the backfill working face are reduced, and that of the caving mining working face is increased to improve the recovery rate of coal resources, minimize the mining cost, and achieve better economic benefits.

2.2. Subsidence Control Design Flow of Backfill-Strip Mining. In Figure 2, the subsidence control design method of backfill-strip mining is divided into 6 steps as follows:

(1) First, the fortification index of surface movement and deformation is determined according to the
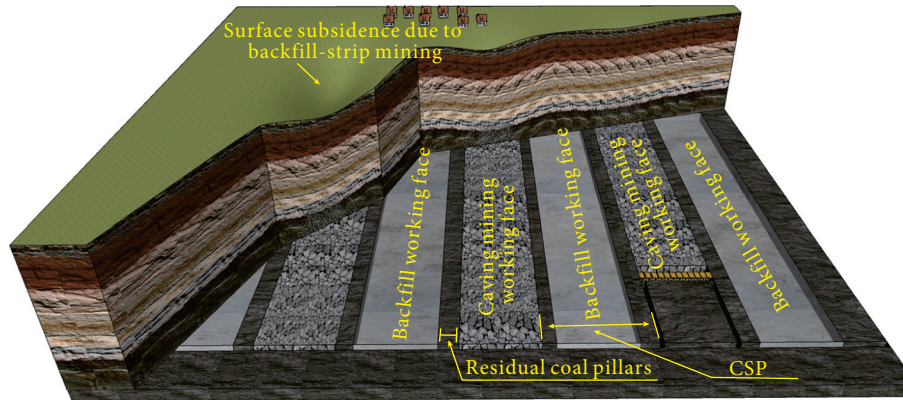
FIGURE 1: Diagram of backfill-strip mining.
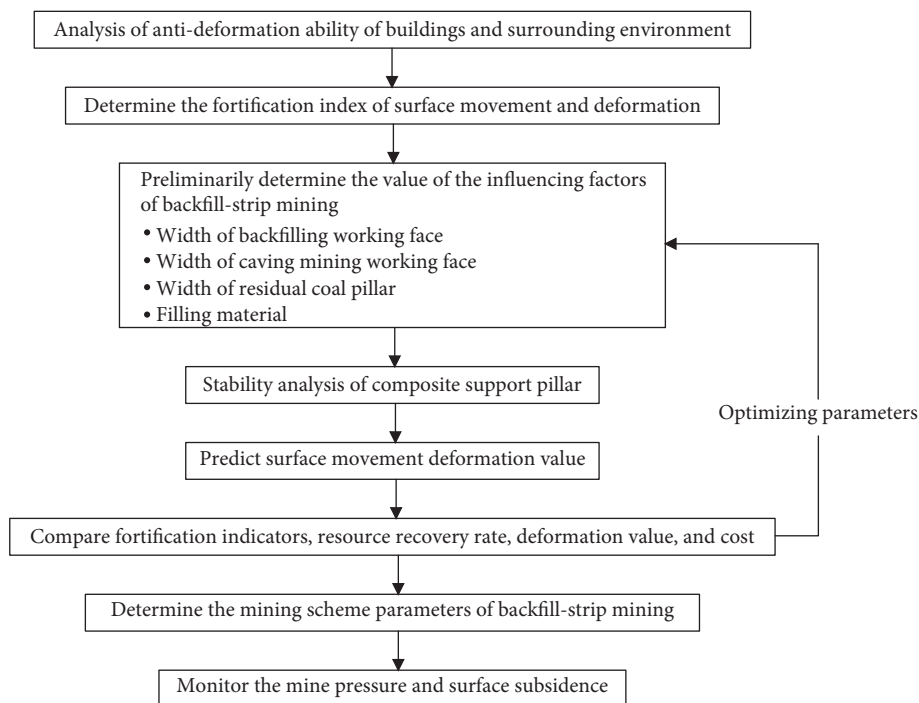
FIGURE 2: Subsidence control design flow of backfill-strip mining.

antideformation ability of buildings and surrounding environment, with determining the mining area of backfill-strip mining with the protection target as the center. The subsidence control fortification index is generally the critical deformation value of the building grade damage, and different environments may require additional fortification indexes. The values of tilt, curvature, horizontal movement, and horizontal deformation are used as the fortification index for the safety of surface building. The maximum surface subsidence is also used as a fortification index to prevent the house from being submerged due to surface subsidence in areas with high phreatic levels.

(2) The influencing factor values of subsidence control in backfill-strip mining are preliminarily determined, and

the influencing factors of subsidence control include the filling material, the size of the backfilling working face, caving mining face, and residual coal pillar.

(3) The type of composite support is determined based on the mining technology and filling material ratio. According to the elastic-plastic analysis of the CSP, the widths of the filling body and residual coal pillar in the different types of CSP are calculated to adjust the width of the backfilling working face, caving mining face, and residual coal pillar. Then, the stability of the CSP is analyzed.

(4) Based on the initial values of working face size, the surface movement deformation value of backfill-strip mining is predicted based on the equivalent superposition PIM.

(5) The values of surface movement and deformation are compared with the fortification index, and the resource recovery rate and economic benefits are analyzed. If the extreme values of surface movement and deformation exceed the fortification index, or the resource recovery rate and economic benefits are inappropriate, then the value of the influencing factors of backfill-strip subsidence control is readjusted and optimized. Step (3) is reconducted until the extreme values of surface movement and deformation are less than the fortification index. Within the fortification index, the resource recovery rate and economic benefits are coordinated, and the backfill-strip mining subsidence process and design parameters are finally determined.

(6) The surface movement and deformation observation station are established according to the backfill-strip mining subsidence technology and design parameters. The regular observations are implemented during the mining impact period for ensuring the safety of surface buildings.

2.3. The Stability Assessment of the CSP. The key to the subsidence control design of backfill-strip mining is to ensure the stability of the CSP and the movement and deformation of the surface structures within the fortification index. These two key steps are affected by the width of the residual coal pillar and working face, so the parameter design of the width of residual coal pillars, the backfilling working face, and the caving mining working face are the core of the subsidence control design of the backfill-strip mining, and the specific calculation method is as follows.

2.3.1. Safety Width Calculation of the Residual Coal Pillar and Backfilling Working Face in Backfill-Strip Mining. The wider the width of the backfilling working face and the residual coal pillars, the lower the coal resource recovery rate and the greater the filling mining cost, which directly affect the stability of the CSP. Therefore, the width of the backfilling working face and the residual coal pillar should be reduced as much as possible under the premise of ensuring the stability of the CSP.

The width of filling working face and coal pillar is also different according to the different filling materials. Zhu [27] divides the stable CSP into three types, namely, Type I, Type II, and Type III CSP, and using the elastic-plastic theory, the calculation method of the minimum residual coal pillar and the width of the backfilling working face under the stable condition of different types of CSP is presented. The residual coal pillars in Type I CSP are wide (Figure 3). The residual coal pillar plays the role of a retaining wall by providing the lateral stress of the filling body to ensure its triaxial stress state and improve the stability of the CSP. The widths of the broken and plastic zones of Type I CSP are small, and its elastic zone, including partial coal pillars and all backfill bodies, is large. The residual coal pillars in Type II CSP are relatively narrow (Figure 4). The widths of the broken and plastic zones of Type II CSP are larger than those of Type I CSP. The residual coal pillars in Type III CSP completely collapse (Figure 5). The filling body is partially destroyed, but the CSP is intact.

The solid filling material of backfilling mining is the bulk material, which needs lateral restraint to obtain a certain supporting capacity. Therefore, when solid backfilling mining is implemented, the stability of the residual coal pillars must be ensured to construct Type I CSP. According to the elastic-plastic analysis method of the CSP, the width of the residual coal pillars on both sides should be at least

$$L_C \geq \frac{n \cdot m}{2 \tan \varphi_0} \left[\ln \left(\frac{k_1 \gamma H + C_0 \cot \varphi_0}{P_x/\beta + C_0 \cot \varphi_0} \right)^{\beta} + \ln \left(\frac{k_2 \gamma H + C_0 \cot \varphi_0}{P_x/\beta + C_0 \cot \varphi_0} \right)^{\beta} + 2 \tan^2 \varphi_0 \right], \tag{1}$$

where L_C is the reserved coal pillar width, m is the average mining thickness of the coal seam, n is the safety factor, taking 1.5, φ_0 is the internal friction angle of the coal seam interface, k_1 and k_2 are the stress concentration coefficients, γ is the average rock mass density, H is the average mining depth of the coal seam, C_0 is the cohesive force of the coal seam, β is the lateral pressure coefficient, p_x is the lateral pressure of the gangue and support on the coal pillar in the caving area, and p_b is the lateral pressure of the backfill on the coal pillar.

The width of the solid backfilling working face should be determined in combination with the predicted results of surface subsidence and the filling process.

Paste filling mining is based on coal gangue as aggregate, mixed with a certain amount of cementing material and water as the filling material. After a period of solidification, the filling material has a certain strength and can be used alone as a support pillar for the overlying strata. Therefore, it can be designed as Type II or Type III CSP when the filling material is paste material, and the coal pillars are completely recovered or a small amount of coal pillars are reserved as the support body to protect the roadway, and the overlying rock strata are supported by the filling body. According to the elastic-plastic analysis of the CSP, the width of the filling face is at least
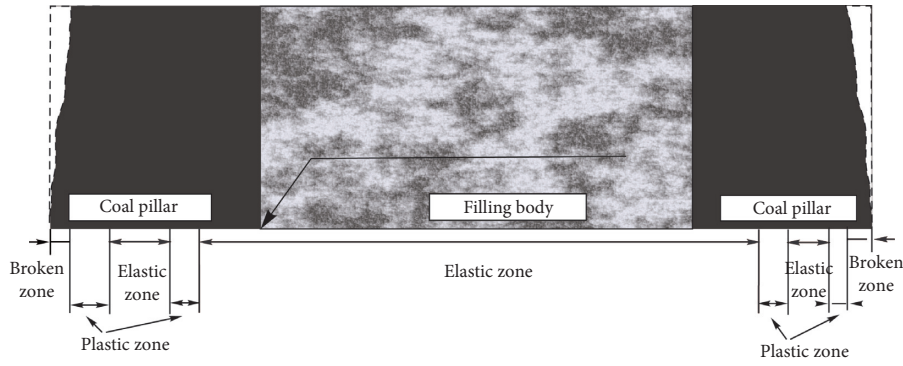
FIGURE 3: Diagram of Type I CSP.
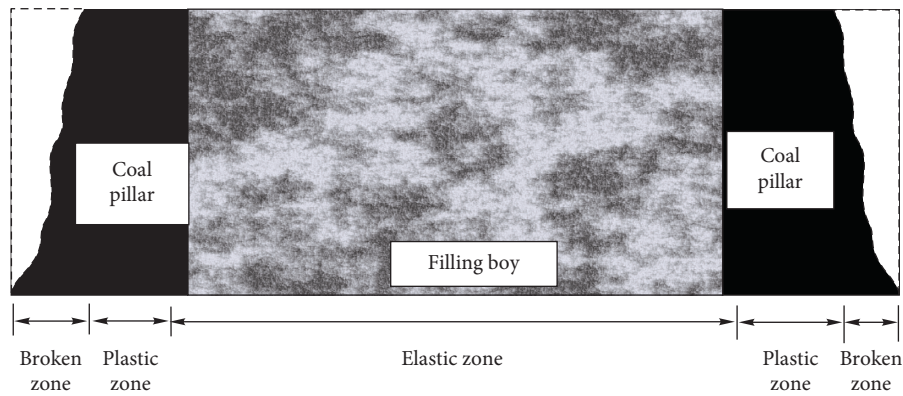
FIGURE 4: Diagram of Type II CSP.
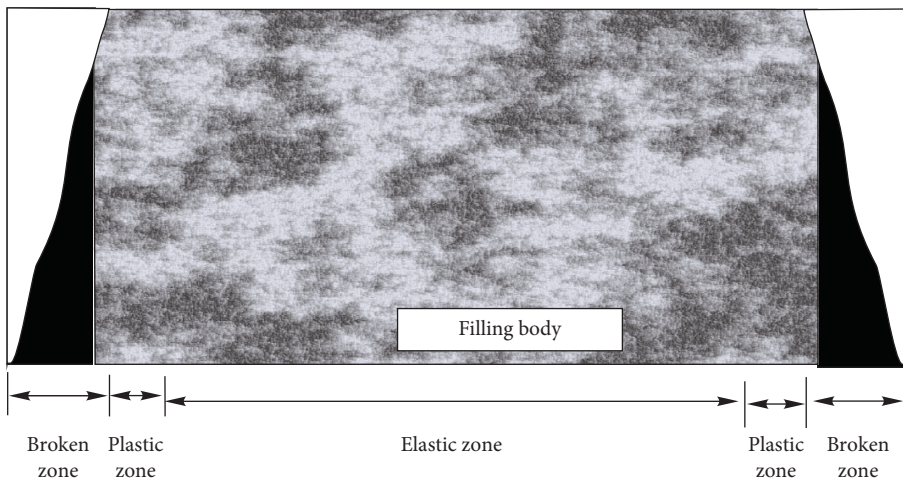
FIGURE 5: Diagram of Type III CSP.

$$L_F \geq n \cdot \frac{k_3 m \gamma H/2 \tan \varphi_0 \left[\ln \left(k_3 \gamma H + C_0 \cot \varphi_0/P_x/\beta + C_0 \cot \varphi_0\right)^\beta + tan^2 \varphi_0\right] + \gamma H \left(2 L_C + L_M\right) - \gamma L_M^2 \cot \delta/4}{k_3 \gamma H - \gamma H}. \quad (2)$$

In the formula, if all coal pillars are recovered, $L_C = 0$, L_F is the width of the filling body, k_3 is the factor of stress concentration, L_M is the width of the caving mining face, and δ is the overburden strata fall angle of the goaf.

2.3.2. Safety Width Calculation of the Caving Mining Working Face. As the size of the caving mining face becomes larger, the coal resource recovery rate will increase and the economic benefits will be better. However, the size of

the caving mining working face has the greatest impact on the subsidence control of backfill-strip mining. Therefore, the width of the caving mining face should be as large as possible under the premise of satisfying the subsidence control requirement.

Consider the following aspects in the design process of caving mining face width:

(a) Referring to the experience of strip mining, the width of the caving mining face should be limited to prevent surface wave subsidence basin, and the ratio of the caving mining working face width to the average mining depth is generally less than 1/3.

(b) From the perspective of insufficient mining, the width of caving mining working face should be limited to the extremely subcritical mining, and the ratio of the width of the caving mining face to the average mining depth is generally less than 1/3.

(c) Finally, the prediction values of surface movement deformation are less than the fortification index. Section 2.4 describes the prediction method of surface subsidence in backfill-strip mining.

2.4. The Surface Subsidence Prediction Method in the Backfill-Strip Mining.
Zhu [20] proposed a detailed prediction method of surface subsidence in the backfill-strip mining. The prediction method of surface subsidence in backfill-strip mining can be adopted as the superposition of the surface subsidence results of strip mining and backfilling mining.

The superposition surface subsidence prediction method for backfill-strip mining is developed on the basis of the PIM (Figure 6). PIM is a mining subsidence prediction method based on stochastic media theory. In China, PIM is the most used function for coal mine subsidence prediction and plays an important role in reducing the influence of mining subsidence. According to the principles of mining subsidence prediction by the PIM, the formula of surface subsidence caused by a small unit is as follows:

$$W_e(x, y) = \frac{1}{r}e^{-\pi\left(x^2 + y^2/r^2\right)}, \tag{3}$$

where $W_e(x, y)$ is surface subsidence caused by a small unit mining, (x, y) are coordinate of the surface point, r is major influence radius given by $r = H/\tan\beta$, H is mining depth, and $\tan\beta$ is tangent of major influence angle.

Integral is carried out on the whole working face, and the subsidence value of any point caused by the mining of working face could be calculated as follows:

$$W(x, y) = \iint\limits_D W_0 W_e(x, y)\mathrm{d}s\mathrm{d}t,$$

$$= \iint\limits_D \frac{W_0}{r^2}e^{-\pi\left((x-s)^2 + (y-t)^2/r^2\right)}\mathrm{d}s\mathrm{d}t, \tag{4}$$

where $W(x, y)$ is the subsidence of working face mining, W_0 is the maximum ground subsidence, $W_0 = mq\cos\alpha$, m is the mining thickness, q is the subsidence factor, α is the dip angle of coal seam, D is the calculation mining area of the working face, the length of the area D along the strike is D_3, l is the calculated length of the working face along the strike and can be calculated by $l = D_3 - 2S$, S is the inflection point offset, the length of the area D along inclination is D_1, L is the calculated length of the working face along the strike and can be calculated by $L = (D_1 - 2S)\sin(\theta + \alpha)/\sin(\theta)$, θ is the main propagation angle, and $ds\,dt$ is the integration variable of double integral of area D.

2.4.1. Surface Subsidence Prediction of the Backfill Mining.
The actual mining thickness of backfilling mining is not the thickness of the coal seam. The traditional caving mining PIM model cannot be applied to backfilling mining. The concept of equivalent mining height is proposed to solve this problem (Figure 7). The equivalent mining height is the difference between the actual mining height of the filling face and the filling height, that is, the mining height of the working face minus the height of the compaction filling.

The calculation formula of the equivalent mining height M_e is as follows:

$$M_e = (M - \delta - \Delta)\eta + \delta + \Delta, \tag{5}$$

where M_e is the equivalent mining height for backfilling mining, δ is the amount of top plate moving, Δ is the unfilled height, and η is the compression rate of the filling body.

The surface subsidence calculation formula for backfilling mining is obtained by substituting the equivalent mining height formulas (5) into (4):

$$W_b(x, y) = [(M - \delta - \Delta)\eta + \delta + \Delta]\frac{q_b \cos\alpha}{r_b^2}\iint_D e^{-\pi\left((x-s)^2 + (y-t)^2/r_b^2\right)}\mathrm{d}t\mathrm{d}s, \tag{6}$$

2.4.2. Surface Subsidence Prediction in Strip Mining.
The mining thickness of strip mining is the mining thickness of the coal seam minus the roof subsidence after the mining is stabilized. The following formula can be used to calculate the thickness M_s of strip mining:

$$M_s = M - M_e,$$
$$= (M - \delta - \Delta)(1 - \eta). \tag{7}$$

Substituting the thickness calculation formula of strip mining into formula (4) yields the calculation formula of the surface subsidence in strip mining:
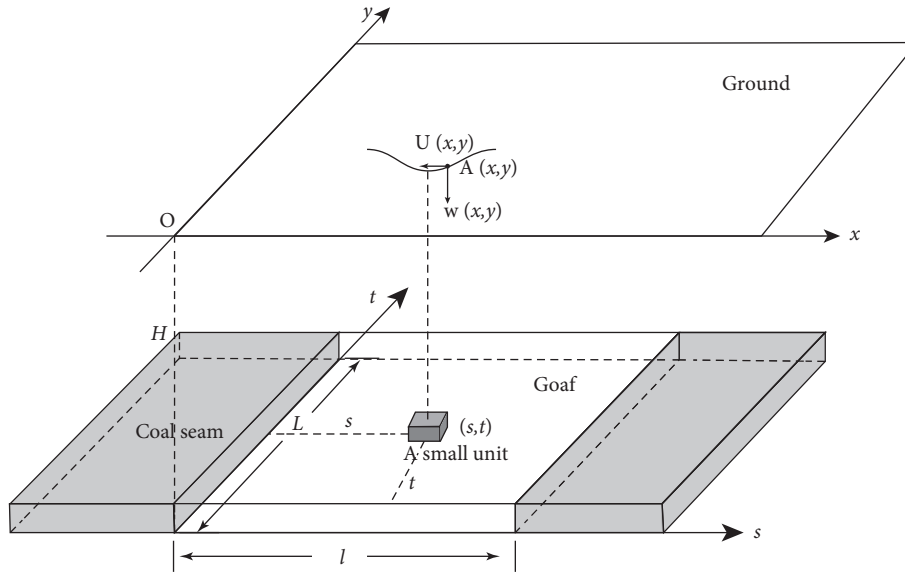
FIGURE 6: A diagram of surfer movement calculated by PIM.
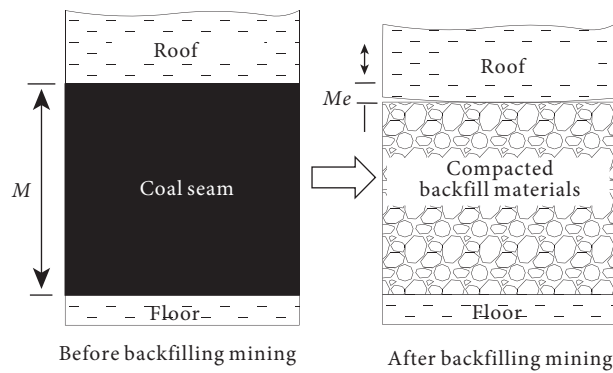
FIGURE 7: Diagram of the equivalent height mining.

$$W_s(x, y) = [(M - \delta - \Delta)(1 - \eta)] \frac{q_s \cos \alpha}{r_s^2}$$
$$\cdot \iint_D e^{-\pi \left((x-s)^2 + (y-t)^2 / r_s^2 \right)} \mathrm{d}t \mathrm{d}s. \tag{8}$$

2.4.3. Surface Subsidence Superposition Prediction of Backfill-Strip Mining.

Surface subsidence of backfill-strip mining can be regarded as the sum of the surface subsidence of backfilling and strip mining. This model is referred to as a superposition prediction method based on the PIM, and its surface subsidence value includes two parts:

$$W = W_b + W_s$$

$$= [(M - \delta - \Delta)\eta + \delta + \Delta] \frac{q_b \cos \alpha}{r_b^2} \iint_D e^{\pi \left((x-s)^2 + (y-t)^2 / r_b^2 \right)} \mathrm{d}t \mathrm{d}s + [(M - \delta - \Delta)(1 - \eta)] \frac{q_s \cos \alpha}{r_s^2} \iint_D e^{-\pi \left((x-s)^2 + (y-t)^2 / r_s^2 \right)} \mathrm{d}t \mathrm{d}s. \tag{9}$$

According to equation (9), the surface movement and deformation values of backfill-strip mining are predicted, and the surface movement and deformation values are compared with the fortification index. If the extreme value of surface movement and deformation exceeds the fortification index, then the values of the influencing factors of subsidence control in backfill-strip mining are readjusted and returned to Step (3) until the extreme value of surface movement and deformation is less than the fortification index; then, the subsidence process and design parameters of backfill-strip mining are finally determined.

3. Engineering Case Study

3.1. Study Area. Ezhuang coal mine is located in Shandong Province, China. The resources of the Ezhuang coal mine are nearly exhausted, and most residual coal reserves are covered by village buildings (Figure 8), which has seriously affected the normal continuity of the mine and shortened the service life. The surface houses in the coal mine are dense. Hence, the caving mining method is not suitable to use for mining because it will easily cause severe surface subsidence, which will have a greater impact on the life of residents. Moreover, the caving mining method is not conducive to the long-term stability and sustainable development of enterprises. Therefore, an effective subsidence control of coal mining technology must be established.

The designed mining area is the 15th coal seam in the west wing of the first mining area. The 15th coal seam in the west wing of the first mining area is located in the middle of the coal mine. The average strike length of the mining area is 750 m, the average incline width is 850 m, and the mining height is 1.2 m. The direct roof of the coal seam is siltstone with a thickness of 8 m.

According to the regulation [20] promulgated by China Coal research institute, the impact of coal mining on the buildings should be less than the Level I damage. The movement deformation values of the building with the Class I damage are as follows: the horizontal deformation, curvature, and tilt value do not exceed 2.0 mm/m, 0.2 mm/m^2, and 3 mm/m. Therefore, the safety fortification index of the surface building are as follows: the horizontal deformation, curvature, and tilt values are 2.0 mm/m, 0.2 mm/m^2, and 3 mm/m, respectively.

3.2. The Width Design of the Residual Coal Pillar and Working Face in the Study Area. Since the backfilling working face adopts the solid filling material as the filling body, the filling body itself has poor supporting ability and needs lateral restraint to obtain a certain supporting capacity and ensure the stability of the residual coal pillars. Type I CSP should be designed to support the load of overlying strata for ensuring the safety of surface buildings and the subsidence control effect of the overlying strata. The designed mining thickness of the 15th coal is 1.2 m, and the factor of stress concentration k_1 is 1.4 and of k_2 is 1.3. The average unit weight γ of the rock formation is 25 kN/m^3, the average mining depth H of the coal seam is 630 m, and the lateral pressure coefficient $\beta = 0.34$. The internal friction angle φ_0 of the coal seam interface is set to 24°, and the cohesive force C_0 of the coal seam interface is set to 2.9 MPa. If the collapsed gangue and anchor rods in the goaf have no binding force on the horizontal direction of the coal wall, then $p_x = 0$. The side pressure of the backfill on the coal pillar is calculated by the passive earth pressure formula; then, $p_b = 37.4$ MPa. The width of the plastic zone at the junction of the coal pillar and the backing body is zero because the side pressure of the backing body on the coal pillar is large. Substituting formulas (1) and (2), the residual coal pillar size can be obtained as follows:

$$L_C \geq 9.94 \, \text{m}. \tag{10}$$

To meet the needs of engineering construction, the width of residual coal pillar L_C is 10 m.

Since the CSP is Type I, the stability of the CSP depends on the residual coal pillar, and the size of the backfilling working face is not limited.

According to the design principle, the ratio of the width of the caving mining working face to the average mining depth should be controlled within 1/3 to prevent the surface from wave subsidence. The average mining depth of the 15th coal seam in the design area is 630 m, so the width of the caving mining working face should be less than 210 m.

3.3. Layout of the Working Surface in the Study Area. The layout of the backfill-strip mining face in the study area is as follows: the working faces of 11501, 11503, and 11505 are filled by solid backfilling method, and the gangue filling rate of the designed goaf is 75%. Then, the working faces of 11502, 11504, and 11506 are mined by caving mining method. The design mining thickness is 1.2 m, the layout plan of the working face is shown in Figure 9, and the sizes of each working face are illustrated in Table 1. The design scheme can mine approximately 531,000 tons of coal.

3.4. Surface Movement and Deformation Prediction in the Study Area

3.4.1. Prediction Parameters of Surface Movement and Deformation

(1) Analysis of the Observation Data of Surface Subsidence. The surface movement and deformation calculation parameters for caving mining in the 15th coal seam are comprehensively determined according to the data of the strata movement analysis and the strata movement parameters of nearby coal mines with similar geological mining conditions. The strata movement calculation parameters of the PIM are shown in Tables 2 and 3 under the conditions of the first mining and repeated mining of the coal seam in the coal mine.

(2) Predicted Parameters of PIM in the Backfill Mining. The geological and mining conditions of Ezhuang coal mine and the solid backfilling mining technology are considered; then, the designed goaf gangue filling rate is 75%, and the equivalent mining height of each backfilling working face is

$$\begin{aligned} M_e &= M - M_g, \\ &= 1200 - 1200 \times 0.75, \\ &= 300 \, \text{mm}. \end{aligned} \tag{11}$$

According to the equivalent mining height theory, the surface subsidence of solid backfilling mining can be predicted by the prediction formulas of caving mining method and the parameters under the same geological mining conditions. The prediction parameters of backfilling mining for the 15th coal seam is approximately equal to the predicted parameters of PIM in the case of repeated mining (Table 4).
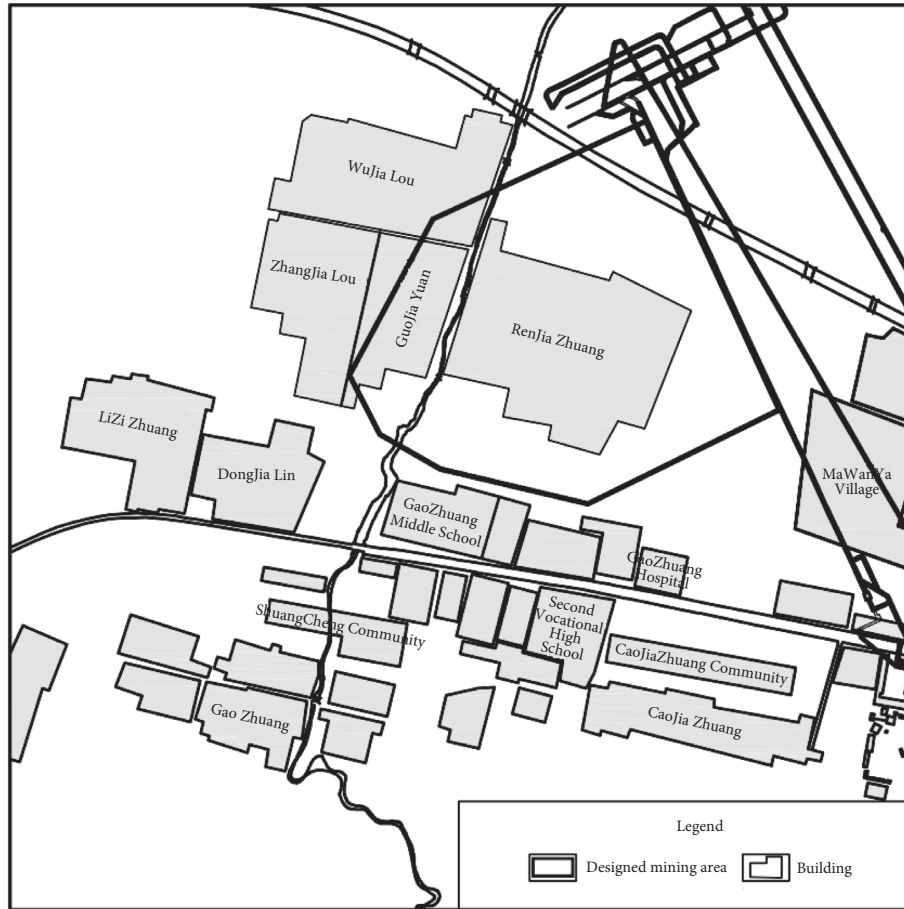
FIGURE 8: Ground and underground contrast map.

(3) Predicted Parameters of PIM in Strip Mining. The number of mining strips in the design area is small, and the superposition prediction method of multiple small working faces can be used to predict the surface subsidence affected by strip mining.

The surface subsidence parameters of PIM for small working face mining are mainly related to the area recovery rate and width-depth ratio of the mining area of the working face and can be obtained according to the conversion relationship with caving mining method. The predicted parameters of the strip mining in the case of the first mining area adopt the PIM of small face mining under the condition of extremely insufficient mining. The predicted parameters of each working face in the study area are determined (Table 5).

The effective thickness of strip mining is as follows:

$$
\begin{aligned}
M_s &= M - M_e, \\
&= 1200 - 300, \\
&= 900 \text{mm}.
\end{aligned}
\tag{12}
$$

(4) Prediction Analysis of Surface Movement and Deformation. The surface movement and deformation of backfill-strip mining should be predicted by the prediction model of the equivalent superposition PIM.

Before the 15th coal seam was mined, the surface buildings had been affected by the 7th coal seam, so the superposition influence of the 7th and 15th coal seam was predicted in the final surface subsidence. Table 6 is a statistical table of the maximum value of surface movement and deformation in the backfill-strip mining in the study area. The surface curvature is less than 0.01 mm/m^2; hence, it is not listed. Figure 10 shows the predicted contour map of the surface subsidence in backfill-strip mining.

Table 6 illustrates that the maximum surface subsidence in backfill-strip mining is 754 mm. The maximum tilt value is 2.9 mm/m, the maximum horizontal movement value is 232 mm, the maximum tensile deformation value is 1.2 mm/m, and the maximum compression deformation value is 1.8 mm/m. The above prediction and analytical results demonstrate that the buildings on the surface are only damaged by level I and can be normally used after backfill-strip mining at each working face. After backfill-strip mining is carried out, the length of the road section affected by mining subsidence of the Tailai Expressway is approximately 944 m. The maximum subsidence of the affected section is 370 mm, the maximum tilt deformation is approximately 2.7 mm/m, the maximum tensile deformation is 1.2 mm/m, the maximum compression deformation is 0.9 mm/m, and the maximum horizontal movement is 210 m.

FIGURE 9: The layout of the backfill-strip mining working face.

TABLE 1: Size of each working surface.

Working face	Strike length (m)	Incline length (m)	Width of the residual coal pillar (m)
11501 backfilling working face	371	80	10
11502 caving mining working face	444/621	99	10
11503 backfilling working face	621/808	103	10
11504 caving mining working face	700/808	118	10
11505 backfilling working face	574/700	96	10
11506 caving mining working face	416/574	100	10

TABLE 2: Predicted parameters of PIM in the case of the first mining.

Mining depth (m)	Q	b	Tan β	θ (°)	S (H)
300–500	0.62	0.3	1.8	85.2	0.08
550–1000	0.58	0.3	1.74		

TABLE 3: Predicted parameters of PIM in the case of repeated mining.

Mining depth (m)	Q	b	Tan β	θ (°)	S (H)
300–500	0.68	0.3	2.4	87	0.06
550–1000	0.60	0.3	2.2		

TABLE 4: Subsidence prediction parameters of backfilling mining.

Prediction parameters	q	b	Tan β	S	θ_0 (°)
	0.60	0.3	2.2	0	$90° - 0.5\alpha$

α is the inclination angle of the coal seam.

TABLE 5: Subsidence predicted parameters of the 15th coal seams' strip mining.

Prediction parameters	q	b	Tan β	S (H)	θ_0 (°)
	0.40	0.28	1.85	0.05	$90° - 0.5\alpha$

TABLE 6: Extremum statistics of surface movement and deformation in backfill-strip mining.

Subsidence (mm)	Tilt deformation (mm/m)		Horizontal movement (mm)		Horizontal deformation (mm/m)	
	North and south	East and west	North and south	East and west	North and south	East and west
754	2.9	2.5	232	184	−1.8, 1.2	−1.3, 1.3
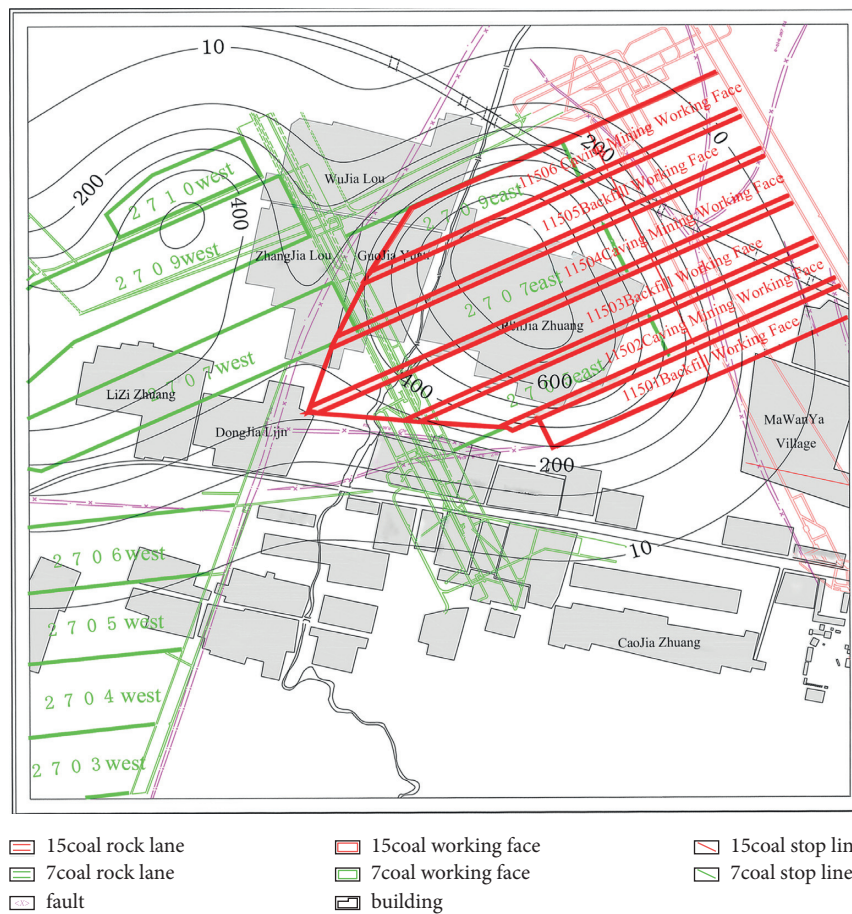
FIGURE 10: Contour map of surface subsidence.

(a)

(b)

(c)
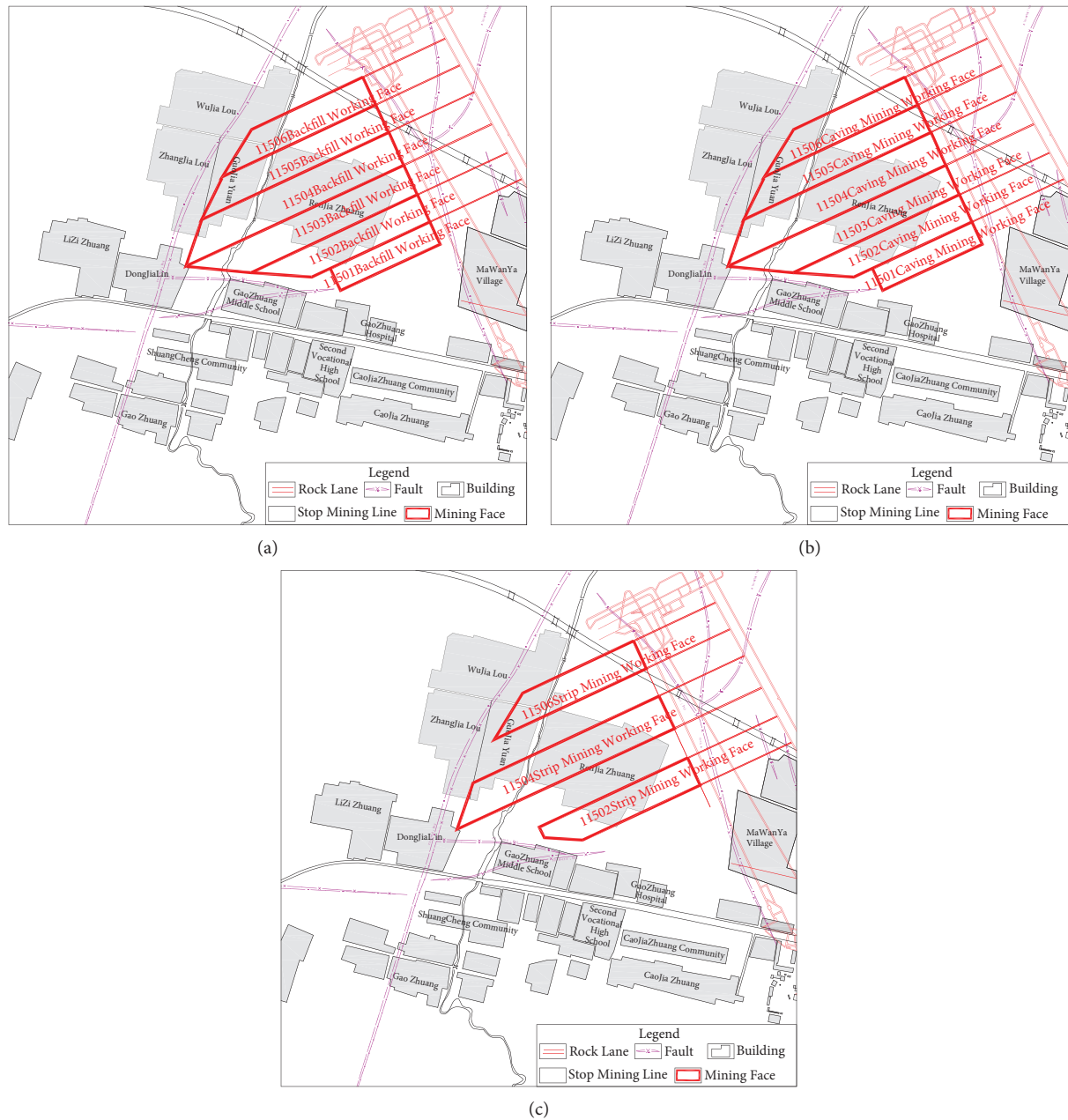
Figure 11: Working face layout of different mining methods. (a) Layout of backfilling mining working face. (b) Layout of caving mining working face. (c) Layout of strip mining working face.

In combination with the predicted results of surface movement and deformation, the selected size of the residual coal pillar and working face meets the fortification index.

4. Comparison of Subsidence Control Effect and Economic Benefit of Different Mining Methods

The surface subsidence values of backfill mining, strip mining, and caving mining methods are predicted by PIM to assess the subsidence control effect. The working face layouts of different mining methods are shown in Figure 11. The maximum values of surface subsidence of each mining method are shown in Table 7. The comparison and analysis of the resource recovery rate, economic benefits, mining technology issues, and social issues are shown in Table 8.

(1) Backfill mining, backfill-strip mining, and strip mining and caving mining are contrasted, and the subsidence control effect and economic benefit are analyzed in this study. The surface movement and deformation values caused by backfill mining, strip mining, and backfill-strip mining methods are small, and the damage to surface buildings is less than level I damage, which does not affect the normal use of the buildings, and only simple maintenance is required. However, the surface movement deformation values

TABLE 7: The extreme values of surface movement and deformation after mining in each scheme.

Mining scheme	Subsidence (mm)	Tilt deformation (mm/m)	Curvature deformation (mm/m^2)	Horizontal movement (mm)	Horizontal deformation (mm/m)
Backfilling mining	653	2.5	0.02	184	−1.8/1.1
Backfill-strip mining	754	2.5	0.03	232	−1.8/1.3
Strip mining	667	2.6	0.02	207	−1.8/1.2
Caving mining	1573	5.3	0.03	450	−2.5/2.3

TABLE 8: Benefit comparison of different coal mining schemes under buildings.

Mining scheme	Damage level of surface buildings	Village treatment scheme	Minable coal volume (10,000 tons)	Filling cost (ten thousand yuan)	Mining technical issues	Social issues
Backfilling mining	Level I damage	Repair compensation	54	2160	Low coal mining efficiency, and high filling costs	The surface subsidence is small, and the buildings are effectively protected.
Backfill-strip mining	Level I damage	Repair compensation	54	1200	High resource recovery rate and low filling costs	The surface subsidence is small, and the buildings are effectively protected.
Strip mining	Level I damage	Repair compensation	23	—	Low resource recovery rate	The surface subsidence is small, and the buildings are effectively protected.
Caving mining	Level II damage	Village relocation	54	—	The mining technology is mature.	The surface subsidence is large, a large number of buildings need to be relocated, the relocation cost is high, and the surface ecological environment has been destroyed.

caused by the caving mining method are large, and the damage to surface buildings exceeds level II damage. A large number of buildings need to be relocated, the relocation cost is high, and the surface ecological environment has been destroyed.

(2) The recoverable coal reserve is 230,000 tons when strip mining is implemented. Meanwhile, the recoverable coal reserve is 540,000 tons when backfill mining, backfill-strip mining, and caving mining methods are implemented, greatly increasing the recovery rate of coal resources.

(3) The backfilling mining and backfill-strip mining adopt backfill mining technology, which increases the filling cost. The added cost of backfilling mining is 21.6 million yuan. Meanwhile, backfill-strip mining belongs to partial filling mining, and the cost has only increased by 12 million yuan. The economic benefit of backfill-strip mining is better than that of backfilling mining.

(4) From the analysis of the surface movement deformation value and economic benefit, it is shown that the surface movement deformation values are small in backfill-strip mining, the surface buildings were not damaged, the resource recovery rate is high, and the filling cost is low. There, the backfill-strip mining can meet the requirements of surface subsidence control and achieve good economic benefits. This backfill-strip mining is the best choice for coal mining under buildings in Ezhuang coal mine.

5. Conclusion

The following conclusions are drawn:

(1) A subsidence control design method of backfill-strip mining was proposed in this paper based on the subsidence control effects and economic benefits. First, the stability of CSP in the backfill-strip mining is analyzed and the values of the main subsidence influencing factors that include the filling material, the size of the backfilling working face, caving mining face, and residual coal pillar are preliminarily determined. Then, the surface movement and deformation are predicted based on the equivalent superposition PIM. The subsidence influencing factors are optimized and determined by comparing the requirements of the safety fortification index of the antideformation ability of surface buildings, resource recovery rate, and coal mining cost. Finally, the mining scheme design parameters of the backfill-strip mining technology are determined.

(2) This method is applied in the subsidence control design of backfill-strip mining in the Ezhuang coal mine. Research results show that backfill-strip mining can ensure the safety of surface buildings, increase the resource recovery rate, and reduce coal mining costs through the reasonable design of this method.

(3) The subsidence control effect and economic benefit of backfill-strip mining, backfilling mining, strip

mining, and caving mining method are contrastively analyzed. Analysis shows that the surface movement deformation values are small in backfill-strip mining, the surface buildings were not damaged, the resource recovery rate is high, and the filling cost is low. There, the backfill-strip mining can meet the requirements of surface subsidence control and achieve good economic benefits.

Data Availability

The data used to support the findings of this study are available from the corresponding author upon request.

Conflicts of Interest

The authors declare that they have no conflicts of interest.

Acknowledgments

References

[1] E. H. Bai, W. B. Guo, H. B Zhang, Y. Tan, and M. J. Guo, "In situ groundwater protection technology based on mining-conservation coordination in the middle and upper reaches of Yellow River Basin," *Journal of China Coal Society*, pp. 1–7, 2021.

[2] B. N. Hu and W. Guo, "Mining subsidence area status, syntheses governance model and governance recommendation," *Coal Mining Technology*, vol. 23, no. 2, pp. 1–4, 2018.

[3] X. Y. Chen and X. M. Shi, "Analysis on the attitudes of coal mine community residents to resource development and influencing factors," *Journal of Natural Resources*, vol. 36, no. 4, pp. 965–977, 2021.

[4] Z. Bian, X. Miao, S. Lei, S. E. Chen, W. Wang, and S. Struthers, "The challenges of reusing mining and mineral-processing wastes," *Science*, vol. 337, no. 6095, pp. 702-703, 2012.

[5] Y. Chen, J. Zhang, A. Zhou, and B. Yin, "Modeling and analysis of mining subsidence disaster chains based on stochastic Petri nets," *Natural Hazards*, vol. 6, no. 1, pp. 1–23, 2018.

[6] Y. F. Duan, Y. X. Zhang, and C. Yu, "Effects of the underground coal mining on the dynamic changes of vegetation in arid desert area," *Acta Ecologica Sinica*, vol. 40, no. 23, pp. 8717–8728, 2020.

[7] H. W. Tian, X. X. Zhang, R. T. Bi, H. F. Zhu, and Q. Xi, "An assessment of the carbon sequestration loss of farmland ecosystems caused by coal mining," *Journal of China Coal Society*, vol. 45, no. 4, pp. 1499–1509, 2020.

[8] L. L. Wan, K. W. Li, R. Na, and J. Yang, "Stress threshold of ecosystem service affected by coal mining in Huaibei City," *China Environmental Science*, vol. 39, no. 10, pp. 4473–4480, 2019.

[9] D. Lamich, M. Marschalko, I. Yilmaz et al., "Subsidence measurements in roads and implementation in land use plan optimization in areas affected by deep coal mining," *Environmental Earth Sciences*, vol. 75, no. 1, pp. 1–11, 2016.

[10] G. L. Guo, W. K. Feng, J. F. Zha, X. Y. Liu, and Q. Wang, "Subsidence control and farmland conservation by solid backfilling mining technology," *Transactions of Nonferrous Metals Society of China*, vol. 21, pp. 665–669, 2011.

[11] J. G. Liu, J. M. Bi, L. T. Zhao, and G. Q. Xie, "Research and application on automatic control of comprehensive mechanized solid back-fill coal mining," *Coal Science and Technology*, vol. 44, no. 1, pp. 149–156, 2016.

[12] J. G. Liu, X. W. Li, and T. He, "Application status and prospect of backfill mining in Chinese coal mines," *Journal of Natural Resources*, vol. 45, no. 1, pp. 141–150, 2020.

[13] J. W. Bai, B. Q. Cui, T. Y. Qi et al., "Fundamental theory for rock strata control of key pillar-side backfilling," *Journal of China Coal Society*, vol. 46, no. 1, pp. 424–438, 2021.

[14] Y. Zhang, S. G. Cao, N. Zhang, and C. Z. Zhao, "The application of short-wall block back fill mining to preserve surface water resources in northwest China," *Journal of Cleaner Production*, vol. 261, 2020.

[15] X. Zhao, A. Fourie, and C. C. Qi, "Mechanics and safety issues in tailing-based backfill: a review," *International Journal of Minerals, Metallurgy and Materials*, vol. 27, no. 9, pp. 1165–1178, 2020.

[16] X. K. Sun, "Research on paste backfilling mining technology of coal mining under buildings, water bodies and railways," *Coal Science and Technology*, vol. 49, no. 1, pp. 218–224, 2021.

[17] S. Ning, W. B. Zhu, X. Y. Yi, and L. L. Wang, "Evolution law of floor fracture zone above a confined aquifer using backfill replacement mining technology," *Geofluids*, vol. 2021, Article ID 8842021, 14 pages, 2021.

[18] B. Y. Jiang, H. G. Ji, L. Fu, S. Gu, T. Zao, and J. Lu, "Research on evaluation index and application of rockburst risk in deep strip mining," *Mining & Minerals*, vol. 2020, Article ID 8824323, 10 pages, 2020.

[19] Y. Z. Luan, Y. Dong, Y. H. Ma, and L. Y. Weng, "Surface and new building deformation analysis of deep well strip mining," *Advances in Materials Science and Engineering*, vol. 2020, Article ID 8727956, 14 pages, 2020.

[20] X. Zhu, G. Guo, H. Liu, and X. Yang, "Surface subsidence prediction method of backfill-strip mining in coal mining," *Bulletin of Engineering Geology and the Environment*, vol. 78, no. 8, pp. 6235–6248, 2019.

[21] H. Li, G. Guo, and S. Zhai, "Mining scheme design for super-high water backfill strip mining under buildings: a Chinese case study," *Environmental Earth Sciences*, vol. 75, no. 12, 2016.

[22] W. M. Sun, P. L. Liu, F. Cui, W. H. Lv, and L. X. Zhao, "Analysis on main control factors of surface subsidence by strip backfill mining with high water material," *Coal Science and Technology*, vol. 41, no. 12, pp. 11–14, 2013.

[23] X. Du, G. Feng, T. Qi, Y. Guo, Y. Zhang, and Z. Wang, "Failure characteristics of large unconfined cemented gangue backfill structure in partial backfill mining," *Construction and Building Materials*, vol. 194, pp. 257–265, 2019.

[24] China National Bureau of Coal Industry, *The Regulation for the Mine Extraction and Coal Pillars Establishment under Buildings, Water Bodies, Railways and Main Laneways*, China Coal Industry Press, Chaoyang, China, 2017.

[25] L. Wang, X. N. Zhang, G. L. Guo, and J. F. Zha, "Quality control system framework for fully mechanized mining,"

Journal of China Coal Society, vol. 38, no. 9, pp. 1568–1575, 2013.

[26] X. J. Zhu, G. L. Guo, Z. Qian, and Q. Fang, "Simulation analysis of strata movement characteristics of backfill-strip mining," *Journal of Mines, Metals and Fuels*, vol. 63, no. 11, pp. 411–418, 2015.

[27] X. J. Zhu, G. L. Guo, H. Liu, X. Peng, and X. Yang, "Research on stability evaluation model of composite support pillar in backfill–strip mining," *Mathematical Problems in Engineering*, vol. 2020, Article ID 3138258, 11 pages, 2020.

Research Article

Pozzolanic Effect on the Hydration Heat of Cements Incorporating Fly Ash, Obsidian, and Slag Additives

Ilker Ustabas [ID],[1] **Sakir Erdogdu,[2] Ihsan Omur,[1] and Erol Yilmaz** [ID][1]

[1]*Department of Civil Engineering, Faculty of Engineering and Architecture, Recep Tayyip Erdogan University, Rize TR53100, Turkey*
[2]*Department of Civil Engineering, Faculty of Engineering, Karadeniz Technical University, Trabzon TR61080, Turkey*

Correspondence should be addressed to Ilker Ustabas; ilker.ustabas@erdogan.edu.tr

Made up of an engineered mix of ordinary Portland cement (OPC) with artificial pozzolans such as trass, fly ash, and slag, the blended cements have been intensely employed within cementitious materials. The main reasons behind this intensive use can be clarified by enhanced workability/strength, the high resistance to chloride/sulfate, reduced permeability/alkali-silica reaction, and a drop in the heat generated by cement's hydration. The use of cementitious blends within concrete not only offers durable products but also cuts climate impact by energy saving and falling CO_2 emissions. This study presents pozzolanic effect on the hydration heat of cements incorporating fly ash, obsidian, and slag additives. The blended cements were manufactured by three different replacement ratios of 20%, 30%, and 50%. The change in the hydration heat of obsidian-, fly ash-, and slag-based cements was observed by several Turkish standards (TS EN 196-8 and TS EN 196-9). Mortars were used for determining the uniaxial strengths of obsidian-, fly ash-, and slag-based cements. The results show that cement's hydration heat decreases as the rate of additives (e.g., obsidian) increases from 20% to 50%. The cement's fineness greatly affects its hydration heat. Increasing the refinement of pozzolanic material to a certain level (30%) leads to an increase in the hydration temperature. After reaching this level, there is no clear relation between the fineness and the replacement rate of pozzolans. As a result, the findings of this work will provide a good understanding of artificial pozzolans on performance and quality of obsidian-, fly ash-, and slag-based cements.

1. Introduction

The cement's hydration is a reaction which exothermically causes a heat output. This resulting heat can damage concrete or large-sized reinforced concrete elements by triggering it to crack if it exceeds certain values in fresh concrete or the temperature difference between two points surpassing certain values. To prevent such damage, some limitations have been introduced in the relevant standards for the quantity of the temperature released in the concrete and cement's hydration heat [1]. According to the TS 13515 standard, the highest temperature in fresh concrete or concrete structural elements with dimensions exceeding 90 cm thickness should not exceed 65°C. The variance between internal and outside temperature of concrete should not exceed 25°C and 20°C for the concretes with and without

reinforcement, respectively [1]. It is recommended to use cements with low-hydration heat in concrete which eliminate or pointedly diminish the risk of being damaged by the hydration heat. As the hydration heat of general-use cements is governed by the rules stated in EN 196-8 (7-day) or EN 196-9 (41-hour) standard, it should not be more than 270 J/g. Therefore, the hydration heat should not exceed 300 J/g in low-hydration-temperature cements [2]. The use of pozzolans is the most commonly used method in the production of low-hydration cement [3]. Pozzolanic additives affect greatly the hydration reactions of cement [4]. Resulting in a decrease in the ratio of clinker and gypsum because of pozzolans added in the blended cements, less heat output occurs in concrete in comparison with ordinary Portland cement. In addition, the encircling of the pozzolan parts around the clinker grains in the cement causes a slowdown

in cement's hydration rate and delays heat output [5, 6]. Pozzolans are widely used in cement making due to decreasing the cement's hydration heat and providing the benefit to concrete properties [7].

The content and fineness of the pozzolans used in the cement affect the speed of cement hydration, the strength gain of the cement, setting start, setting finish, and standard consistency values [8]. Fly ash, among other additives, has a fine structure as it is obtained by filtering the fumes into a thermal power plant chimney and can be used in the cement without being subjected to grinding. However, additives such as clinker, slag, and pozzolans must be ground to certain fineness values by using grinders. The limit values for the cement fineness are generally given according to the amount of material passing through 32-μm, 45-μm, 90-μm, and 200-μm sieves or the Blaine fineness. According to the TS 25 standard, the specific surface value of the natural pozzolan to be used in the cement should be at least $4000 \, cm^2/g \pm 25\%$ [9]. For the refinement of the limestone to be used in the cement, its specific surface should be ground to nearly $5000 \, cm^2/g$. Pozzolan fineness also affects the early and late strength of cement. Saedi et al. [10] detected an increase in the strength values of up to twice in mortars with alkali activation and two different Blaine's fineness values, $2900 \, cm^2/g$ and $4200 \, cm^2/g$ [10]. Khan and Amin [11] indicated that ultrathin volcanic ash- and slag-based mortars raise the strength acquisition of mortars with normal fineness. Khan and Alhozaimy [12] stated that the cements with natural pozzolans ground to 1800, 3400, and $375 \, cm^2/g$ Blaine fineness provide improvements regarding the stability performance. Moghaddam et al. [13] stated that for a given cement, fine fly ashes offer more hydration temperature than coarse ones. Pozzolans are substances causing a drop in cement's hydration rate, a rise in setting start time, and a slowdown in the strength-gaining speed. Otherwise, pozzolans that do not have suitable fineness will raise undesirable situations, such as decreasing the strength-gaining speed and delaying the setting start time in cement. Niu et al. [14] used blast furnace slag in cement by grinding it to ultrathinness so as not to extend the setting start time of the cement. They stated that ultrafine slag tended to decline in the setting start time of the cement and the standard consistency. The fineness of the pozzolan used in the cement with additives also affects the setting time of the cement [15]. In the cements with blast furnace slag and natural pozzolan, a 13.6% strength increase was observed as pozzolan fineness increased from $2800 \, cm^2/g$ to $4200 \, cm^2/g$. As the pozzolan ratio increases, the grain diameters of cement are collected in a narrow gap and the hydration of cement exhibits a decrease in the temperature [16]. Particles with small grains have a larger surface, and when they are exposed to water, they hydrate faster and cause the mortar to gain more mechanical strength. Cement with finer particles also releases more hydration heat [14]. A fast hydration reaction takes place in the cements with high thinness and alkali level values [7]. Baran and Pichniarczyk [17] stated that there is a clear link between concrete's strength and temperature of cement hydration and the cement with high strength has higher hydration heat. Han et al. [18] stated that fly ash slows down the hydration reaction at early stages, falling the temperature of cement hydration. Thongsanitgarn et al. [19] determined the hydration heat of fly ash- and limestone-based cements by isothermal calorimetry. They declared that a rise in limestone powder's fineness increases the hydration temperature of cement. Tydlitát et al. [20] examined zeolite's hydration heat by isothermal calorimetry and determined at what rate the zeolite addition to the cement reduced the hydration heat. As a result, one can say that the hydration heat of pozzolans is a hot topic [21]. Reducing the hydration temperature of cement is crucial, mainly in mass concretes and thick concrete structural elements [22].

Figure 1 shows the cement hydration mechanism which is basically divided into five phases [23, 24]. In stage one, as cement is mixed with water, aluminate reacts with water and rapid heat is released. The reaction of sulfate with water surrounds the cement grains to form ettringite. In stage two, which is the dormant phase of the cement for 2–4 hours and the cement grains of ettringite gel, the cement grains are kept under pressure by wrapping them around. In stage three, after supersaturating Ca-rich pore solution, alite and belite transform into C-S-H and CH gels without dissolving, and it begins to form with major heat evolution. At stage four, the contact of C-S-H and CH products with water and anhydrate particles retards the reaction of alite (i.e., the basic phase required for setting/increasing early strength gains), thus reducing the hydration heat of cement. Sulfate's quantity begins to decline, and aluminate responds with ettringite (Ca-Al-SO_4^{2-}) to construct monosulfate, which may lead to low temperature. Figure 1 shows three temperature peak values occurring after the hydration stages of cement [23].

Two main techniques are employed for appreciating the temperature of cement hydration: (i) the chemical technique and (ii) the semiadiabatic technique. TS EN 196-8 is a chemical technique in which cement's hydration heat is determined by calculating the temperature released by dissolving cement in acid in a calorimeter. When determining the hydration temperature according to TS EN 196-8, the heat flow diagram is a reverse arc curve that first rises and then descends, and it does not conform to the curve in Figure 1. In the ASTM C1679 standard method, with the help of isothermal calorimetry, the hydration heat of cement is evaluated by the temperature released by the reaction with the cement. In this way, it partly resembles the shape in Figure 1, regarding determination of hydration temperature. TS EN 196-9 is a semiadiabatic technique in which cement hydration temperature is determined by the temperature released from the mortar sample consisting of a cement, water, and sand mixture. Since the mortar mixture is prepared outside and placed inside the calorimeter, the sudden temperature rises in Stage I cannot be detected clearly in this method.

This work inspects the hydration temperatures of fly ash-, slag- and obsidian-based cements, using the TS EN 196-8 and TS EN 196-9 methods. How obsidian affects the hydration heat of cement, in comparison with cement containing fly ash and slag additives, was measured. How pozzolan fineness affects the hydration heat of cement was
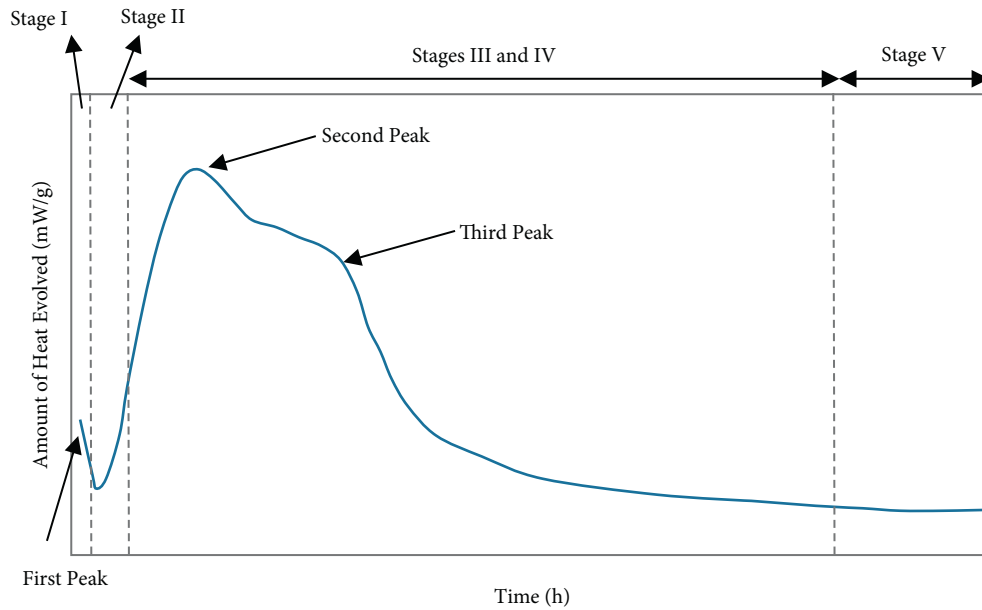
FIGURE 1: Schematic view of the hydration stages of cement (modified after [23]).

investigated. Although the hydration temperatures related to cement incorporating fly ash and slag additives exist in the literature, there is no work being conducted on the hydration heat values of obsidian (a.k.a., volcanic glass), which provides the originality of the present work. Additionally, in the hydration heat measurements made according to TS EN 196-8 and TS EN 196-9, this study indicates clearly that the temperature difference value of cements incorporating fly ash, obsidian, and slag additives decreases as the mineral additive ratio increases. Additionally, mineral additives are found to decrease the hydration heat of cement.

2. Materials and Methods

2.1. Materials. The cement used in this study is typically produced by adding 20%, 30%, and 50% fly ash, slag, and ground obsidian to CEM I 42.5R. Three different fineness levels of fly ash, slag, and obsidian additives were added to CEM I 42.5R. Table 1 lists the different fineness levels of 10 different cement types. Table 2 lists cement's chemical composition and the reactive silica contents of pozzolans.

The fly ash utilized during the experiments was sampled from the Tuncbilek thermal power plant in the province of Kutahya (Turkey), while the slag additive was sampled from the Karabuk iron and steel plant. Obsidian, also known as volcanic glass, is a rare substance used as a pozzolan in cement in the literature. In the region in which this study was carried out, there is lots of obsidian in the area of 10 km^2 (Figure 2).

Figure 3 shows obsidian located in the Rize-Ikizdere locality which is in sharp glass form. Obsidian having a thick and massive appearance is spread over a wide area, reaching up to six meters thick. The obsidian structure is sharp and like broken glass, which is dangerous for humans/animals to wander in this area. The obsidian used as a pozzolan in this study was pulverized and added to cement [8].

2.2. The Fineness of the Cements Used. The fly ash and slag additives were ground to different fineness levels in a ball mill. Obsidian was crushed by using a jaw crusher at laboratory first and then ground by using a ball mill. Table 1 lists the cement fineness. Obsidian was ground in 45, 60, and 75 minutes and fly ash and slag in 20 and 40 minutes to obtain the targeted pozzolan fineness levels within the scope of the study.

2.3. Determination of Hydration Heat of Cement. The solution and semiadiabatic methods are used to study the hydration heat of cement. The hydration heat of additive-based cements (e.g., obsidian, fly ash, and slag) with three fineness levels and cement without pozzolan was measured by using two different Turkish standard methods (i.e., TS EN 198-8 and TS EN 196-9).

The determination of the hydration heat of cement, based on TS EN 196-8 standard procedure, is calculated by dissolving the cement and hydrated cement in the solution made by adding 2.76 g of 40% hydrofluoric acid solution to each 100 g of nitric acid solution of 2 ± 0.01 mol/liter. The mass ratio of total acid/dry cement mixtures is 140 ± 2 g of the dry cement dissolved in the acid solution. The solution's temperature escalation is measured with a thermometer with 0.002°C precision.

After 7-day hardened cement prepared by adding 100 g of cement to 40 g of water is crushed and sieved, the temperature released by its dissolution in acid in hydrated cement, which is 40% more than the mass of dry cement, is measured. The hydration heat of the cement is calculated using the following equation from the temperature differences obtained:

$$H_i = Q_a - Q_i, \tag{1}$$

where Q_a shows the melting temperature of dry cement in solution. Q_a is calculated by the following equation:

TABLE 1: Fineness values of cements containing different pozzolanic additives.

Cements with different additives	Percentage left on sieve			Blaine fineness (cm^2/g)
	$200\,\mu m$	$90\,\mu m$	$45\,\mu m$	
Obsidian (OBS) 45	0	5.3	40.2	4752
OBS 60	0	2.5	35.3	5502
OBS 75	0	1.7	28.5	6135
Fly ash (FA)	0	0	11.7	4263
FA 20	0	0	7.5	5261
FA 40	0	0	6.8	6705
Blast furnace slag (BFS)	0	0	9.8	4713
BFS 20	0	0	7.5	5623
BFS 40	0	0	6.9	6125
CEM I 42.5R	0	0	19.5	4424

TABLE 2: A summary of oxide analysis of additives utilized in the experiments (%).

Oxides	CEM I 42.5R	Obsidian	Fly ash	Blast furnace slag
CaO	63.52	0.75	3.85	31.23
SiO_2	18.48	71.56	51.65	37.58
Al_2O_3	5.25	12.52	17.65	10.52
Fe_2O_3	3.48	1.53	11.51	0.63
MgO	1.01	0.17	4.62	8.06
K_2O	1.13	5.21	2.05	1.53
Na_2O	0.36	3.95	0.65	0.35
P_2O_5	0.071	0.011	0.112	0.002
SO_3	2.775	0.003	1.25	3.57
TiO_2	0.13	0.17	0.68	0.41
Sr	0.075	0.012	0.013	0.061
Cr_2O_3	0.06	0.065	0.11	0.13
MnO	0.25	0.05	0.12	1.25
Loss on ignition	2.76	2.02	2.13	1.12
Reactive silica	-	39.34	47.13	43.01

$$Q_a = \left(\frac{C \cdot \Delta T_c}{P}\right) + 0.8\left(T_f - T_a\right) + 0.8\left(T_f - 20\right)\left(\frac{J}{g}\right). \quad (2)$$

ΔT_c is the modified temperature increase, Kelvin (K) is the calorimeter's thermal capacity (J/K), P is the dry cement's amount (g), T_f is the dry cement's temperature at the end of the dissolution period (°C), and T_a is the environment in which the dry cement was added to the calorimeter. The temperature (°C), 0.8, is the dry cement's heat (J/g K), and −0.8 is the temperature coefficient of the melting heat of dry cement (J/g K).

$$\Delta T_c \text{ for all cements: } \Delta T_c = \left(T_{30} - T_0\right) - 2\left(\left(T_0 - T_{-15}\right) - K\left(T_{30} - T_0\right)\right), \quad (3)$$

$$\Delta T_c \text{ for all cements: } \Delta T_c = \left(T_{30} - T_0\right) - 2\left(T_{45} - T_{30}\right). \quad (4)$$

ΔT_c is calculated from the above equations. The numbers shown as indices under T in the above equations show the temperatures taken from thermometer at a specific time. Q_i indicates the melting temperature of the hydrated cement in the solution. Q_i is determined by the following equation:

$$Q_i = \left(\frac{C \cdot \Delta T_c}{P \cdot F}\right) + 1.7\left(T_f - T_a\right) + 1.3\left(T_f - 20\right)\left(\frac{J}{g}\right), \quad (5)$$

where P is the hydrated cement's amount (g), T_f is the hydrated cement's temperature at the end of the dissolution age (°C), T_a is the ambient temperature (°C) when the hydrate cement is added to the calorimeter, F is the modified bound water factor, 1.7 is the hydrated cement's specific heat (J/gK^{-1}), and −1.3 is the temperature coefficient of the melting heat of the hydrated cement (J/gK^{-1}). The correction factor (F) for bound water is calculated by the following equation:

$$F = \frac{\left(100 - m_h\right)}{\left(100 - m_a\right)}, \quad (6)$$

where m_h indicates the mass change (%) of the hydrated sample afterglow and m_a is the mass change (%) of the dry sample afterglow.

The hydration temperatures of cements incorporating additives such as obsidian, fly ash, and slag were measured according to TS EN 196-8 by using the calorimeter (Figure 4).

TS EN 196-9 is another technique in which the hydration heat of cement is calculated by using the semiadiabatic technique. The test sample is manufactured by blending
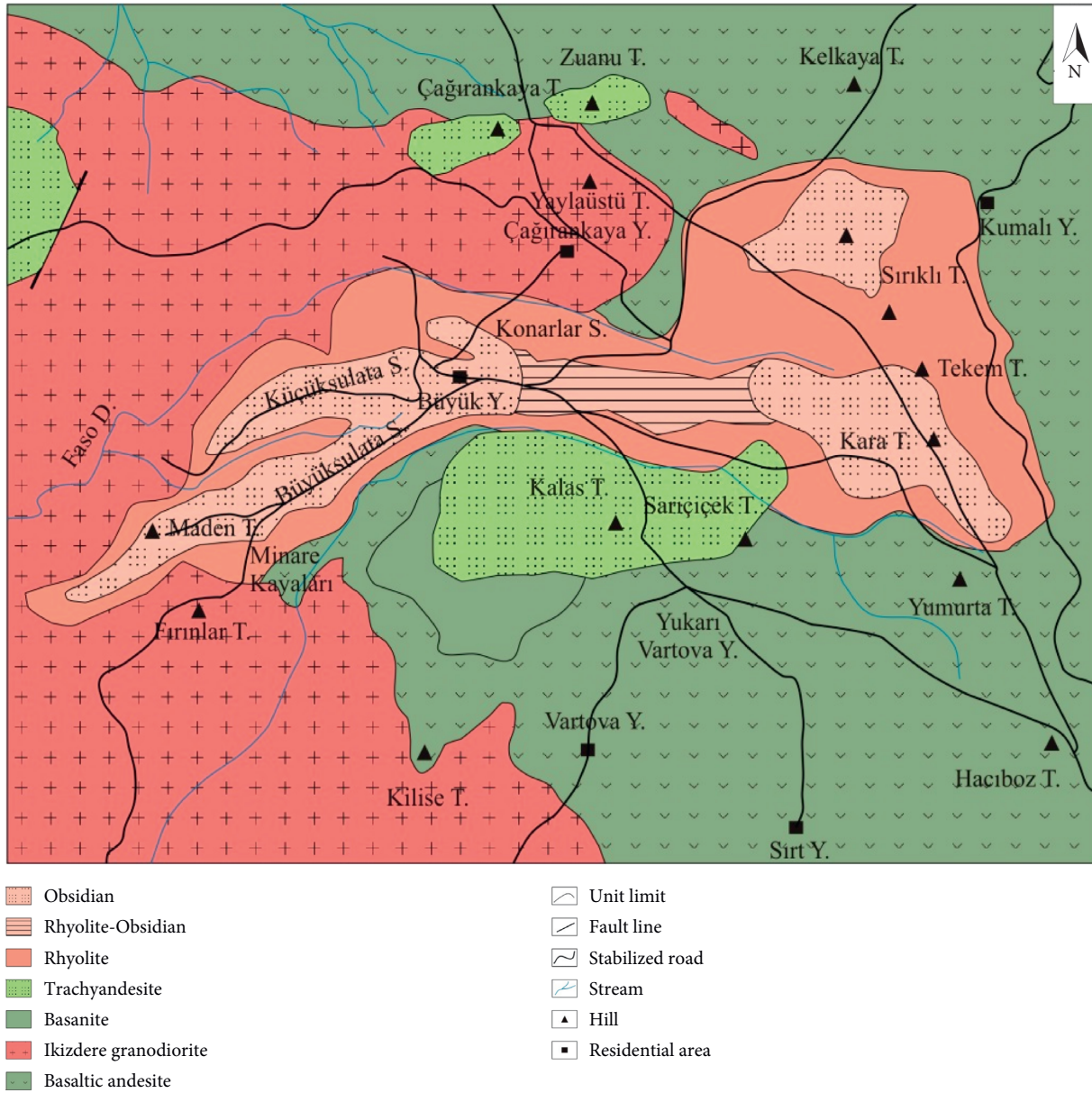
Figure 2: The geological map of Rize Buyukyayla obsidians and their immediate surroundings.

Figure 3: Photo of the obsidian accumulated in rash form.

FIGURE 4: Photo of the calorimeter used by the chemical technique.

360 g of cement and 180 g of water and sand, as given clearly in TS EN 196-9 standard. The total material amount is 1575 g, and hydration heat of cement is measured on two main specimens by using a calorimeter: one is the reference while the other is the measurement of specimen. At temperature readings, the temperature rise of sample (θ_t) is mainly calculated from the temperature differences between T_s and T_r specimens through the calorimeter. The hydration heat ($\square$) of cement is determined by the following equation:where m_c is the cement's quantity (g), t is the interval of cement hydration (h), c is the thermal capacity of calorimeter (J.K^{-1}), and α is the coefficient of temperature losses of the calorimeter (J.h^{-1}.K^{-1}).

$$Q = \frac{c}{m_c}\theta_t + \frac{1}{m_c}\sum_{i=1}^{i=1}\overline{\alpha_i}\cdot\overline{\theta_i}\cdot\Delta t_i, \qquad (7)$$

Figure 5 shows the hydration heat measurement of cements incorporating additives such as obsidians, fly ashes, and slags, as given clearly by TS EN 196-9 standard. The measurement of hydration temperature in the desired time was performed at laboratory, and it found to be 20°C by using a device.

3. Results and Discussion

3.1. Influence of Grinding Time on Temperature Difference of Obsidian-Incorporated Cements. Figure 6 shows the temperature differences measured by subtracting the temperatures measured in CEM I 42.5R and in cement prepared by adding 20%, 30%, and 50% obsidian ground for 45 min from the temperatures measured in the reference mortars. The highest temperature difference of 21.6°C was found in the 26th hour of CEM I 42.5R cement without pozzolan. Erdogan and Kocak [21] calculated the heat flow and hydration heat in 27 types of cement according to the ASTM C1679 standard. Since less cement is used in the ASTM C1679 standard in comparison with the TS EN 196-9 standard, the highest heat flow in ordinary Portland cement reaches nearly 9 hours, and the heat flow decreases to the test starting temperature at 42 hours [21]. The technique used

FIGURE 5: The measurement of computer-controlled hydration temperature in the blended cement.
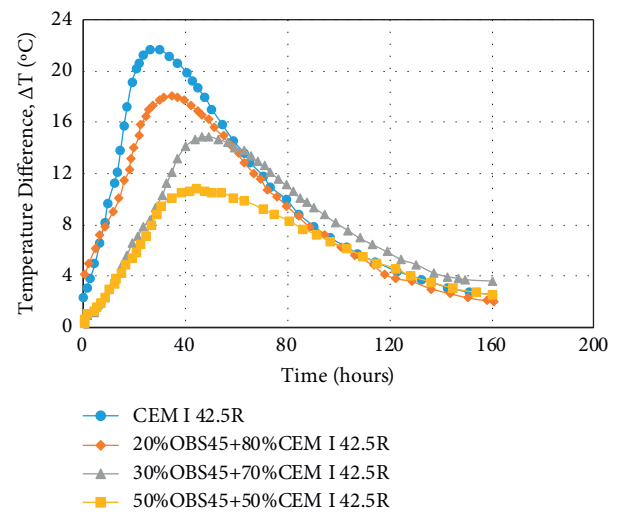

FIGURE 6: Temperature difference of CEM I 42.5R and 45-min ground 20%, 30%, and 50% obsidian-added cements.

affects greatly the highest heat flow and heat flow exit time of the cement.

Figure 6 also shows that, in 20% obsidian-added cement ground for 45 min, the highest temperature is 18.03°C at the 34th hour; in the 30% obsidian-added cement ground for 45 min, it is 14.88°C at the 49th hour; and in the 50% obsidian-added cement ground for 45 min, it is 10.82°C at the 44th hour. The highest temperature difference was found. This means that increasing the rate of obsidian added to cement reduces the maximum temperature differences of cement and extends the time required to reach the highest temperature difference. This shows that the pozzolan surrounds the cement grains, causing the heat output to be slower. Han et al. [18] and Erdogan and Kocak [21] measured the heat flow and hydration temperatures in the cement in which 3.5 g of cement was blended with 1.4 g of water, based on the ASTM C1679 standard. They encountered three temperature increase peaks when the heat flow reached the highest value between 6 and 10 hours. Since the amount of cement used in the TS EN 196-9 method in this study is more than that used in the ASTM C1679 standard and a blend of sand and mortar is made and placed in the

container, the temperature during the initial mixing of water and cement cannot be measured. In the ASTM C1679 method, a temperature peak value is seen in the TS EN 196-9 method, just like the second temperature peak value. The heat leaving the cement reaches its peak value in a longer time and at a higher amount. Adding obsidian ground for 45 min to CEM I 42.5R reduces the resulting temperature and extends the time to reach the highest value.

Figure 7 shows that, as the obsidian addition rate increases in 20%, 30%, and 50% obsidian-added cements ground for 60 min, the time to reach the highest temperature difference of the obsidian cement compared to Portland cement increases and the temperature difference drops. The highest temperature difference is 18.7286°C at 28 hours in cements with 20% obsidian added, ground for 60 min; 16.6996°C at 28 hours in 30% obsidian-added cement, the highest temperature difference per hour; and 15.7689°C at 36 hours for 50% obsidian-added cements. The highest temperature difference is 12.8704°C per hour for milling for 60 min; obsidian-added cement with Blaine fineness of 5497 cm^2/g was ground for 45 min and reached the highest temperature difference in a shorter time compared to cement with a Blaine fineness of 4746 cm^2/g. Increasing the milling time from 45 to 60 min led to a temperature difference by 3.8% in 20% obsidian-added cement, 12.2% in 30% obsidian-added cement, and 19% in 50% obsidian-added cement. Addition of finer obsidian to the cement reduced the time during which the highest temperature difference occurred and increased the temperature difference.

Figure 8 shows the temperature differences of 20%, 30%, and 50% obsidian-added cements ground for 75 min and cement without additives. The temperature differences in obsidian-added cement ground for 75 min are 19.2034°C at 27 hours in the 20% obsidian-added cement, 17.8642°C at 28 hours in the 30% obsidian-added cement, and 12.8515°C at 32 hours in the 50% obsidian-added cement. There was a decrease/increase in temperature difference in obsidian-added cement whose Blaine fineness increased to 6122 cm^2/g by grinding for 75 min, when the peak temperature difference was observed compared to 45- and 60-min ground obsidian-added cements. In obsidian-added cements, as the amount of obsidian increased, the temperature difference value decreased; as the fineness of the obsidian decreased, the temperature difference peak and the temperature difference value increased. This is due to the increase in the speed of the pozzolan entering into reactions as a result of the increase in the fineness of the pozzolan. The issues identified in this study were determined by Binici et al. [16] and Ardoga et al. [4]. Accordingly, as the amount of pozzolan increased, the hydration heat of cement decreased, and when the fineness of cement increased, the reaction rates were determined.

3.2. Effect of Grinding Time on Hydration Heat of Obsidian-Incorporated Cements.
Figure 9 shows the hydration temperatures of 20%, 30%, and 50% obsidian-added cements ground for 45 min and the temperature differences until the 160th hour. The cement hydration heat at the 41st hour was
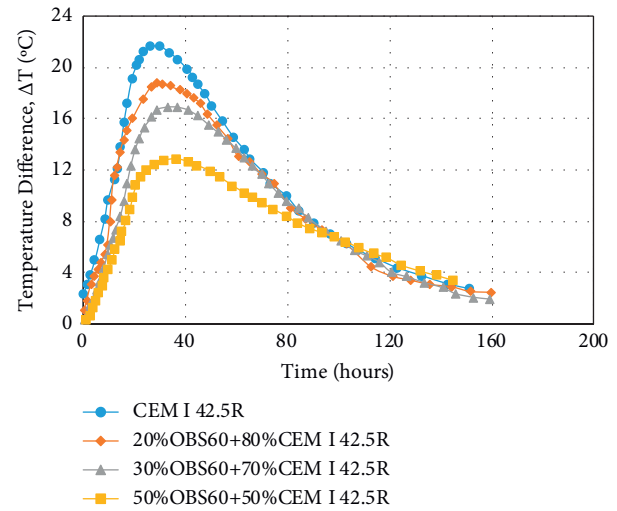

FIGURE 7: Temperature difference of CEM I 42.5R and 60-min ground 20%, 30%, and 50% obsidian-added cements.
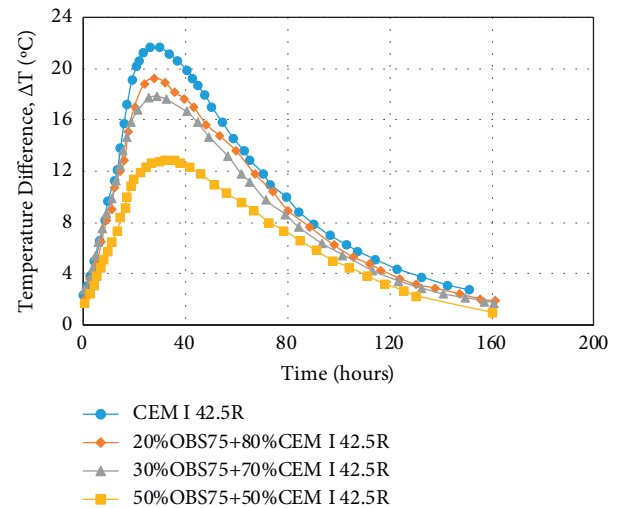
FIGURE 8: Temperature difference of CEM I 42.5R and 75-min ground 20%, 30%, and 50% obsidian-added cements.

267.2 J/g, and the hydration heat at the 160th hour was 362.9 J/g. The hydration temperature at the 41st hour was 130.2 J/g in the 20% obsidian-added cement milled for 45 min. The hydration heat at the 160th hour was 326.9 J/g; the hydration temperature at the 41st hour in the 30% obsidian-added cement was 149 J/g.

The hydration heat at the 160th hour was 278.9 J/g, the hydration heat at the 41st hour was 120 J/g, and the heat at the 160th hour was 233.7 J/g in the 50% obsidian-added cement ground for 45 min. Based on the measurement according to TS EN 196-9, as the rate of obsidian added to cement increased, hydration temperatures decreased.

Figure 10 shows the hydration temperatures of 20%, 30%, and 50% obsidian-added cements ground for 60 min and the cements without additives, measured according to the TS EN 196-9 standard. The addition of obsidian reduced

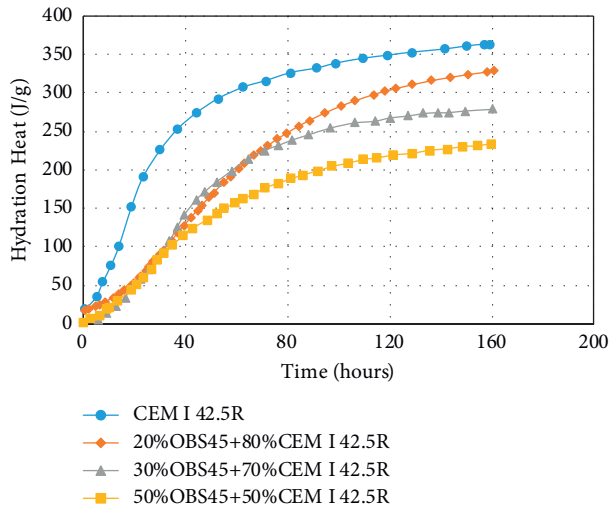FIGURE 9: Measured hydration temperatures in CEM I 42.5R and 45-min ground 20%, 30%, and 50% obsidian-added cements.
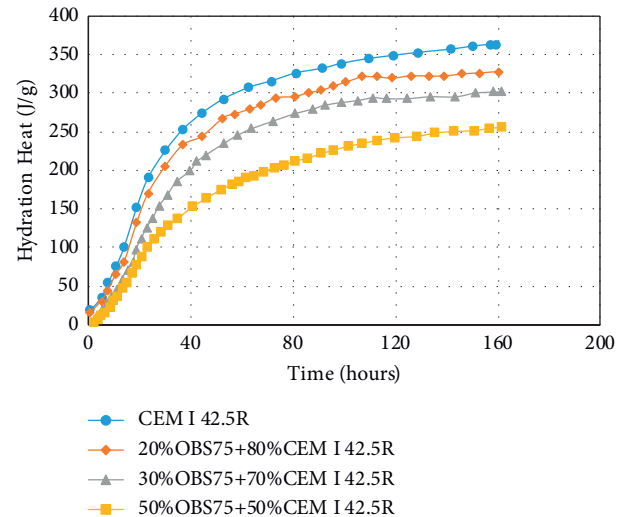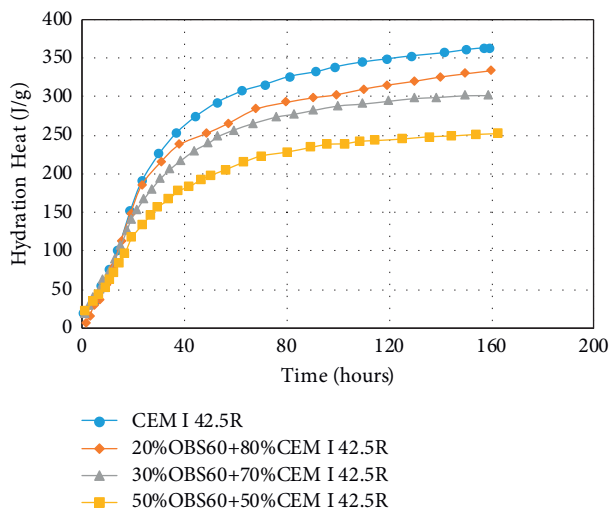

FIGURE 10: Measured hydration temperatures in CEM I 42.5R and 60-min ground 20%, 30%, and 50% obsidian-added cements.

the hydration heat of cement. As the fineness of the pozzolan added to the cement increased, the hydration heat of the obsidian-based cement increased when compared with the cement containing less obsidian added.

Figure 11 shows the hydration heat measured in 20%, 30%, and 50% obsidian-added cements ground for 75 min. As the obsidian rate increased, the hydration heat of cement decreased. Thongsanitgarn et al. [19] indicated that the hydration heat augmented with growing fineness. The findings of this study were consistent with those of Thongsanitgarn et al. [19]. Since the cement has a heterogeneous composition, some hydration temperatures behave differently from this rule. In general, the rise in the amount of obsidian additives caused a drop in the hydration heat, and an increase in obsidian fineness caused a rise in the hydration heat in a short time.

FIGURE 11: Measured hydration temperatures in CEM I 42.5R and 75-min ground 20%, 30%, and 50% obsidian-added cements.

3.3. Effect of Grinding Time on Hydration Heat of Slag-Incorporated Cements. Figure 12 shows the hydration temperatures calculated at the 41st and 160th hours in accordance with TS EN 196-9 for the unadulterated cement and blast furnace slag-added cements.

Figures 9–11 state that the hydration temperature decreased as the pozzolan ratio increased, and a rise in the hydration heat as the fineness augmented was not seen in the blast furnace slag-added cements. Although the hydration temperature decreased as the pozzolan additive ratio increased in the slag-added cements, no major change was detected in the hydration heat when the fineness of cements increased. This shows that when the pozzolan fineness reaches to a certain value, the increase in the fineness of the pozzolan does not increase significantly the hydration temperature.

3.4. Influence of Milling Time on Hydration Heat of Fly Ash-Incorporated Cements. Figure 13 shows the hydration temperatures calculated at the 41st and 160th hours according to TS EN 196-9 for OPC and OPC with fly ash additive. The fly ash added to the cement reduces hydration temperature of cement. Augmenting the fly ash's fineness did not cause a major rise in the hydration temperatures at the 41st and 160th hours. According to Han et al. [18], the cement hydration heat was 200 J/g at the 41st hour when 30% high blast furnace slag was added to the cement. On the other hand, the hydration heat was 175 J/g when slag was added and 125 J/g for 35% cement. It was measured as 150 J/g when fly ash was added and 85 J/g when 65% fly ash was added [18]. The hydration temperatures of the cement replaced with blast furnace slag and fly ash additives, as investigated by Han et al. [18], were similar to those in this study. Demir et al. [25] showed experimentally that the fineness of pozzolanic material greatly affects hydration temperature when measured according to TS EN 196-9.
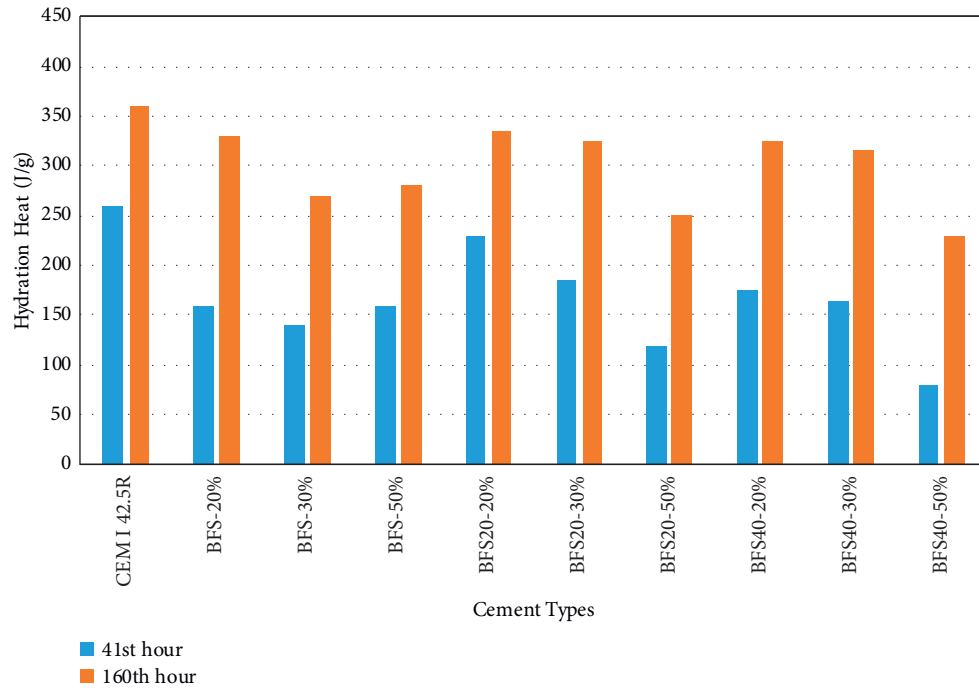
Figure 12: Hydration temperatures at 41st and 160th hours in CEM I 42.5R and 20%, 30%, and 50% slag-added cements.
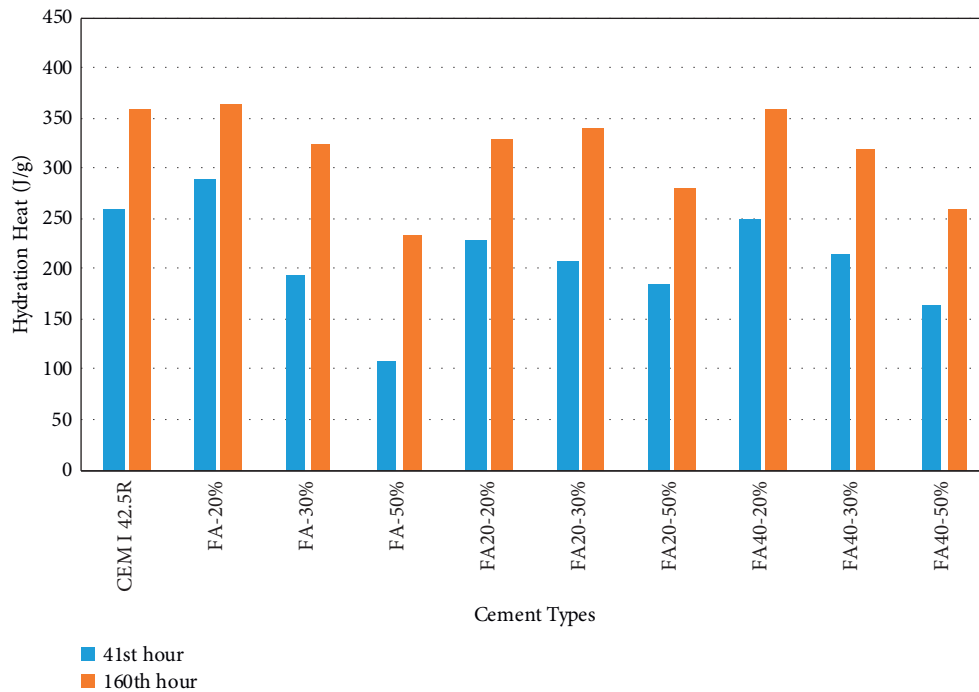
Figure 13: Hydration temperatures at the 41st and 160th hours in CEM I 42.5R and 20%, 30%, and 50% fly ash cement.

3.5. Effect of Additive Type on Hydration Heat of Blended Cements.

Figure 14 shows hydration heat measurements made using the chemical technique, based on TS EN 196-8. Since the influence of additive fineness on the hydration heat of cement, as said by TS EN 196-8, was not determined in this study, the hydration temperatures of additive-containing cements are given in Figure 14. The

hydration temperatures measured based on TS EN 196-8 are compatible with the values at the 41st hour based on TS EN 196-9. Han et al. [18] calculated the cement's hydration heat in 80 hours as 300 J/g; it was 285 J/g in 30% slag contained cement and 180 J/g in 35% fly ash-contained cement [18]. Baran and Pichniarczyk [17] found values ranging from 374 to 404 J/g in CEM I 42.5R. The
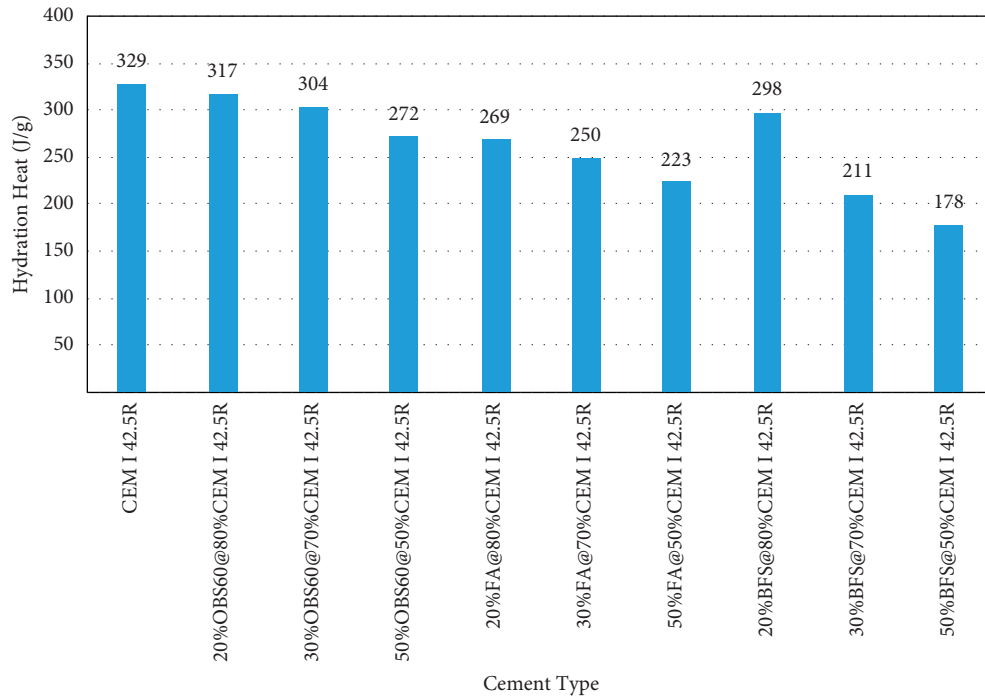
FIGURE 14: Variation of the hydration temperatures measured in the cement.
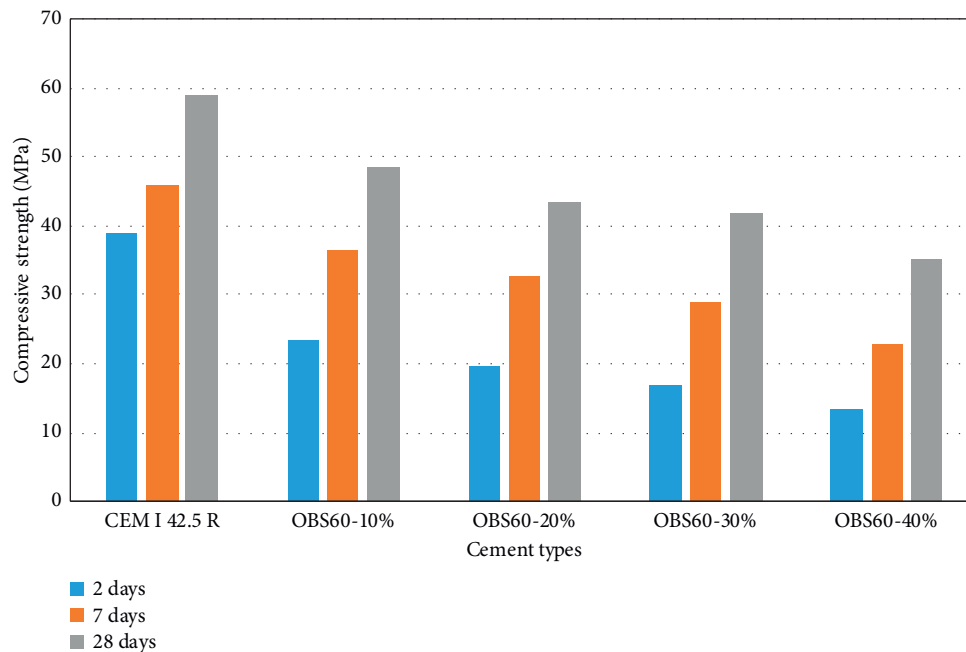
FIGURE 15: Mechanical strength of CEM I 42.5R and mortars produced with 60-min ground 10%, 20%, 30%, and 40% obsidian-added cement.

hydration heat of cement was similar to that in the work done by Baran and Pichniarczyk [17]. Merzouki et al. [26] stated that slag's hydration heat falls after 140 h. Adding an additive content of 20% to cement did not specify a major variation in the hydration heat of obsidian-, fly ash-, and slag-incorporated cements. The hydration heat is strongly affected by the replacement rate of pozzolans and the hydration period.

As the quantity of additives in the mixture rises, the postponement of hydration could set a major drop in the heat of hydration. Cement's hydration heat replaced with 20% obsidian was akin to that of cements replaced with fly ash and slag additives. The hydration heat was determined using the chemical technique according to TS EN 196-8 to compare the results with those of the tests done according to TS EN 196-9. The determination of hydration heat on 7-day

FIGURE 16: Compressive strengths obtained from CEM I 42.5R cement and cements replaced with obsidian, fly ash, and slag (with a replacement rate of 40%) and mortar samples.

cured mortars shows that it corresponds with the hydration heat at the 41st hour [20]. In this study, the hydration temperatures in Figure 14 were found to be close to the values at the 41st hour. The pozzolanic materials used in the cement should not have an adverse impact on the mechanical strength of cement. With the increased replacement rate of fly ash and slag, the corresponding mechanical strength decreases when compared with standard samples.

3.6. Influence of Curing Age on Strength Development of Obsidian-Containing Cements.
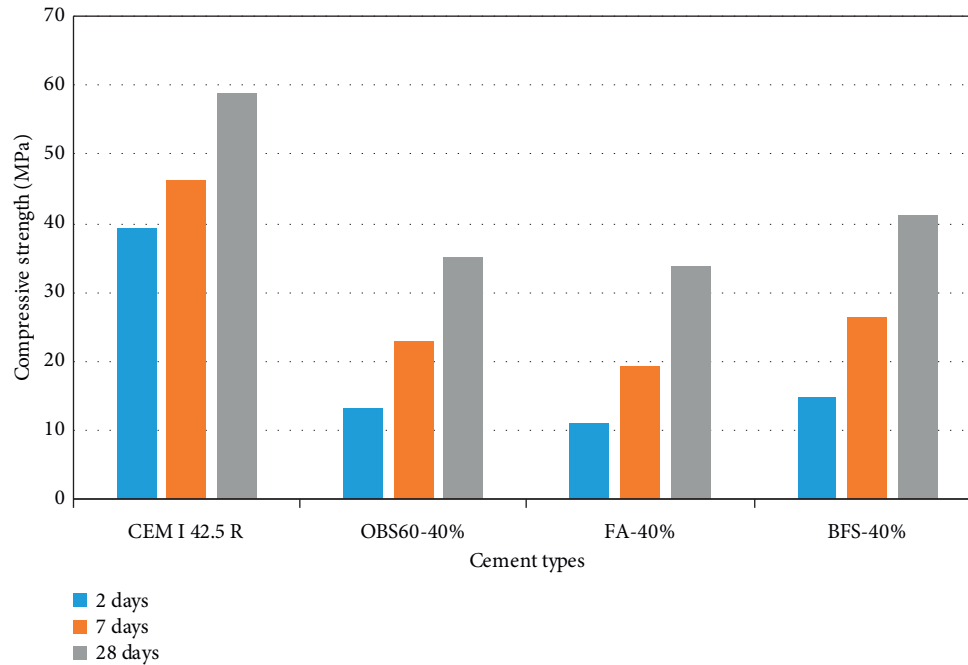Figure 15 shows the strengths obtained from CEM I 42.5R and mortar samples prepared as said by TS EN 196-1 with the cement mixed with 10%, 20%, 30%, and 40% obsidian for 60 min. As the rate of obsidian additives to cement increases, the corresponding compressive strength decreases.

3.7. Curing Time Effect on Strength Development of Additive-Containing Cements.
Figure 16 shows the strengths obtained from CEM I 42.5R (100%) and obsidian-, fly ash-, and slag-based cements at a rate of 40% and mortars prepared as said by TS EN 196-1. The highest strengths were found in CEM I 42.5R, followed by slag-, obsidian-, and fly ash-based cements, respectively.

Obsidian-blended cements behaved similarly to cements replaced with fly ash and slag additives concerning the strength performance as the pozzolan ratio increased. The mechanical strength value of 40% obsidian-based cement at 2, 7, and 28 days was more than that of cement-contained fly ash and lesser than that of cement-contained slag. Khan and Amin [11] found a 22.6% reduction in the 28-day strength value of 20% fly ash-containing cement when compared with

the standard sample. The strength value of 40% fly ash-added cements at 28 days was found to be 42.6% lower than that of the standard sample. The mechanical strength value of the fly ash-contained cement showed similar effects to the research work done by Khan and Amin [11]. When the mechanical strength values of obsidian and fly ash were compared, it was found that obsidian had a pozzolanic effect in the cement. Schöler et al. [27] demonstrated that the strength value of slag-containing cements is less than that of cement replaced with fly ash when compared with OPC, as seen in this study. This was attributed to the blast furnace slag forming a higher volume of hydration product due to its chemical composition.

4. Conclusions

In the present study, the following main conclusions have been drawn:

(i) Accumulation of additives to the unadulterated cement decreases the temperature difference value and the hydration temperature of cement.

(ii) Obsidian additive showed a behavior akin to other additives (fly ash or blast furnace slag) in terms of the impact of cement's hydration temperature.

(iii) Increasing the fineness of the pozzolan up to a certain level causes the highest temperature difference to occur earlier and the hydration temperature to increase. After the pozzolan fineness exceeds a certain value, this relationship cannot be determined clearly.

(iv) There is a tuneful relationship between the hydration heat value calculated by the TS EN 196-9 standard and the value calculated by the TS EN 196-8 method.

Data Availability

No data were used to support this study.

Conflicts of Interest

The authors declare that they have no conflicts of interest.

Acknowledgments

References

[1] TS 13515, *Complementary Turkish Standard for the Implementation of TS EN 206*, Turkish Standard, Ankara, Turkey, 2019.

[2] TS EN 197-1, *Cement – Part 1: Composition, Specification and Conformity Criteria for Common Cements*, Turkish Standard, Ankara, Turkey, 2012.

[3] I. Ustabas and F. Desik, "Transition coefficients between compressive strengths of samples with different shape and size in mass concrete and use of weight maturity method in dam construction," *Structural Concrete*, vol. 22, no. 1, pp. 696–709, 2021.

[4] M. K. Ardoga, S. T. Erdogan, and M. Tokyay, "Effect of particle size on early heat evolution of interground natural pozzolan blended cements," *Construction and Building Materials*, vol. 206, pp. 210–218, 2019.

[5] N. Y. Mostafa and P. W. Brown, "Heat of hydration of high reactive pozzolans in blended cements: isothermal conduction calorimetry," *Thermochimica Acta*, vol. 435, no. 2, pp. 162–167, 2005.

[6] I. Ustabaş and I. Omur, "The effect of the obsidian of the Rize region on the hydrating heat of cement," *Nevsehir Journal of Science and Technology*, vol. 8, pp. 78–87, 2019.

[7] S. H. Kosmatka, G. F. Yoigt, and P. Taylor, *Integrated Materials and Construction Practices for concrete Pavement: A State-Of-The-Practice Manual*, pp. 69–104, Iowa State University, Ames, IA, USA, 2006.

[8] I. Ustabas and A. Kaya, "Comparing the pozzolanic activity properties of obsidian to those of fly ash and blast furnace slag," *Construction and Building Materials*, vol. 164, pp. 297–307, 2018.

[9] TS25, *Natural Pozzolan (Trass) for Use in Cement and concrete - Definitions, Requirements and Conformity Criteria*, Turkish Standards, Ankara, Turkey, 2008.

[10] M. Saedi, K. Behfarnia, and H. Soltanian, "The effect of the Blaine fineness on the mechanical properties of the alkali-activated slag cement," *Journal of Building Engineering*, vol. 26, Article ID 100897, 2019.

[11] K. Khan and M. N. Amin, "Influence of fineness of volcanic ash and its blends with quarry dust and slag on compressive strength of mortar under different curing temperatures," *Construction and Building Materials*, vol. 154, pp. 514–528, 2017.

[12] M. I. Khan and A. M. Alhozaimy, "Properties of natural pozzolan and its potential utilization in environmental friendly concrete," *Canadian Journal of Civil Engineering*, vol. 38, no. 1, pp. 71–78, 2011.

[13] F. Moghaddam, V. Sirivivatnanon, and K. Vessalas, "The effect of fly ash fineness on heat of hydration, microstructure, flow and compressive strength of blended cement pastes," *Case Studies in Construction Materials*, vol. 10, Article ID e00218, 2019.

[14] Q. Niu, N. Feng, J. Yang, and X. Zheng, "Effect of superfine slag powder on cement properties," *Cement and Concrete Research*, vol. 32, no. 4, pp. 615–621, 2002.

[15] L. Ting, W. Qiang, and Z. Shiyu, "Effects of ultra-fine ground granulated blast-furnace slag on initial setting time, fluidity and rheological properties of cement pastes," *Powder Technology*, vol. 345, pp. 54–63, 2019.

[16] H. Binici, O. Aksogan, I. H. Cagatay, M. Tokyay, and E. Emsen, "The effect of particle size distribution on the properties of blended cements incorporating GGBFS and natural pozzolan (NP)," *Powder Technology*, vol. 177, no. 3, pp. 140–147, 2007.

[17] T. Baran and P. Pichniarczyk, "Correlation factor between heat of hydration and compressive strength of common cement," *Construction and Building Materials*, vol. 150, pp. 321–332, 2017.

[18] F. Han, X. He, Z. Zhang, and J. Liu, "Hydration heat of slag or fly ash in the composite binder at different temperatures," *Thermochimica Acta*, vol. 655, pp. 202–210, 2017.

[19] P. Thongsanitgarn, W. Wongkeo, A. Chaipanich, and C. S. Poon, "Heat of hydration of Portland high-calcium fly ash cement incorporating limestone powder: effect of limestone particle size," *Construction and Building Materials*, vol. 66, pp. 410–417, 2014.

[20] V. Tydlitát, J. Zákoutský, and R. Černý, "Early-stage hydration heat development in blended cements containing natural zeolite studied by isothermal calorimetry," *Thermochimica Acta*, vol. 582, pp. 53–58, 2014.

[21] S. T. Erdogan and T. Kocak, "Influence of slag fineness on the strength and heat evolution of multiple- clinker blended cements," *Construction and Building Materials*, vol. 155, pp. 800–810, 2017.

[22] M. K. Saeed, M. K. Rahman, and M. H. Baluch, "Influence of steel and polypropylene fibers on cracking due to heat of hydration in mass concrete structures," *Structural Concrete*, vol. 20, no. 2, pp. 808–822, 2019.

[23] P. C. Taylor, S. H. Kosmatka, and G. F. Voigt, *Integrated Materials and Construction Practices for concrete Pavement: A State-Of-The-Practice Manual*, p. 338, National Concrete Pavement Technology Center, Iowa State University, Ames, IA, USA, 2006.

[24] J. W. Bullard, H. M. Jennings, R. A. Livingston et al., "Mechanisms of cement hydration," *Cement and Concrete Research*, vol. 41, no. 12, pp. 1208–1223, 2011.

[25] M. Demir, T. Erenoglu, H. Ekim, and M. A. Tasdemir, "Effects of fineness and amount of fly ash on strength development of concrete," in *Proceedings of the 5th International Congress on Advances in Civil Engineering*, pp. 1349–1358, Istanbul, Turkey, September 2002.

[26] T. Merzouki, M. Bouasker, N. E. Houda Khalifa, and P. Mounanga, "Contribution to the modeling of hydration and chemical shrinkage of slag-blended cement at early age," *Construction and Building Materials*, vol. 44, pp. 368–380, 2013.

[27] A. Schöler, B. Lothenbach, F. Winnefeld, and M. Zajac, "Hydration of quaternary Portland cement blends containing blast-furnace slag, siliceous fly ash and limestone powder," *Cement and Concrete Composites*, vol. 55, pp. 374–382, 2015.

[28] T. S. En 196-8, *Methods of Testing Cement - Part 8: Heat of Hydration - Solution Method*, Turkish Standard, Ankara, Turkey, 2011.

Research Article

Towards the Understanding of Damage Mechanism of Cemented Tailings Backfill

Haijun Wang [1,2]

[1]*BGRIMM Technology Group, Beijing 100160, China*
[2]*School of Resource and Civil Engineering, Northeastern University, Shenyang 110819, China*

Correspondence should be addressed to Haijun Wang; 2957577750@qq.com

Recent studies have shown that the damage characteristics of cemented tailings backfill (CTB) are influenced significantly by the variation of cement-tailings ratio, while the effects of other influencing factors remain unanswered. The CTB damage constitutive model, which takes the corrected coefficient of damage variable into consideration, and peak toughness are introduced to investigate the effects of fine tailings contents, curing ages, curing temperatures, and water-to-cement ratios (w/c) on the damage evolution laws, damage (D_P), and specific energy (G_P) at peak stress point of CTB. The results show that appropriate content of fine tailings could improve the compressive strength of CTB and reduce its damage evolution speed and D_P. The damage growth rate of CTB decreases with curing age in early curing period and increases with higher curing temperature and w/c. D_P of CTB takes on a descending trend with higher w/c and fine tailings content but shows an increase with curing age. There exists no significant relationship between D_P and curing temperature. G_P of CTB increases with curing age and higher curing temperature with a quadratic function but is on a decline with increases of fine tailings content and w/c with logarithmic and exponential function, respectively. The results obtained from our study have important application to the successful design of backfill structures in underground mines.

1. Introduction

The backfill mining method has been increasingly used in underground goaf treatment in mines worldwide, as it can effectively reduce the accumulation of surface waste and alleviate the pressure of mining operations on the surrounding environment [1–4]. From the perspective of engineering application, this mining method can effectively control the mining site pressure, reduce ore loss and dilution, and ensure the safety of underground personnel and equipment [5–10]. Cemented tailings backfill (CTB) is an essential part of the backfilling method, mainly made of tailings, cementitious materials (such as cement, fly ash, and blast furnace slag), and water in a particular proportion [11, 12]. Its mechanical properties are influenced by internal factors, e.g., the physical and chemical properties of tailings, water-cement (w/c) ratio, content and type of cementitious materials, and external factors such as curing environment

(e.g., temperature and temperature humidity) and curing age [13, 14]. As a multiphase composite medium, CTB contains initial defects such as pores, microcracks, and bubbles, resulting in the initial damage characteristics [15]. Overall, the CTB has unique failure characteristics. The stress-strain curve is unique in reflecting the failure characteristics of materials, which is commonly used to describe the damage and failure process of CTB [16].

In recent years, many scholars have conducted in-depth studies on the damage constitutive model and damage characteristics of CTB. For example, Shulin and Yufa [17] analysed the CTB's failure mechanism with a cement-tailings (c/t) ratio of 1 : 6 from the mesoscale level using solid mechanics. The damage constitutive equation of CTB under uniaxial compression was given based on the test results. Deng et al. [18] conducted uniaxial compression and split tensile tests on CTB sampled from underground backfill stopes and established the damage constitutive models using

elastic damage theory. Liu et al. [19–21], Guicheng et al. [15], and Qiu et al. [22] established the prepeak and postpeak damage constitutive equations of CTB under uniaxial compression tests based on the strain equivalence principle, and their results had been used to guide the design in practice. Xie et al. [23] defined a damage variable based on the cumulative energy of acoustic emission and established a damage constitutive model for the CTB with a c/t ratio of 1: 8. Gong et al. [24] noticed that under the uniaxial cyclic loading and unloading conditions, the b value of acoustic emission of CTB with a c/t ratio of 1:4 showed different characteristics, indicating the dynamic evolution of the microfracture inside CTB. Zhang et al. [25] derived the damage constitutive model of cemented waste rock backfill and studied the effect of waste rock content on their damage characteristics. Yu et al. [26] proposed that the CTB stress would transfer when the damage occurs. Accordingly, they established the damage constitutive models of CTB with different c/t ratios containing damage correction factors. Wang et al. [16] established the temperature-time coupled damage constitutive model of CTB based on the stress-strain curves under different initial temperatures and curing ages. Ke et al. [27] noted that the cubic polynomial function matched well with stress-strain curves of CTB with various c/t ratios.

To sum up, those studies have shed light on the damage evolution and characteristics of CTB. However, they mainly concentrated on the influence of the c/t ratio, and the effects of other factors, e.g., w/c ratio, curing age, and fine tailings content, on the damage characteristics of CTB are rarely reported. Thus, this study introduces a modified damage constitutive model to characterize the uniaxial compression stress-strain curves of CTB with various curing ages, curing temperatures, fine tailings contents, and c/t ratios based on reported data and then analyse these factors' effects on the damage evolution behaviour. The peak toughness concept was also introduced to compare the damage value and specific energy at peak stress point. Our thorough study benefits to the enhanced understanding on the CTB's damage mechanism and the successful design of backfilling technique in practice.

2. Damage Constitutive Models for Cemented Tailings Backfill

It has been well recognized that the CTB contains random distribution of microcracks before failure and belongs to a kind of heterogeneous continuous medium. When the CTB is subjected to an external load, these defects will further expand and form macrocracks after reaching failure through a complex damage mechanism. The damage mechanic principle is suitable for describing this kind of damage mechanism, and thus it is widely used in concrete [28, 29], rock [30, 31], and cemented backfill materials [21], such as the Weibull and Mazars damage models. In the Weibull damage model, both CTB strength and damage variable follow the Weibull distribution function, and the damage constitutive model under uniaxial compression is given as

$$\sigma = E\varepsilon \left\{ \exp\left[-\frac{1}{m}\left(\frac{\varepsilon}{\varepsilon_p} \right)^m \right] \right\},$$

$$D = 1 - \exp\left[-\frac{1}{m}\left(\frac{\varepsilon}{\varepsilon_p} \right)^m \right], \quad (1)$$

$$m = \frac{1}{\ln\left(E\varepsilon_p / \sigma_P \right)},$$

where σ is the stress; E is Young's modulus; ε is the strain; ε_p is the strain at peak stress point; m is the shape parameter of the Weibull function; D is the damage variable; and σ_P is the peak stress. The Mazars model assumes that the CTB behaves almost linearly at prepeak stage and performs like the evolution behaviour of concrete at postpeak stage [20]. Before peak stress, the Mazars model for CTB is written as

$$\sigma = E\varepsilon - EA\varepsilon^{\beta+1},$$

$$D = A\varepsilon^\beta, \quad (2)$$

where A and β are two constants, in which $\beta = \sigma_p/(E\varepsilon_p - \sigma_p)$ and $A = 1/(\varepsilon_p^\beta + \beta\varepsilon_p^\beta)$. At postpeak stage, the stress and damage evolution model of CTB in the Mazars model is given as

$$\sigma = -ED_p\varepsilon + E\varepsilon \exp\left[-B\left(\varepsilon - \varepsilon_p \right) \right],$$

$$D = D_p + 1 - \exp\left[-B\left(\varepsilon - \varepsilon_p \right) \right]. \quad (3)$$

Note that the Weibull and Mazars models do not consider the influence of residual strength, which may not efficient enough to reflect the postpeak behaviour of CTB. Therefore, a correction factor α was incorporated into the Weibull model (referred to as modified Weibull model for short). α mainly influences the postpeak stage of CTB's stress-strain curve and has minor effect on the prepeak stage. In the modified Weibull model, the stress and damage evolutions of CTB are expressed as

$$\sigma = E\varepsilon \left[\alpha \exp\left(-\left(\frac{F}{F_0} \right)^m \right) + 1 - \alpha \right],$$

$$D = 1 - \exp\left[-\left(\frac{F}{F_0} \right)^m \right], \quad (4)$$

where F is the microcosmic element strength of CTB and m and F_0 are the shape parameters of the Weibull function, which can be deduced by

$$F = \left(\frac{\sin\varphi}{\sqrt{9 + 3\sin^2\varphi}} + \frac{1}{\sqrt{3}} \right)E\varepsilon_p,$$

$$m = \frac{\left(\sigma_p/E\varepsilon_P\left(\left(\sigma_p/E\varepsilon_P \right) + \alpha - 1 \right) \right)}{\ln\alpha - \ln\left(\left(\sigma_p/E\varepsilon_P \right) + \alpha - 1 \right)}, \quad (5)$$

$$F_0 = \frac{F}{\exp\left\{ \left(\ln\left[\ln\alpha - \ln\left(\left(\sigma_p/E\varepsilon_P \right) + \alpha - 1 \right) \right]/m \right) \right\}},$$

where ϕ is the internal friction angle of CTB.

The stress-strain curves of CTB with a c/t ratio of $1:4$ given in [20] are selected to compare the performance of these three damage constitutive models in characterizing the stress and damage evolutions of CTB, as shown in Figure 1. It can be seen from Figure 1(a) that the stress-strain curves obtained by the three damage models before the peak stress are almost the same, and the stress-strain curves of the initial deformation and elastic stage of the CTB are regarded as straight lines. As the CTB enters the yield stage, the slope of the curve gradually decreases to 0. In the failure stage of CTB, the stress prediction value of the Mazars damage model is closer to the test result because of the consideration of residual strain, but the failure rate is higher than the test curve. Although the stress values obtained by equations (1) and (5) are slightly larger, they are consistent with the actual values, and the damage failure rate is more consistent with the test curve. The residual strength of cemented backfill is susceptible to the damage correction coefficient α, while the curve changes slightly in the prepeak stage. It can be seen from Figure 1(b) that the changing trend of damage value D obtained according to the three different damage evolution equations is the same. Before the peak stress, the damage of CTB increases slowly with the increase of stress value. When the stress value reaches the peak stress, the damage increases rapidly, indicating the formation of macrocracks and the rapid instability of the CTB. When the c/t ratio is $1:4$, the larger the correction coefficient α is, the slower the damage growth before the peak of the CTB is and the more significant the damage growth after the peak is. For the modified Weibull damage model, when the damage variable correction coefficient $\alpha = 1$, it is equivalent to the Weibull damage model before correction.

In summary, the three damage constitutive models can reflect the stress-strain behaviour and damage failure process of the filling body under uniaxial compression reasonably, but an effective damage correction coefficient should be selected for the modified Weibull damage model. Although the model proposed in [20] is more consistent with the experimental results, the postpeak damage rate is significantly higher than the experimental curve. The residual strain value of the filling body under uniaxial compression is not easy to determine. Therefore, in the third part of the paper, the modified Weibull damage model is selected to study the influence of different factors on the damage characteristics of the filling body. The determination method of the correction coefficient of the reasonable damage variable is shown in [26].

3. Damage Characteristics of Cemented Tailings Backfill

3.1. Effect of Fine Tailings Content. Fall et al. [13] conducted uniaxial compression tests on CTB with various fine tailings contents (30%, 50%, 70%, and 80%). The axial displacement loading rate was 1 mm/min. The measured results and the fitting results obtained from the modified Weibull damage model are shown in Figure 2(a). As shown in the figure, the higher the fine tailings content, the smaller the filling body's

peak strength and elastic modulus. When the fine tailings content is greater than 50%, the peak strength of the filling body decreases by 46.0% and 57.6%, respectively. When the fine tailings content is between 30% and 50%, the peak strength increases slowly by only 4.2%. The reason for this is that the porosity of the CTB decreases with the decrease of the fine tailings content, which promotes the increase of bonding strength between the tailings and the cement base [13, 32]. It can be seen from Figure 2(a) that the results obtained by fitting with the modified damage model are consistent with the experimental data, and the fine tailings content in the cemented filling body has a significant impact on its mechanical behaviour.

Figure 2(b) shows the result of damage evolution versus strain of CTB with different fine tailings contents. As shown in the figure, the damage development trend is like an S-type growth. When the fine tailings content is greater than 50%, the damage growth rate increases with fine tailings content. When the fine tailings content is 30%–50%, the higher the fine tailings content, the slower the damage growth. Figure 2(c) presents the damage values of CTB at peak stress points corresponding to different fine tailings contents. When the fine tailings content increases from 30% to 80%, the corresponding D_p is 0.61, 0.13, 0.57, and 0.51, respectively. These calculation results show that the higher the fine tailings content is, the smaller the damage value at the peak point is. It is noteworthy that the CTB with 50% fine tailings content has the advantages of high peak strength and slow damage growth, indicating that appropriate fine tailings can improve the mechanical properties of the CTB.

The deformation and damage processes of cemented backfill relate to the energy dissipation and release [7]. Under the action of external load, CTB absorbs most of the energy and uses it in the initial deformation stage. When the input energy is greater than the specific energy of the CTB (the energy absorption value at the peak stress point), the excess energy will lead to the evolution, accumulation, and coalescence of microcracks in the CTB until macrocracks occur. The concept of peak toughness in high-performance reinforced fibre reinforced concrete (HPFRC) is introduced herein, and the area under the stress-strain curve before the peak stress point is defined as the specific energy at the peak stress point of the CTB [33]. Figure 2(d) shows that specific energy of CTB with different fine tailings contents is 4.76×10^{-3} J/m^3 (30%), 2.86×10^{-3} J/m^3 (50%), 2.09×10^{-3} J/m^3 (70%), and 1.34×10^{-3} J/m^3 (80%), respectively, indicating that the specific energy decreases with the increase of fine tailings content. By fitting the data in Figure 2(d), the relationship between specific energy and fine tailings content is a logarithmic function, and the fitting correlation coefficient R2 is about 0.99. The relationship between the two is expressed as $Y = a \ln X + b$, where Y is the specific energy, X is the fine tailings content, and a and b are the fitting correlation coefficients.

3.2. Effect of Curing Ages. Ghirian and Fall [12] studied the deformation characteristics of CTB with different curing
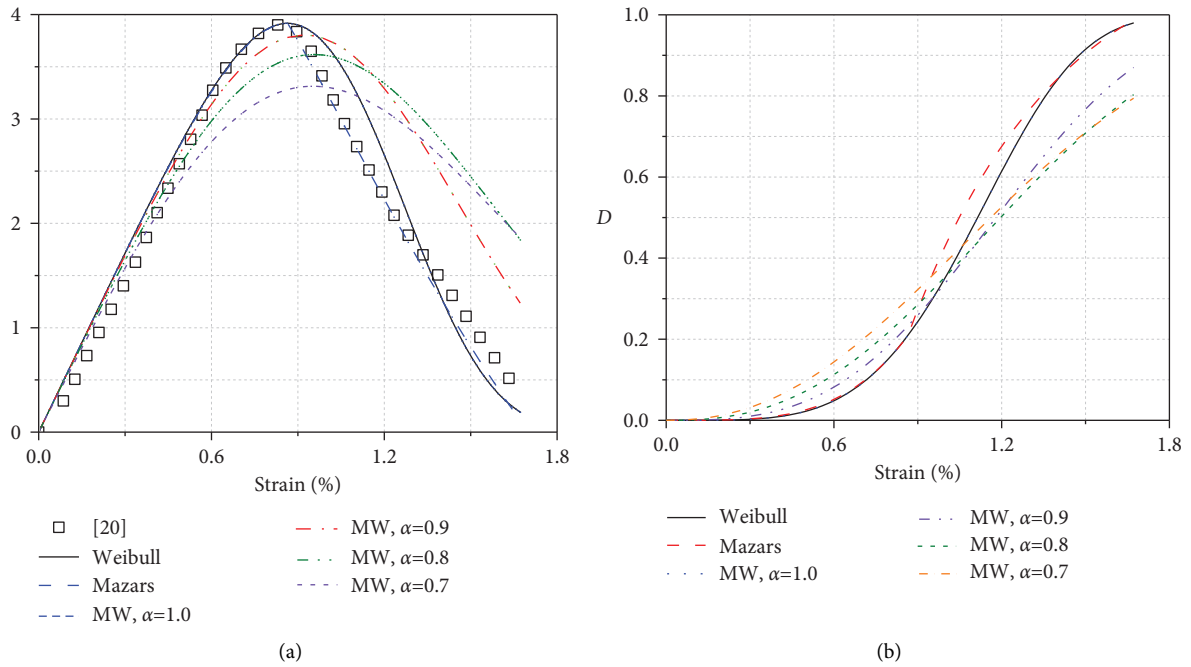
(a)

(b)

FIGURE 1: Damage failure process of CTB with a *c/t* ratio of 1 : 4: (a) stress-strain curves and (b) *D* vs. strain curves.
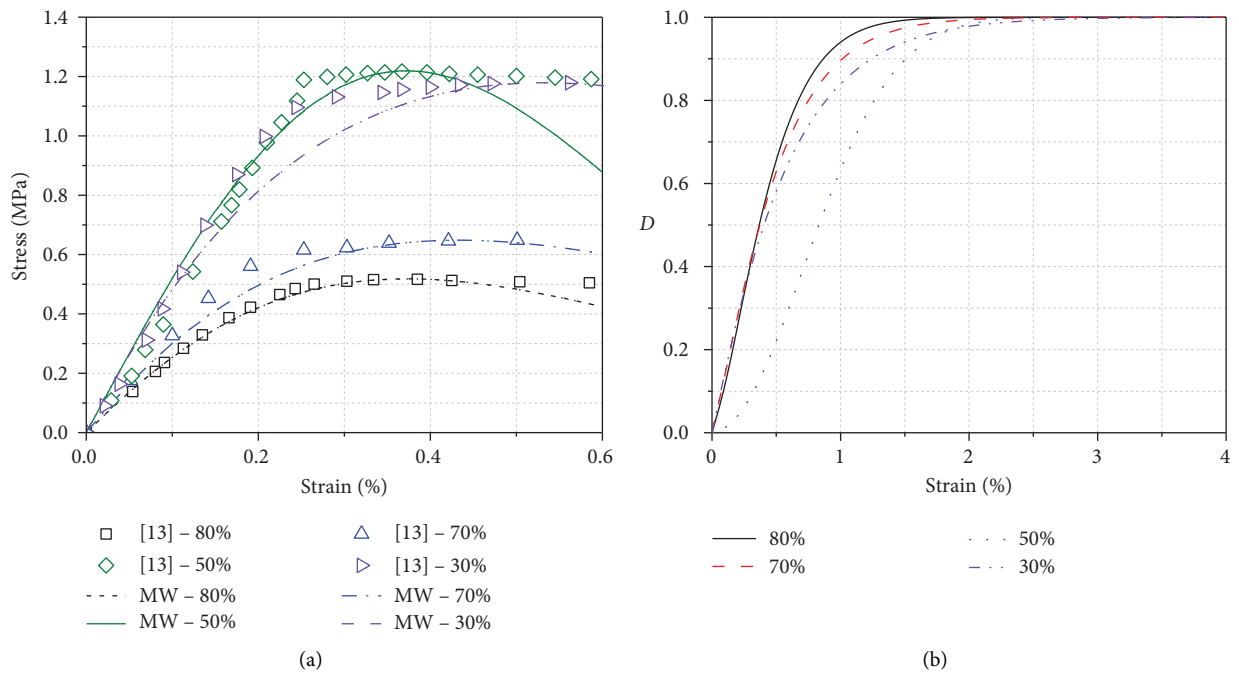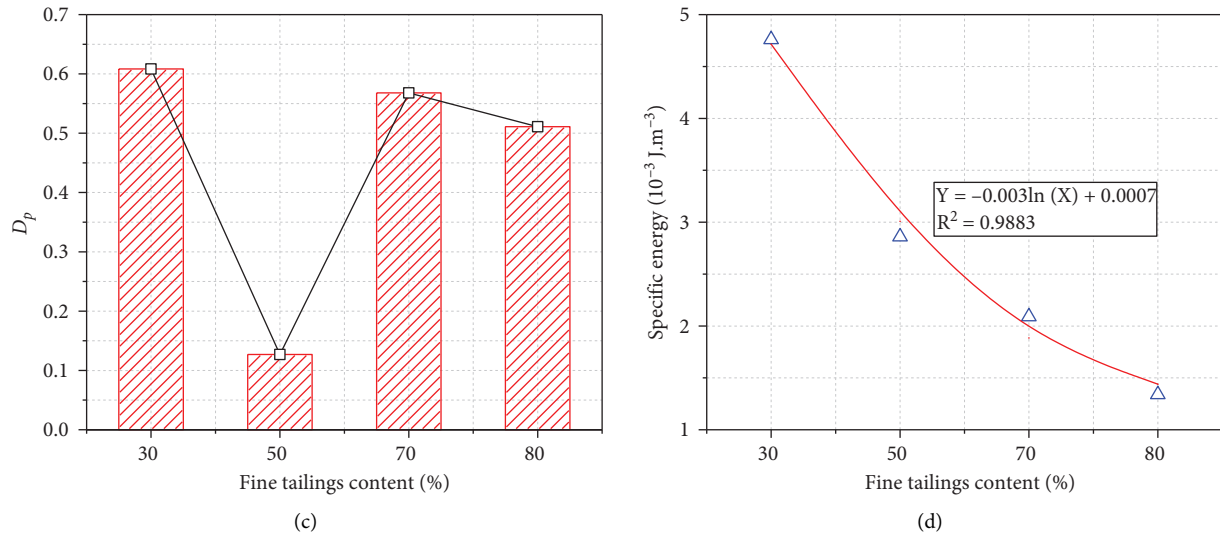

(a)

(b)

FIGURE 2: Continued.

(c)

(d)

FIGURE 2: The effect of fine tailings content on damage characteristics of CTB. (a) Measured and theoretical stress-strain curves. (b) D vs. strain curves. (c) D_P vs. fine tailings content curve. (d) G_P vs. fine tailings content curve.

ages (7, 28, 90, and 150 days) under uniaxial compression with an axial displacement loading rate of 1.14 mm/min, as shown in Figure 3(a). It can be seen from Figure 3(a) that the stress-strain behaviour of the backfill is significantly affected by curing ages, and the curves obtained from the modified Weibull damage model are in good agreement with the experimental results. Compared with the curing age of 7 days and 28 days, the long-term cured CTB can obtain higher peak strength and elastic modulus, but the peak strain decreases. The longer the curing age is, the more complete the hydration reaction inside the filling body is and the more the hydration products such as calcium silicate, C-S-H gel, and ettringite are produced, and the strength characteristics and durability of the material are further improved [34]. When the curing age is short, the CTB shows plastic deformation. With the increase of curing age, the filling body gradually shows brittle behaviour. It is because the CTB with a higher strength absorbs more energy before reaching the peak stress point and thus benefits the propagation of internal microcracks. As a result, the deformation of CTB after reaching peak stress point is more severe, together with the abrupt reduction in strength.

Figure 3(b) shows the change curve of the damage evolution of CTB with strain at different curing ages. As shown in the figure, the damage value increases with the increase of strain in an S-shaped curve. When the curing age is short (less than 28 days), the damage growth rate of CTB is inversely proportional to the curing age. Compared with the CTB with shorter curing ages, the damage evolution of CTB with longer curing ages is divided into two stages. Before the peak stress point, the damage growth is slow and the shorter the curing age is, the slower the damage growth rate is. After peak stress, the damage of CTB increases rapidly. The shorter the curing age is, the faster the damage growth rate is. Figure 3(c) shows the damage value corresponding to the peak point of the CTB

at different curing ages. The 7-day cured CTB's damage value at peak stress point is about 0.35. When the curing age increases to 28, 90, and 150 days, the corresponding Dp is 0.50, 0.42, and 0.51, respectively. Overall, the damage value of CTB at peak stress point increases with the increase of curing age.

Figure 3(d) shows the curve of the peak stress ratio energy of the filling body changing with the curing age. The specific energy corresponding to different curing ages (7, 28, 90, and 150 days) is 3.98×10^{-3} J/m^3, 5.06×10^{-3} J/m^3, 5.11×10^{-3} J/m^3, and 9.31×10^{-3} J/m^3, respectively. It indicates that the longer the curing age is, the more the energy absorbed by the CTB when it reaches the peak stress point is and the greater the peak stress ratio energy is. The statistical regression analysis of the curve shows that the specific energy has a quadratic function relationship with the curing age, and the fitting correlation coefficient is about 0.94. The relationship between the two is expressed as $Y = aX^2 + bX + c$ where Y is the specific energy at the peak stress point, X is the curing age, and a, b, and c are the test correlation coefficients.

3.3. Effect of Curing Temperatures. The influence of curing temperature on the uniaxial deformation characteristic of CTB was studied in [35]. The experimental results, together with theoretical curves obtained from the modified Weibull damage model, are shown in Figure 4(a). As shown in the figure, a good agreement is obtained between the experimental and predicted results. The higher the curing temperature, the greater the elastic modulus of the CTB, the higher the peak strength, and the smaller the strain at the peak stress point. When the curing temperature increased from 20°C to 50°C, the peak strength increased by 81.6% (20°C), 133.9% (35°C), and 374.1% (50°C), respectively, and the peak strain decreased by 24.8%, 39.7%, and 69.9%, respectively. The reasons why an
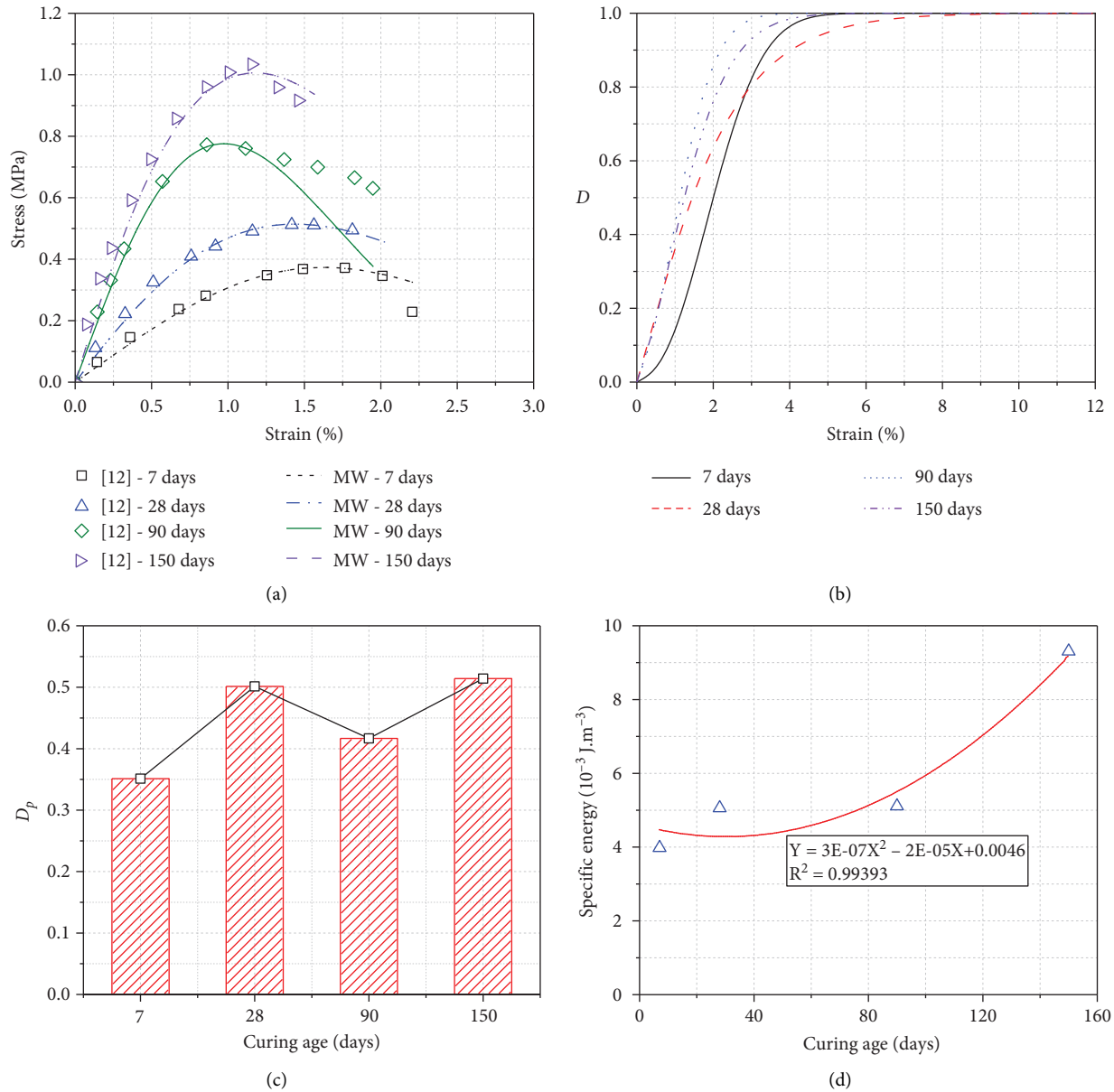
(a)

(b)

(c)

(d)

Figure 3: The effect of curing ages on damage characteristics of CTB. (a) Measured and theoretical stress-strain curves. (b) D vs. strain curves. (c) D_P vs. curing age curve. (d) G_P vs. curing age curve.

appropriate high temperature can promote the strength growth of the CTB are mainly the following two aspects. Firstly, it promotes the cement hydration reaction in the CTB and generates more hydration products such as C-S-H gel [35, 36] to improve its peak strength and stiffness and shorten its postpeak deformation period [35]. Secondly, the increase of temperature accelerates the capillary water consumption rate and promotes the development of pore water pressure in the filling body, resulting in higher strength [37].

Figure 4(b) shows the curve of damage value changing with strain under different curing temperatures. When the curing temperature is 20°C and 50°C, the damage shows an S-shaped curve. The damage increases slowly before the peak point and rapidly after the peak point. When the curing temperature was

20°C and 35°C, the damage evolution rate of the CTB gradually decreases with the increase of strain. Also, the damage increases rapidly before the peak stress point, while the damage increases slowly after the peak point, showing the characteristics of strain softening. Figure 4(c) shows that when the curing temperature is less than 20°C, the damage value at the peak stress point increases with the increase of curing temperature. When the temperature is more significant than 20°C, the peak damage value decreases with the increase of curing temperature. For the CTB with a curing temperature of 50°C, the damage value increases rapidly to 1 after the peak stress point, indicating that the CTB gradually exhibits brittle characteristics with the increase of curing temperature.

Figure 4(d) shows the peak specific energy curves of backfill at different curing temperatures. When the initial
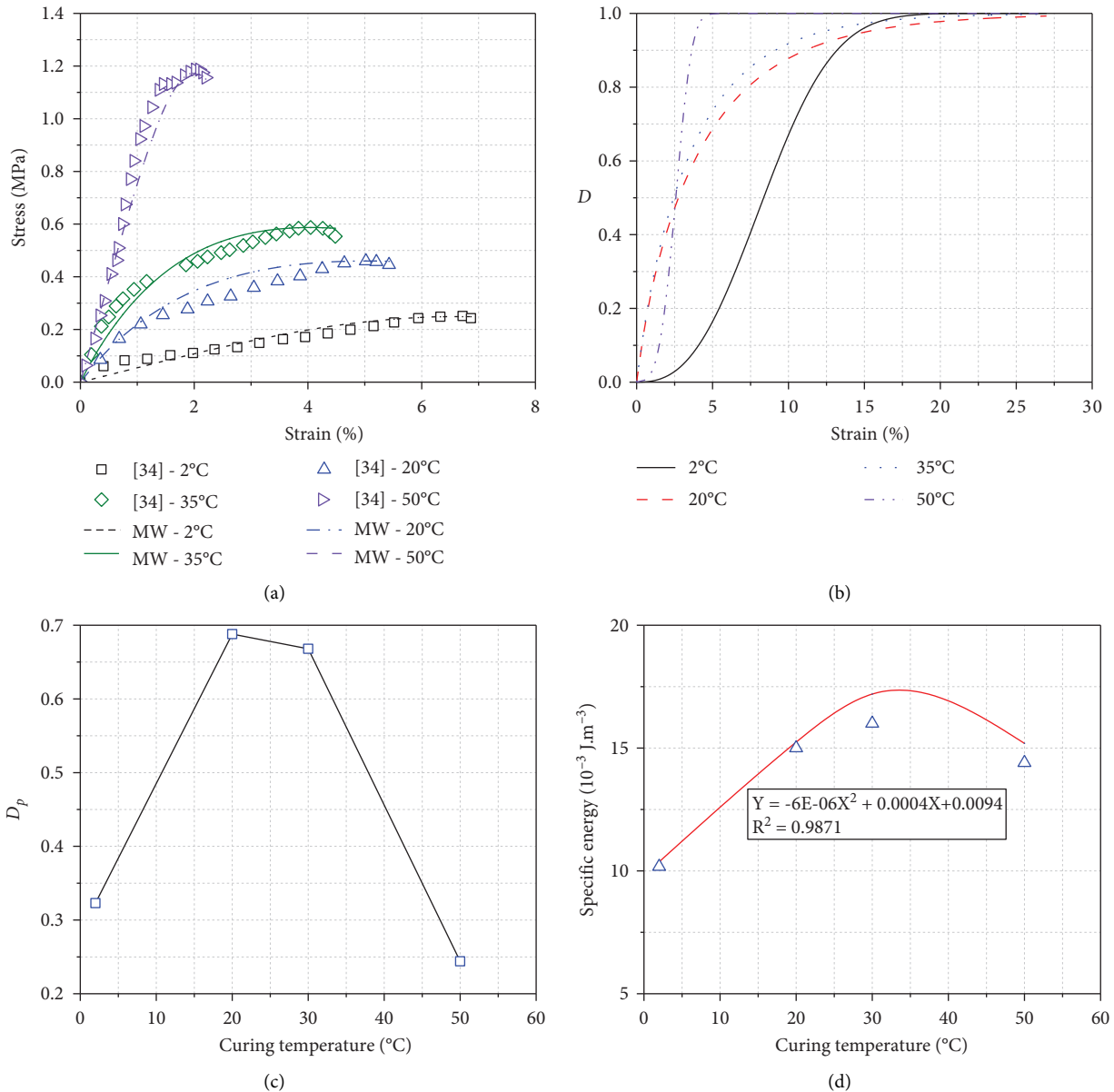
FIGURE 4: The effect of curing temperatures on damage characteristics of CTB. (a) Measured and theoretical stress-strain curves. (b) D vs. strain curves. (c) D_P vs. curing temperature curve. (d) G_P vs. curing temperature curve.

curing temperature is 2℃, the peak strain ratio of the backfill is 1.04×10^{-3} J/m³. When the curing temperature increases to 20℃, 35℃, and 50℃, the specific energy of the backfill is 1.47, 1.66, and 1.46 times that of 20℃. It denotes that when the curing temperature is less than 35℃, the specific energy increases with the increase of temperature. When the curing temperature exceeds 35℃, the peak strain ratio energy decreases gradually. The regression analysis shows that the specific energy has a quadratic relationship with the curing temperature, and the fitting correlation coefficient R2 is about 0.99. The relationship between the two is expressed as $Y = aX^2 + bX + c$ where Y is the specific energy at the peak stress point, X is the curing temperature, and a, b, and c are the correlation coefficients.

3.4. *Effect of Water-Cement Ratios.* The stress-strain behaviour of fillings with different w/c ratios (7, 10, and 13) under uniaxial compression was studied in [13]. The experimental results are compared with the predicted curves obtained from the modified Weibull damage model in Figure 5(a). The theoretical curves show a good agreement with the experimental results. The stress-strain curve of the CTB is significantly affected by the water-cement ratio. The peak strength, residual strength, and elastic model of the CTB increase with the decrease of the water-cement ratio. The decrease of the water-cement ratio will increase the content of columnar ettringite in the filling body and reduce the porosity in the CTB, and the porosity is inversely proportional to the material strength [38]. When the water-cement ratio is 7, the corresponding peak strength is
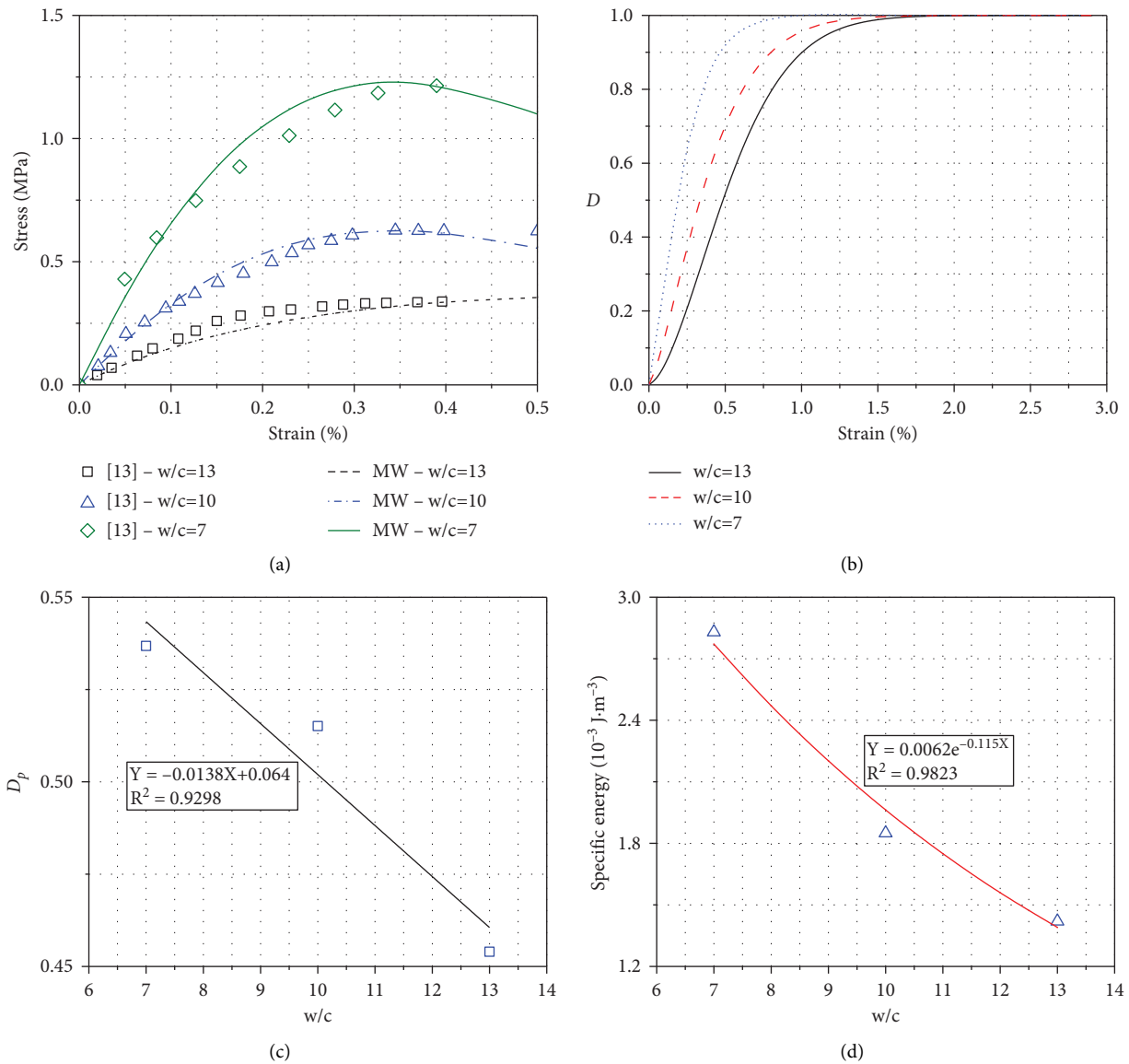
FIGURE 5: The effect of water-to-cement ratios on damage characteristics of CTB. (a) Measured and theoretical stress-strain curves. (b) D vs. strain curves. (c) D_P vs. water-to-cement curve. (d) G_P vs. water-cement ratio curve.

1.23 MPa. When the water-cement ratio increases to 10 and 13, the peak strength of the CTB decreases to 0.63 MPa and 0.37 MPa, respectively.

Figure 5(b) shows the curve of the damage value of the CTB with different water-cement ratios. The damage value of the CTB increases with the increase of strain, and the smaller the water-cement ratio, the faster the damage growth of the CTB. As shown in Figure 5(c), the damage values corresponding to the peak stress point are 0.54, 0.52, and 0.45 when the water-cement ratio of the CTB is 7, 10, and 13, respectively. The regression analysis of the data shows that the damage value of the peak stress point is linearly related to the water-cement ratio and decreases linearly with the increase of the water-cement ratio. The fitting correlation coefficient is about 0.93, indicating that there is a high regularity between the two. The relationship between the two is expressed as $Y = aX + b$, where Y is the

damage value corresponding to the peak stress point, X is the water-cement ratio, and a and b are the correlation coefficients.

Figure 5(d) shows the variation curve of specific energy with the water-cement ratio. The figure shows that when the initial water-cement ratio is 7, the specific energy is determined as 2.83×10^{-3} J/m³. When the water-cement ratio increases to 10 and 13, respectively, the specific energy of CTB decreases by 34.63% and 49.83%. This shows that the smaller the water-cement ratio, the more the energy absorbed by the CTB when reaching the peak point, and the greater the strength. The data fitting between specific energy and water-cement ratio has an obvious exponential function, and the correlation coefficient is as high as 0.98. The relationship between them is $Y = Ae^{BX}$, where Y is the specific energy of the CTB, X is the water-cement ratio, and A and B are the test correlation coefficients.

It is well known that the leaching risk from CPB to groundwater proposed by Chen et. al. has been an important issue in mining engineering, which will be further studied in our future research.

4. Conclusions

In this study, a modified Weibull damage model is introduced to characterize the damage mechanism of cemented tailings backfill with various curing ages, curing temperatures, water-cement ratios, and fine tailings contents. Based on the results, the following conclusions can be drawn:

(1) As a kind of multiphase composite material containing initial defects such as microcracks and pores, CTB's mechanical properties and damage characteristics are significantly affected by the fine tailings content, curing age, curing temperature, and water-cement ratio.

(2) The damage growth rate of CTB increases with fine tailings content when the fine tailings content is more than 50% but decreases when the content of fine tailings is less than 50%. It indicates that appropriate content of fine tailings can effectively improve the mechanical properties of the CTB. The damage growth rate is inversely proportional to the curing age for the CTB with low curing age. For long-term curing CTB, the more significant the curing age, the faster the damage growth before the peak stress point and the slower the damage growth after the peak stress point. With the increase of curing temperature, the CTB gradually shows brittle behaviour. The higher the curing temperature, the faster the damage growth rate of the CTB and the more sudden the failure process. The greater the water-cement ratio, the faster the damage development inside CTB.

(3) The damage value at the peak stress point of the CTB decreases with the increase of fine tailings content (except 50%), decreases with the increase of water-cement ratio, and increases gradually with the increase of curing age but does not show apparent regularity with the curing temperature.

(4) The specific energy is the energy absorbed at the peak stress point, proportional to the uniaxial compressive strength of CTB. The specific energy grows in a quadratic polynomial manner with the increase of curing age and curing temperature, decreases logarithmically with fine tailings content, and follows the exponential reduction law with increasing water-cement ratio.

Data Availability

The data used to support the findings of this study are included within the article.

Conflicts of Interest

The author declares that there are no conflicts of interest.

References

[1] M. Benzaazoua, M. Fall, and T. Belem, "A contribution to understanding the hardening process of cemented pastefill," *Minerals Engineering*, vol. 17, no. 2, pp. 141–152, 2004.

[2] A. Ghirian and M. Fall, "Coupled thermo-hydro-mechanical-chemical behaviour of cemented paste backfill in column experiments. part I: physical, hydraulic and thermal processes and characteristics," *Engineering Geology*, vol. 164, pp. 195–207, 2013.

[3] L. Li, "Generalized solution for mining backfill design," *International Journal of Geomechanics*, vol. 14, no. 3, Article ID 04014006, 2014.

[4] Z. Guo, J. Qiu, H. Jiang, S. Zhang, and H. Ding, "Improving the performance of superfine-tailings cemented paste backfill with a new blended binder," *Powder Technology*, vol. 394, 2021.

[5] F. Cihangir, B. Ercikdi, A. Kesimal, A. Turan, and H. Deveci, "Utilisation of alkali-activated blast furnace slag in paste backfill of high-sulphide mill tailings: effect of binder type and dosage," *Minerals Engineering*, vol. 30, pp. 33–43, 2012.

[6] Z. Guo, J. Qiu, H. Jiang, J. Xing, X. Sun, and Z. Ma, "Flowability of ultrafine-tailings cemented paste backfill incorporating superplasticizer: insight from water film thickness theory," *Powder Technology*, vol. 381, pp. 509–517, 2021.

[7] J. Qiu, L. Yang, X. Sun, J. Xing, and S. Li, "Strength characteristics and failure mechanism of cemented super-fine unclassified tailings backfill," *Minerals*, vol. 7, no. 4, p. 58, 2017.

[8] S. Yin, A. Wu, K. Hu, Y. Wang, and Y. Zhang, "The effect of solid components on the rheological and mechanical properties of cemented paste backfill," *Minerals Engineering*, vol. 35, pp. 61–66, 2012.

[9] T. Belem and M. Benzaazoua, "Design and application of underground mine paste backfill technology," *Geotechnical & Geological Engineering*, vol. 26, no. 2, pp. 147–174, 2008.

[10] M. Fall, M. Benzaazoua, and S. Ouellet, "Experimental characterization of the influence of tailings fineness and density on the quality of cemented paste backfill," *Minerals Engineering*, vol. 18, no. 1, pp. 41–44, 2005.

[11] B. Ercikdi, G. Külekci, and T. Yılmaz, "Utilization of granulated marble wastes and waste bricks as mineral admixture in cemented paste backfill of sulphide-rich tailings," *Construction and Building Materials*, vol. 93, pp. 573–583, 2015.

[12] A. Ghirian and M. Fall, "Coupled thermo-hydro-mechanical-chemical behaviour of cemented paste backfill in column experiments," *Engineering Geology*, vol. 170, pp. 11–23, 2014.

[13] M. Fall, T. Belem, S. Samb, and M. Benzaazoua, "Experimental characterization of the stress-strain behaviour of cemented paste backfill in compression," *Journal of Materials Science*, vol. 42, no. 11, pp. 3914–3922, 2007.

[14] J. Qiu, Z. Guo, L. Yang, H. Jiang, and Y. Zhao, "Effects of packing density and water film thickness on the fluidity behaviour of cemented paste backfill," *Powder Technology*, vol. 359, pp. 27–35, 2020.

[15] H. Guicheng, L. Shenglong, and H. Bingxiang, "Reasonable matching for cemented waste rock backfill and sand shale,"

Journal of Mining & Safety Engineering, vol. 34, no. 2, pp. 371–377, 2017.

[16] Y. Wang, A. Wu, H. Wang et al., "Damage constitutive model of cemented tailing paste under initial temperature effect," *Chinese Journal of Engineering*, vol. 39, no. 1, pp. 31–38, 2017.

[17] L. Shulin and S. Yufa, "The fracture mechanism and damage constitutive equation of cemented tail filling," *Gold*, vol. 18, pp. 24–29, 1997.

[18] D. Deng, Y. Yang, and Z. Yao, "Research on constitutive equation of damage evolution of backfill based on the full tensile and compressive process," *Journal of Mining & Safety Engineering*, vol. 4, pp. 485–488, 2006.

[19] Z. Liu, X. Li, G. Zhao, Q. Li, and W. Wang, "Three-dimensional energy dissipation laws and reasonable matches between backfill and rock mass," *Chinese Journal of Rock Mechanics and Engineering*, vol. 29, no. 2, pp. 344–348, 2010.

[20] Z.-x. Liu, X.-B. Li, T.-g. Dai, and P. Cao, "On damage model of cemented tailings backfill and its match with rock mass," *Yan Tu Li Xue*, vol. 27, no. 9, pp. 1442–1446, 2006.

[21] Z.-x. Liu, M. Lan, S.-y. Xiao, and H.-q. Guo, "Damage failure of cemented backfill and its reasonable match with rock mass," *Transactions of Nonferrous Metals Society of China*, vol. 25, no. 3, pp. 954–959, 2015.

[22] J.-P. Qiu, L. Yang, J. Xing, and X.-G. Sun, "Analytical solution for determining the required strength of mine backfill based on its damage constitutive model," *Soil Mechanics and Foundation Engineering*, vol. 54, no. 6, 2018.

[23] Y. Xie, W. He, Z. Zhu, X. Liu, H. Liu, and T. Xie, "Study on backfill acoustic emission characteristic and damage evolution under uniaxial compression," *Chinese Journal of Applied Mechanics*, vol. 32, no. 4, pp. 670–676, 2015.

[24] C. Gong, C. Li, and K. Zhao, "Experimental study on b-value characteristics of acoustic emission of cemented filling body under loading and unloading test," *Journal of Mining and Safety Engineering*, vol. 31, no. 5, pp. 788–794, 2014.

[25] F. Zhang, W. Liu, and L. Shen, "Damage constitutive model for cemented paste backfill after mixing waste rock," in *Proceedings of the World Automation Congress 2012*, pp. 1–4, IEEE, Puerto Vallarta, Mexico, 24-28 June 2012.

[26] G. B. Yu, P. Yang, and Y. Z. Chen, "Study on damage constitutive model of cemented tailings backfill under uniaxial compression," in *Applied Mechanics and Materials*vol. 353-356, pp. 379–383, Trans Tech Publ, 2013.

[27] Y.-x. Ke, X.-m. Wang, Q.-l. Zhang, and E.-y. Liu, "Strength determination of crude tailings backfill in deep mine based on non-linear constitutive model," *Journal of Northeastern University*, vol. 38, no. 2, p. 280, 2017.

[28] B. S. Underwood, "A continuum damage model for asphalt cement and asphalt mastic fatigue," *International Journal of Fatigue*, vol. 82, pp. 387–401, 2016.

[29] J. Zhou and X. Chen, "Stress-strain behavior and statistical continuous damage model of cement mortar under high strain rates," *Journal of Materials in Civil Engineering*, vol. 25, no. 1, pp. 120–130, 2013.

[30] R. Cao, S. He, J. Wei, and F. Wang, "Study of modified statistical damage softening constitutive model for rock considering residual strength," *Rock and Soil Mechanics*, vol. 34, no. 6, pp. 1652–1660, 2013.

[31] H. Zhao, C. Shi, M. Zhao, and X. Li, "Statistical damage constitutive model for rocks considering residual strength," *International Journal of Geomechanics*, vol. 17, no. 1, Article ID 04016033, 2017.

[32] X. Ke, X. Zhou, X. Wang, T. Wang, H. Hou, and M. Zhou, "Effect of tailings fineness on the pore structure development of cemented paste backfill," *Construction and Building Materials*, vol. 126, pp. 345–350, 2016.

[33] D.-Y. Yoo, S. Kim, G.-J. Park, J.-J. Park, and S.-W. Kim, "Effects of fiber shape, aspect ratio, and volume fraction on flexural behavior of ultra-high-performance fiber-reinforced cement composites," *Composite Structures*, vol. 174, pp. 375–388, 2017.

[34] S. Zhang, L. Yang, F. Ren, J. Qiu, and H. Ding, "Rheological and mechanical properties of cemented foam backfill: effect of mineral admixture type and dosage," *Cement and Concrete Composites*, vol. 112, Article ID 103689, 2020.

[35] M. Fall, J. Célestin, M. Pokharel, and M. Touré, "A contribution to understanding the effects of curing temperature on the mechanical properties of mine cemented tailings backfill," *Engineering Geology*, vol. 114, no. 3-4, pp. 397–413, 2010.

[36] D. Wu, G. Sun, and G. Huang, "Experimental and simulation study on seepage characteristics of cemented tailings backfill," *Journal of Central South University*, vol. 46, no. 3, pp. 1050–1057, 2015.

[37] N. Abdul-Hussain and M. Fall, "Thermo-hydro-mechanical behaviour of sodium silicate-cemented paste tailings in column experiments," *Tunnelling and Underground Space Technology*, vol. 29, pp. 85–93, 2012.

[38] M. Fall, M. Benzaazoua, and E. G. Saa, "Mix proportioning of underground cemented tailings backfill," *Tunnelling and Underground Space Technology*, vol. 23, no. 1, pp. 80–90, 2008.

Research Article

Investigation on Shear Wave Velocity and Triaxial Mechanical Performance of Tailings Core from Tailings Dam

Pengfei Luo [ID]

School of Civil and Resource Engineering, University of Science and Technology Beijing, Beijing 100083, China

Correspondence should be addressed to Pengfei Luo; 515270288@qq.com

The physical and mechanical parameters of tailings are important to study the stability of tailings dams (TDs). In this study, a series of laboratory experiments (shear wave velocity, triaxial compressive, and peak strain strength testing) were conducted to obtain the mechanical properties of tailings from TD. The results showed the following. (1) The linear function fitting could characterize the quantitative relationship between shear wave velocity and hole depth. (2) The corresponding static pressure coefficient increased as the confining pressure increased. The exponential fitting could characterize the quantitative function relation between the static pressure coefficient and the confining pressure. (3) The cohesion and internal friction angle of the tailings sample were 20 kPa and 41°, respectively, and the logarithmic fitting could better characterize the quantitative relation between shear peak strength and confining pressure. The results of this study can provide important references for further research on the stability of TD.

1. Introduction

Mineral resources have provided important material support for the development of human civilization. The main methods for obtaining mineral resources are open-pit mining and underground mining. Orebody is subjected to a series of processes such as rock drilling, blasting, transportation, grinding, flotation, and smelting to obtain the required metal. The solid wastes obtained after flotation are collectively called tailings. At present, the main ways of tailings disposal are tailings backfilling and tailings discharge [1]. Some scholars and engineers have also tried to use tailings as a building material, but the effect is not very satisfactory. TDs are used to dispose of tailings waste, as shown in Figure 1. Once the TD collapses, an enormously destructive debris flow will flock to the downstream area, causing great harm to downstream lives and property and polluting the environment seriously [2]. 300 people were killed in the disaster of Brumadinho in Brazil [3]. Nowadays, the TD failure has become one of the major dangerous sources of mines all around the world.

To date, there are lots of references on TD, such as TD failure, stability numerical simulation, and stability measurements [4–9]. The research methods mainly include numerical simulation and on-site monitoring method [10–13]. Yang et al. [14] found that the application of geotextile tubes in the construction of TD is a good alternative for fine tailings disposal. The impedance ratio and the depth of foundation have the significant effect on the seismic factor of safety of TD [15]. The Earth observation-based service could be used to forecast any potential risk from TDs several weeks in advance [16]. Generally, TD is constructed from compacted tailings, and its mechanical properties are different from the cemented tailings backfill (CTB) or cemented paste backfill (CPB). Lots of scholars and engineers have investigated the macro-mechanical, micro-behaviors of CTB and CPB [17, 18].

However, there are few references on the compacted and loose tailings from TD. The main purpose of this study is to obtain the basic mechanical parameters of tailings from Makeng TD. A series of laboratory experiments (shear wave velocity, triaxial compressive, and peak strain strength tests) were conducted to obtain the above mechanical properties.
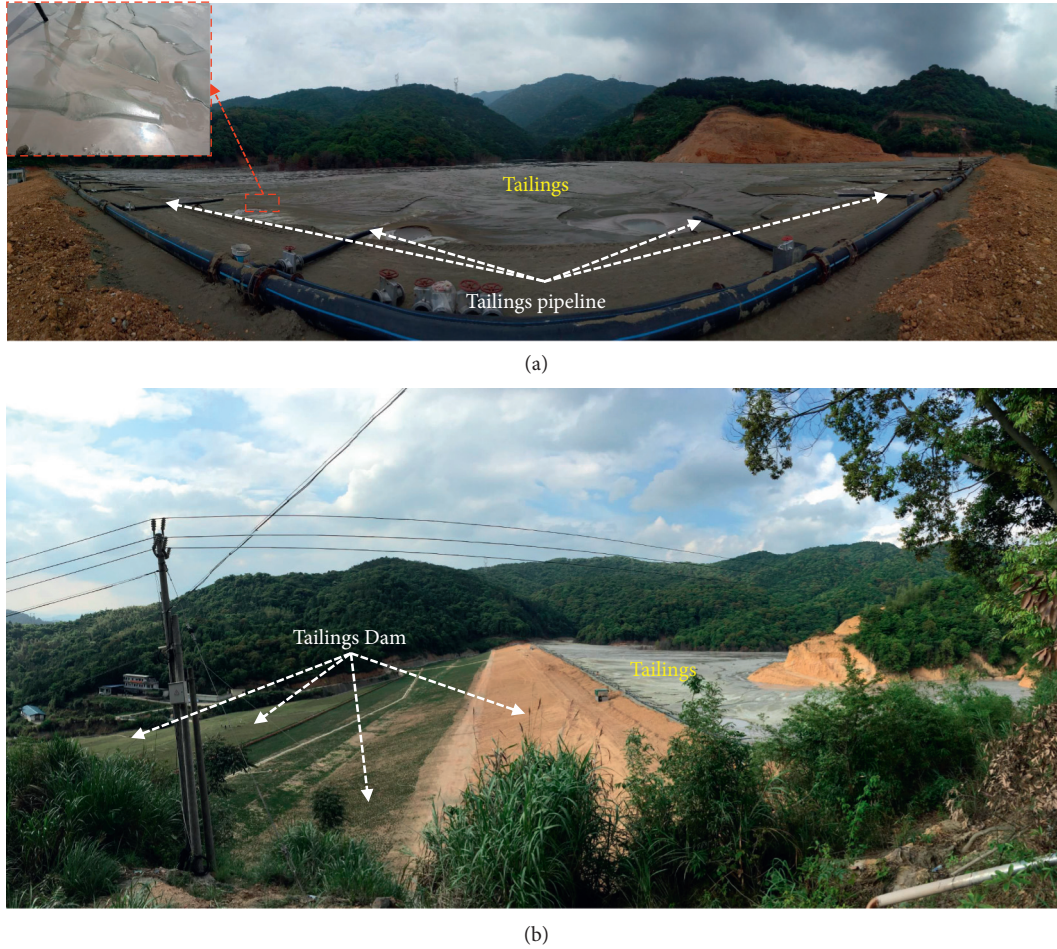
(a)

(b)

FIGURE 1: Photograph of the Makeng TD in this study.

The obtained mechanical parameters of tailings from TD will provide an important reference for further research on the stability of ultra-high TDs.

2. Materials and Methods

2.1. Tailings Characteristics. The tested tailings samples were obtained in a TD of Makeng Iron Mine, Fujian, China. In this study, the Shandong Nikeite NKT6100-D laser particle size analyzer was used to analysis the particle size distribution (PSD) of tested tailings. A total of 5 tailings samples were selected for testing. It is found that the tested tailings is mainly composed of SiO_2, CaO, Fe_2O_3, MgO, and Al_2O_3. The PSD curve is shown in Figure 2. The particle size and chemical components are shown in Tables 1 and 2, respectively.

2.2. Experimental Content

2.2.1. Tested Specimens from the TD. There are a total of 11 boreholes from TD, and the tested specimens were numbered ZK1, ZK2, ZK3, ZK4, ZK5, ZK6, ZK7, ZK8, ZK9, ZK10, and ZK11, respectively. The coring at the scene is shown in Figure 3.

2.2.2. Shear Wave Test. According to the Code for Seismic Design of Buildings (GB 50011-2010), shear wave test was conducted in this study. The suspended wave speed testing system named XG-I was used to analyze the relation between shear wave velocity and drilling depth. The basic parameter is shown as follows: dynamic range is 96 dB; preamp gain is 18-60 dB; and the probe used to receive signals from the instrument uses a suspended borehole detector. The main technical indicators are as follows: the horizontal detector has a natural frequency of 60 Hz and a sensitivity of 30 V/(m·s). The equivalent shear wave velocity could be measured as follows:

$$v_{se} = \frac{d_0}{t},$$
$$t = \sum_{i=1}^{n} \left(\frac{d_i}{v_{si}} \right), \tag{1}$$

where v_{se} is the equivalent shear wave velocity of soil layer; d_0 is the calculated depth, which is smaller than the thickness of the cover and 20 m; t is the shear wave which is between the ground and the calculated depth; d_i is the thickness (m) of the i-th soil layer; v_{si} is the shear wave velocity of the i-th soil layer; and n is the number of layers.
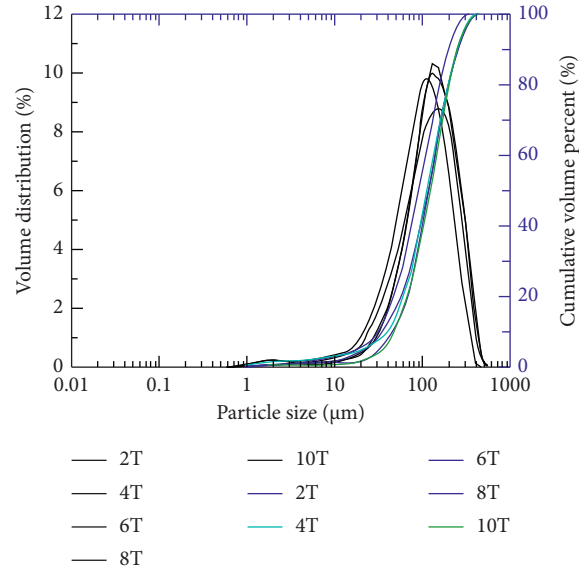
FIGURE 2: Particle size distribution curves of tailings in this study.

TABLE 1: Particle size of tested tailings from the TD.

ID	D_{10}	D_{50}	D_{90}	D_{95}	D_{97}	Specific surface area (cm^2/cm^3)
2T	47.12	118.15	246.03	287.85	314.09	967.60
4T	38.93	113.56	236.44	277.88	304.30	1464.89
6T	30.49	91.70	196.23	231.39	253.38	1522.53
8T	35.45	112.96	249.65	290.94	316.81	1169.74
10T	47.16	119.75	251.37	292.01	317.42	820.49
Average value	39.83	111.22	235.94	276.01	301.20	1189.05

TABLE 2: Chemical components of the tested tailings.

Varieties (%)	SiO_2	Al_2O_3	CaO	MgO	Fe_2O_3	MnO	Other
Content	37.07	3.60	26.06	9.00	18.47	2.07	3.73

2.2.3. Triaxial Compression Laboratory Test. The SLB-1 stress-strain controlled triaxial shear penetration tester was used in this study, which could perform unequal consolidation, isotropic consolidation, reverse pressure saturation, stress path test, and penetration test. Besides, the device could transfer the data to the computer during the whole testing. The testing standard was obtained according to the results from [19]. The main technical parameters of the equipment include the following: the range of axial force was 0–20 kN and the measurement accuracy was ±1%; the loading rate was set as 0.002~4 mm/min ± 10%; the diameter and height of tested specimen were 39.1 mm and 80 mm, respectively; and the confining pressure was set as 100 kPa, 200 kPa, 300 kPa, and 400 kPa, respectively. Figure 4 shows the process steps of the triaxial test.

3. Results and Discussion

3.1. Shear Wave Velocity Test Results. Table 3 shows the tested original data of shear wave and hole depth. In order to visually describe the quantitative relationship between the

TD core and wave velocity at different drilling depths and to facilitate the prediction of the wave velocity of subsequent deep drilling tailings cores, the relationship curve was plotted as shown in Figure 5.

It was observed from Figure 5 that the multiple correlation coefficients of exponential, linear, logarithmic, and power function fitting were 0.9554, 0.9601, 0.757, and 0.8181, respectively. It showed that the linear fitting could realize the quantitative characterization of the relation between the shear wave velocity and the hole depth, which could be shown in the following equation:

$$y = ax + b, \tag{2}$$

where y was the shear wave velocity; x represented the hole depth; and a and b were relative coefficients related to the shear wave velocity and the hole depth.

It was also found that tailings of TD less than 20 m belong to medium soft soil, while the tailings of TD between 20 and 30 m belong to medium hard soil according to the Code for Seismic Design of Buildings (GB 50011-2010).
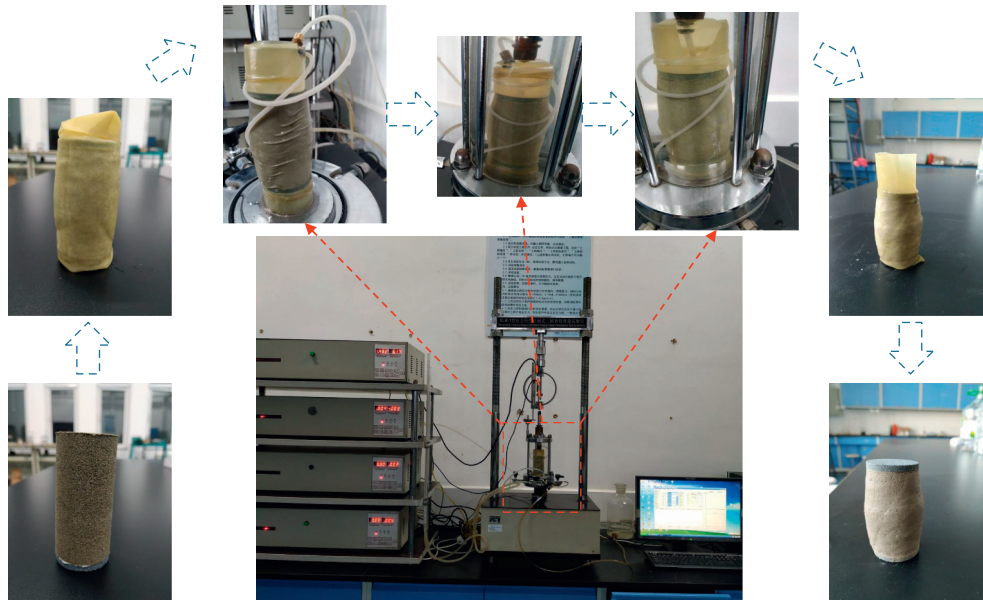
FIGURE 3: Coring of TD site.

FIGURE 4: The process steps of triaxial testing in this study.

3.2. Confining Pressure Effect on Triaxial Shear Strength. Figure 6 shows the relationship between the static pressure coefficient and the stress path under different confining pressure conditions. σ_3 was the minimum principal stress, and σ_1 was the maximum principal stress.

It can be seen from the analysis of Figure 6 that as the main pressure difference and the confining pressure gradually increase, the value of K_0 also gradually decreases and eventually approaches a stable value. When the confining pressure was 100 kPa, 200 kPa, 300 kPa, and 400 kPa, the corresponding values of K_0 were 0.18, 0.19, 0.21, and 0.23, respectively.

In order to quantitatively characterize the relationship between confining pressure and static lateral pressure coefficient, the linear, logarithmic, exponential, and power function fitting methods were used to calculate its complex correlation coefficient. The result is shown in Figure 7.

As shown in Figure 7, it was found that the multiple correlation coefficients of linear, exponential, logarithmic, and power function fitting were 0.9797, 0.9861, 0.8887, and 0.906, respectively. It shows that exponential fitting could

better characterize the quantitative relationship between static lateral pressure coefficient and confining pressure.

3.3. Confining Pressure Effect on Shear Peak Strength. Figure 8 shows the Mohr envelope circle under different confining pressures.

The cohesion and internal friction angle of the tested tailings specimen could be calculated by calculating the slope and intercept of the envelope circle tangent. Finally, the calculated cohesion and internal friction angle of the tailings sample were 20 kPa and 41°, respectively.

In order to quantitatively characterize the relationship between confining pressure and shear peak strength, the linear, logarithmic, exponential, and power function fitting methods were used to calculate its complex correlation coefficient. The result is shown in Figure 9.

As shown in Figure 9, it was found that the multiple correlation coefficients of linear, exponential, logarithmic, and power function fitting were 0.9595, 0.8961, 0.9965, and 0.9833, respectively. It shows that logarithmic fitting could

TABLE 3: The original data of hole depth and shear wave in this study.

Hole depth (m)	Shear wave (m/s)	Hole depth (m)	Shear wave (m/s)	Hole depth (m)	Shear wave (m/s)
1	98	11	141	21	251
2	110	12	158	22	265
3	108	13	161	23	276
4	113	14	167	24	279
5	116	15	185	25	286
6	117	16	212	26	290
7	118	17	234	27	293
8	121	18	238	28	295
9	124	19	243	29	297
10	130	20	247	30	300

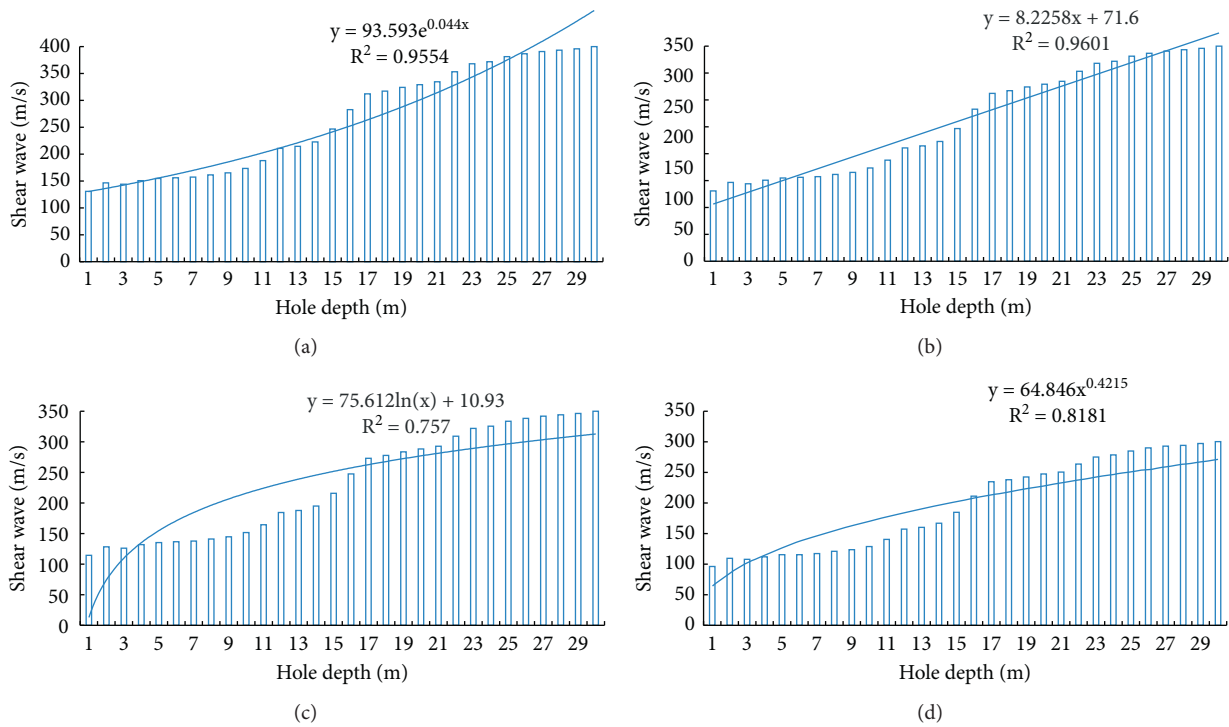

(a)

(b)

(c)

(d)

FIGURE 5: Relations between shear wave and hole depth.
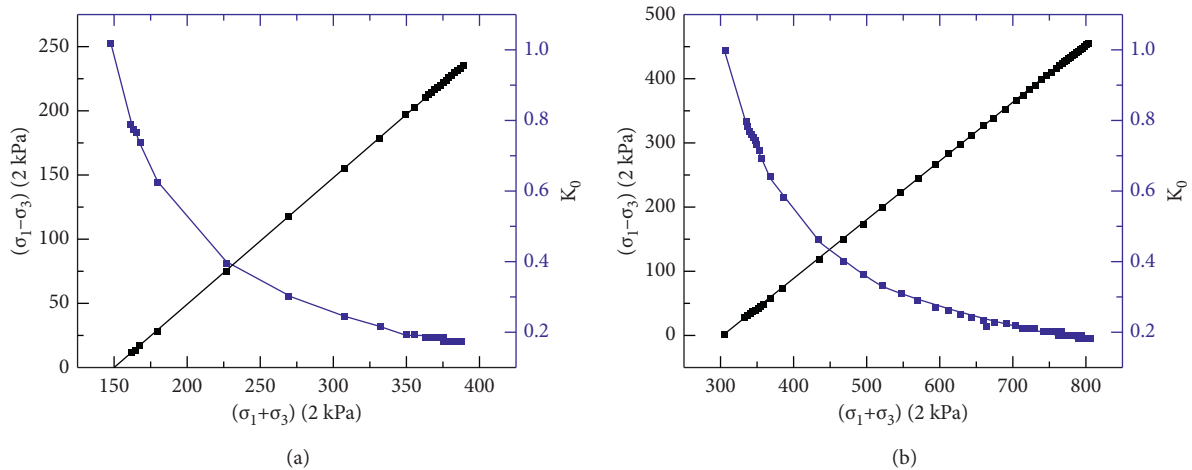

(a)

(b)

FIGURE 6: Continued.

(c)

(d)
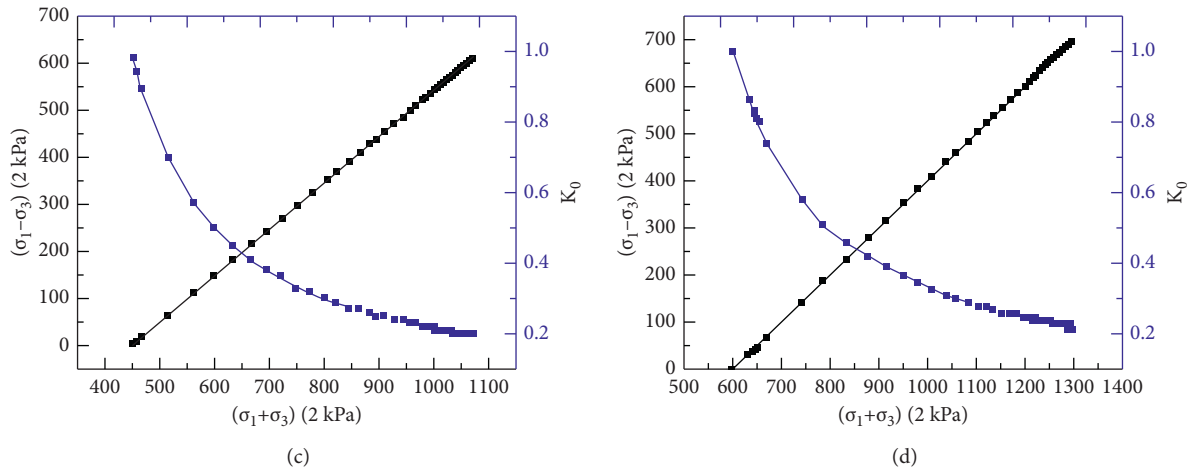
FIGURE 6: Relations between static pressure coefficient and the stress path. (a) 100 kPa. (b) 200 kPa. (c) 300 kPa. (d) 400 kPa.

$y = 0.017x + 0.16$
$R^2 = 0.9797$

(a)

$y = 0.1636e^{0.0835x}$
$R^2 = 0.9861$

(b)

$y = 0.0348\ln(x) + 0.1749$
$R^2 = 0.8887$

(c)

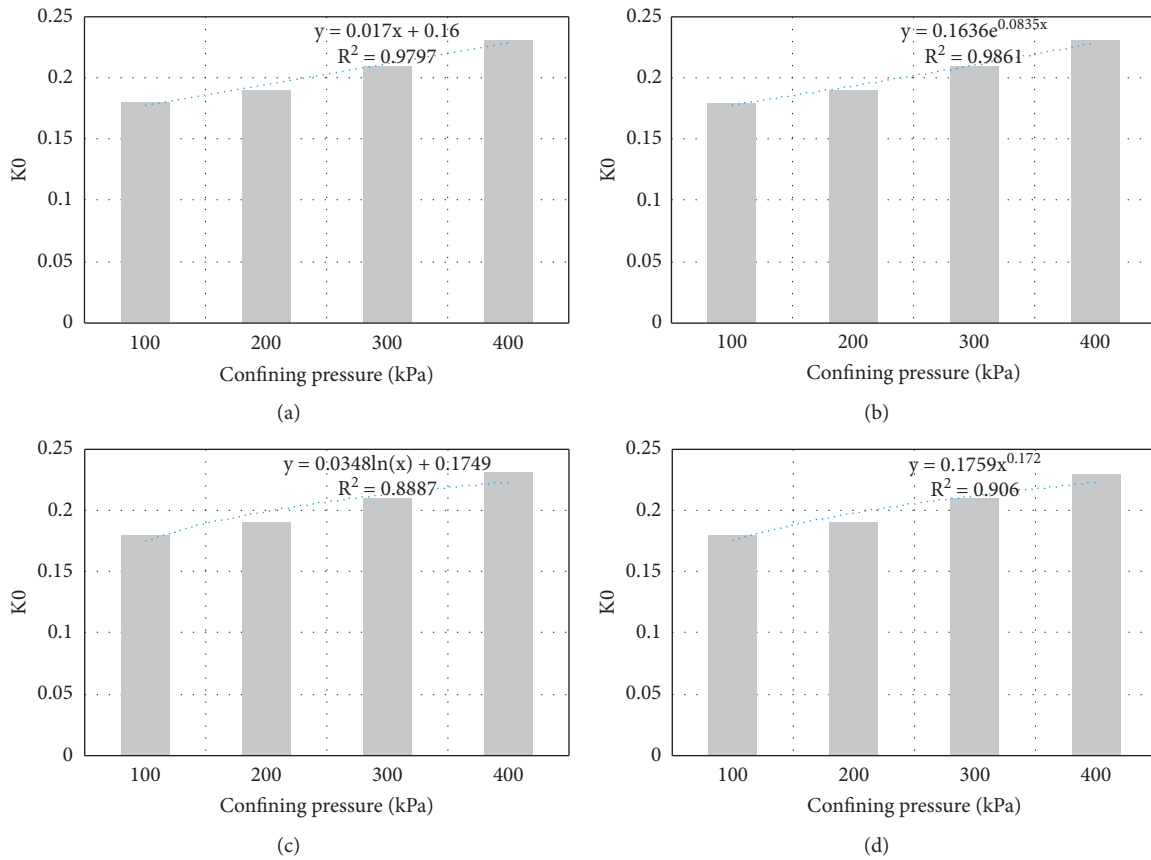$y = 0.1759x^{0.172}$
$R^2 = 0.906$

(d)

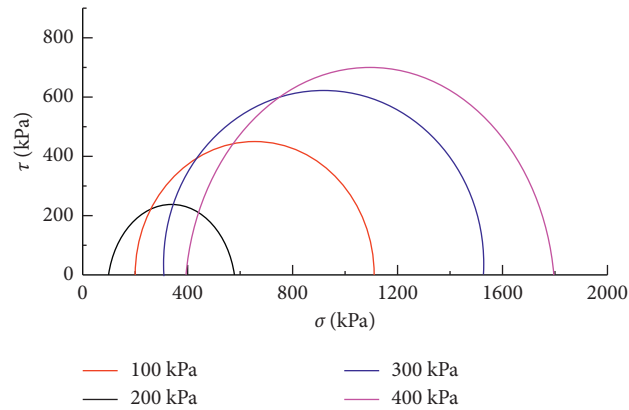FIGURE 7: Relations between confining pressure and K_0.

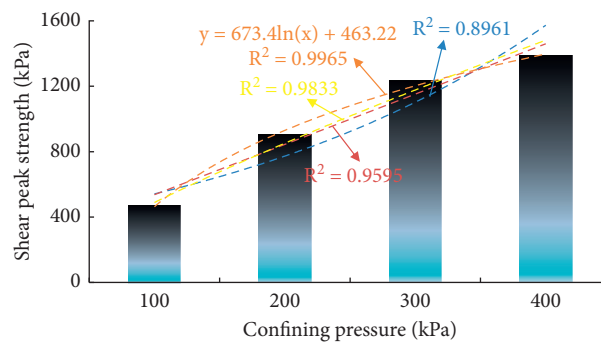FIGURE 8: Mohr envelope circle under different confining pressures.

FIGURE 9: Relations between confining pressure and shear peak strength.

better characterize the quantitative relationship between shear peak strength and confining pressure.

4. Conclusion

In this study, a series of laboratory experiments have been conducted to evaluate the mechanical performance of tailings specimens from TD. The following conclusions can be drawn from the current study based on the analysis and discussion of the experimental results.

(1) The quantitative relationship between shear wave and hole depth can be expressed as linear equation. It was found that the tailings of TD less than 20 m belong to medium soft soil, while the tailings of TD between 20 and 30 m belong to medium hard soil.

(2) The corresponding static pressure coefficient increased as the confining pressure increased. The quantitative relation between the static pressure coefficient and confining pressure was exponential equation.

(3) The cohesion and internal friction angle of the tailings sample were 20 kPa and 41°, respectively. Besides, the logarithmic fitting could better characterize the quantitative relation between shear peak strength and confining pressure.

The basic mechanical characteristics of tailings from TD provide an important reference for further research on the stability of ultra-high tailings dams. In the future, the author will use on-site monitoring and numerical simulation to study the stability of TDs.

Data Availability

The data in this study were obtained by laboratory testing. The data analysis is included within the article.

Conflicts of Interest

The author declares that there are no conflicts of interest.

Acknowledgments

References

[1] S. Cao, E. Yilmaz, W. Song, E. Yilmaz, and G. Xue, "Loading rate effect on uniaxial compressive strength behavior and acoustic emission properties of cemented tailings backfill," *Construction and Building Materials*, vol. 213, pp. 313–324, 2019.

[2] G. M. Yu, C. W. Song, J. B. Zou et al., "Applications of online monitoring technology for tailings dam on digital mine,"

Transactions of Nonferrous Metals Society of China, vol. 21, pp. 604–609, 2011.

[3] M. Armstrong, N. Langrene, R. Petter, W. Chen, and C. Petter, "Accounting for tailings dam failures in the valuation of mining project," *Resources Policy*, vol. 63, Article ID 101461, 2019.

[4] L. Dong, D. Sun, and X. Li, "Theoretical and case studies of interval nonprobabilistic reliability for tailing dam stability," *Geofluids*, vol. 2017, Article ID 8745894, 11 pages, 2017.

[5] D. Kossoff, W. E. Dubbin, M. Alfredsson, S. J. Edwards, M. G. Macklin, and K. A. Hudson-Edwards, "Mine tailings dams: characteristics, failure, environmental impacts, and remediation," *Applied Geochemistry*, vol. 51, pp. 229–245, 2014.

[6] J. Tong, C. Miaowen, J. Juhui, L. Jinxian, and C. Baofeng, "Endophytic fungi and soil microbial community character- istics over different years of phytoremediation in a copper tailings dam of Shanxi, China," *The Science of the Total En- vironment*, vol. 574, pp. 881–888, 2017.

[7] Y. S. Wang, N. Anderson, and E. Torgashov, "Condition assessment of building foundation in Karst terrain using both electrical resistivity tomography and multi-channell analysis surface wave techniques," *Geotechnical & Geological Engi- neering*, vol. 38, pp. 1839–1855, 2019.

[8] B. Xu and Y. Wang, "Stability analysis of the Lingshan gold mine tailings dam under conditions of a raised dam height," *Bulletin of Engineering Geology and the Environment*, vol. 74, no. 1, pp. 151–161, 2015.

[9] X. Yu, X. Kang, Y. Li et al., "Rhizobia population was favoured during in situ phytoremediation of vanadium-titanium magnetite mine tailings dam using Pongamia pinnata," *En- vironmental Pollution*, vol. 255, Article ID 113167, 2019.

[10] Z. Deng, S. Wu, Z. Fan, Z. Yan, and J. Wu, "Research on the overtopping-induced breaching mechanism of tailings dam and its numerical simulation," *Advances in Civil Engineering*, vol. 2019, Article ID 3264342, 10 pages, 2019.

[11] Z. Lyu, J. Chai, Z. Xu, Y. Qin, and J. Cao, "A comprehensive review on reasons for tailings dam failures based on case history," *Advances in Civil Engineering*, vol. 2019, Article ID 4159306, 18 pages, 2019.

[12] H.-m. Liu, G. Nan, W. Guo, C.-h. Yang, and C. Zhang, "Analytical solution and application for one-dimensional consolidation of tailings dam," *Mathematical Problems in Engineering*, vol. 2018, Article ID 4573780, 9 pages, 2018.

[13] Z. Xu, X. Yang, J. Chai, Y. Qin, and Y. Li, "Permeability characteristics of tailings considering chemical and physical clogging in Lixi tailings dam, China," *Journal of Chemistry*, vol. 2016, Article ID 8147845, 8 pages, 2016.

[14] Y. Yang, Z. Wei, G. Cao et al., "A case study on utilizing geotextile tubes for tailings dams construction in China," *Geotextiles and Geomembranes*, vol. 47, no. 2, pp. 187–192, 2019.

[15] S. Nimbalkar, V. S. R. Annapareddy, and A. Pain, "A sim- plified approach to assess seismic stability of tailings dams," *Journal of Rock Mechanics and Geotechnical Engineering*, vol. 10, no. 6, pp. 1082–1090, 2018.

[16] D. Lumbroso, C. McElroy, C. Goff, M. R. Collell, G. Petkovsek, and M. Wetton, "The potential to reduce the risks posed by tailings dams using satellite-based information," *International Journal of Disaster Risk Reduction*, vol. 38, Article ID 101209, 2019.

[17] S. Cao, E. Yilmaz, and W. Song, "Fiber type effect on strength, toughness and microstructure of early age cemented tailings backfill," *Construction and Building Materials*, vol. 223, pp. 44–54, 2019.

[18] G. Xue, E. Yilmaz, W. Song, and S. Cao, "Mechanical, flexural and microstructural properties of cement-tailings matrix composites: effects of fiber type and dosage," *Composites Part B: Engineering*, vol. 172, pp. 131–142, 2019.

[19] T. Yoshikawa and T. Noda, "Triaxial test on water absorption compression of unsaturated soil and its soil-water-air-coupled elastoplastic finite deformation analysis," *Soils and Founda- tions*, vol. 60, no. 5, pp. 1151–1170, 2020.